

ALMA MATER STUDIORUM - UNIVERSITÀ DI BOLOGNA

SCUOLA DI INGEGNERIA E ARCHITETTURA

DIPARTIMENTO DI TECNICA DELLE COSTRUZIONI

CORSO DI LAUREA IN CIVIL ENGINEERING

TESI DI LAUREA

in

Structural Engineering

**STRUCTURAL OPTIMIZATION OF A 3D-PRINTED BRANCH OF
A TREE-LIKE COLUMN**

CANDIDATO
Todeschi Matteo

RELATORE:
Trombetti Tomaso

Anno Accademico 2017/18

Data: 23/07/2018

ACKNOWLEDGEMENT

First, I would like to thank all the committee members for their support and help provided for the development of this thesis. I also want to mention Filippo Giraldi and Benedetto di Castro, from MX3D and RamLAB respectively, for the precious information they shared with me about 3D printing.

Second, I would like to say a big “thank you” to my parents that allowed me to spend an entire year abroad. Despite I was not the best period to leave the family they never stopped me and supported me the whole time. I have no words to describe how thankful I am for what they have done for me.

Third, I want to thank my girlfriend, because she patiently waited my return, first from Australia and then from the Netherlands. We have been far from each other for a long time, but she always supported and trusted in me.

Finally, I would like to thank all my friends, the old ones, from my hometown, but also the new ones .people I have met during these last two years of Master: all my course mates in Bologna, the Spanish girls of Via Marconi, the guys of 172 Coogee Bay Road (Sydney), the Pegasus (gymnastic association, Delft), and every single person that contributed to making these two years simply incredible and unforgettable.

ABSTRACT

3D printed steel is becoming more and more common. This research aims to assess the potential of steel 3D-printing in the building sector. A case study is used to investigate possibilities and limitations of 3D-printed steel for structural elements. The analysis is based on the structural optimization of a branch of an existing dendriform column. An algorithm based on a second order non-linear analysis has been generated to perform the shape and size optimization of the branch. An assessment of the hard constraints to be applied for the minimization of the mass is reported. Finally, an investigation on the effects of imperfections on the optimization process has been performed.

CONTENTS

ABSTRACT	III
CONTENTS.....	IV
NOMENCLATURE	VII
i. List of Symbols	vii
ii. List of Abbreviations.....	viii
iii. Labels used for Geometries	viii
RESEARCH QUESTIONS AND METHODOLOGY.....	1
1 Introduction	1
2 Research Question	3
3 Research Methodology	3
BACKGROUND OF THE RESEARCH	6
4 3D-Printing Process and Material Properties.....	6
4.1 <i>Overview on Additive Manufacturing</i>	6
4.2 <i>Metal Additive Manufacturing</i>	7
4.3 <i>Printing process for WAAM</i>	11
4.4 <i>Properties of 3D-Printed Steel</i>	12
5 Structural optimization	21
5.1 <i>Mathematical Programming Problem</i>	21
5.2 <i>Multi-objective Optimization</i>	22
6 Case Study: Zlote Tarasy	25
6.1 <i>Overview of the Building</i>	25
6.2 <i>The Atrium Roof</i>	26
6.3 <i>Structural Properties of the Element</i>	29
COMPUTATIONAL MODEL AND OPTIMIZATION ALGORITHM	32
7 Structural Analysis for Parametric Design.....	32
7.1 <i>Parametric Drawing</i>	32
7.2 <i>Non-Linear Analysis</i>	33
7.3 <i>Second Order Effects</i>	34
7.4 <i>Initial Imperfections of Steel Columns</i>	36

8	Settings and Calibration of the Model	38
8.1	<i>Loading Conditions and Material</i>	38
8.2	<i>Topology Optimization</i>	38
8.3	<i>Shape Optimization</i>	39
8.4	<i>Definition of the Geometry</i>	42
8.5	<i>Optimization Algorithm</i>	47
8.6	<i>Settings for the Evolutionary Solver</i>	48
8.7	<i>Application of Constrains</i>	48
8.8	<i>Size optimization</i>	49
8.9	<i>Boundary Conditions</i>	52
9	Analysis of Convergence	54
10	Summary of Settings for Optimization Process.....	56
10.1	<i>Settings for Finite Element Analysis</i>	56
10.2	<i>Settings for Optimization Algorithm</i>	57
ANALYSIS OF RESULTS		59
11	Definition of the Optimum Solution for p1	59
11.1	<i>Solution of optimization without Imperfections</i>	59
11.2	<i>Optimization with Imperfections</i>	62
11.3	<i>Solution for random imperfections</i>	63
12	Definition of the Optimum Solution for p2	66
13	Comparison of Results	68
13.1	<i>Assessment of the Optimization Level</i>	69
13.2	<i>Assessment of Strength and Efficiency</i>	69
13.3	<i>Comparison with Original Column</i>	71
DISCUSSION		73
14	Conclusions	73
14.1	<i>Summary of the process</i>	73
14.2	<i>Summary of Results</i>	74
15	Answers to the Research Questions	75
16	Final Remarks and Future Research	75
REFERENCES		77
APPENDICES		81
I. DENDRIFORM STRUCTURES.....		81
II. GENERATION OF THE MESH.....		87
i.	Summary of Parameters and Conditions	87
ii.	Generation Procedure.....	88

III.	FULL RESULTS TEST ON CONVERGENCE	92
i.	Geometries tested for Convergence Analysis	92
ii.	Algorithm for Convergence Analysis	96
IV.	DISTRIBUTION OF CROSS-SECTIONS FOR OPTIMIZED GEOMETRY P1_GI_I	97
V.	FEEDSTOCK MATERIALS.....	98
i.	Ugiweld Welding Wire	98
ii.	Oerlikon Welding Wire.....	98

NOMENCLATURE

i. List of Symbols

Symbol	Description	Unit
α	Coefficient of thermal expansion	/°C
λ	Slenderness	-
$\bar{\lambda}$	Relative slenderness	-
λ_e	Limit slenderness	-
γ	Density	<i>Kg/m³</i>
θ	Total angle of rotation of the hoops	<i>Deg/m</i>
\emptyset	Outer diameter	<i>mm</i>
A	Area	<i>mm² or cm²</i>
a	Shape amplification factor	<i>m</i>
BF	Buckling Factor	-
E	Young modulus	<i>Mpa</i>
e_0	Initial crookedness	<i>mm</i>
e_0	Factored crookedness	<i>mm</i>
f_y	Yielding strength	<i>MPa</i>
G	Shear Modulus	<i>MPa</i>
I	Modulus of inertia	<i>mm⁴ or cm⁴</i>
k	Buckling Factor	-
L	Member length	<i>mm</i>
L_{meas}	Measured length	<i>mm</i>
L_{eff}	Effective length	<i>mm</i>
M_e	Maximum external bending moment	<i>kN m</i>
N_e	Maximum external axial force	<i>kN</i>
n_h	number of hoops	-
n_i	number of inclined elements	-
P	Applied load	<i>kN</i>
P_0	Design load	<i>kN</i>
$p(x)$	Shape pattern	-
R	Actual radius	<i>mm</i>
r	Radius of gyration	<i>mm</i>
r_r	Reference radius	<i>mm</i>
T	Wall thickness	<i>mm</i>
V_e	Maximum external shear force	<i>kN</i>
ν	Poisson Ratio	-
U	Utilization	-
U_m	Average Utilization	-

ii. List of Abbreviations

Abbreviation	Description
1D	One Dimensional
3D	Three Dimensional
3DS	3D printed steel
AM	Additive Manufacturing
C-S	Cross-Section
DOF	Degree of Freedom
EC3	Eurocode 3
GI	Global Imperfections
LF	Load Factor
MAM	Metal Additive Manufacturing
MOO	Multi-Objective Optimization
NI	No Imperfections (perfect system)
OC	Original Column
SLS	Serviceability Limit State
SS	Stainless steel
TS	Traditional Steel
TUDeft	Delft University of Technology
ULS	Ultimate Limit State
UNIBO	University of Bologna
WAAM	Wire Arch Additive Manufacturing

iii. Labels used for Geometries

OC= original column, column located on site

CHS x y = Circular Hollow Section; $d= x$ mm; $t= y$ mm

Pattern_ImperfectionsUsedInOptimization_Imperfections_Modifications

Example: P2_GI_P_M

Column with shape pattern P2, obtained from reference geometry optimized with initial global imperfections, perfect (straight axis), modified (cross sections are modified with respect to reference geometry)

RESEARCH QUESTIONS AND METHODOLOGY

1 INTRODUCTION



Figure 1. 3D printed steel bridge the at MX3D [1]

The technology is running fast, 3D printing is no more limited to small plastic elements but is coming up also in the building sector. A lot of companies and start-ups are investing time and resources to develop new methods to fabricate metal pieces with geometries not achievable with traditional production processes. However, to exploit these new shapes, designer need to be prepared to welcome these technologies into their sector and be capable to ensure sufficient levels of safety in their design.

MX3D, born in 2014 as a start-up is now a world-wide know reality in the sector of 3D printing with steel, thanks to their 3D printed pedestrian bridge (Figure 1). Although the

bridge is still not placed on side, the structure is already fully assembled, making it the very first fully functional 3D printed steel structure in the world.

This unique design shows exactly how this technology can achieve shapes never seen before in the building industry (at least for load bearing elements). However, engineers must be ready to welcome all the freedom coming from the advancement of the production process and develop design strategies ad hoc to make sure that their design satisfy the safety requirements set by national and international design codes.



Figure 2. Laser-cut cardboard columns [2]

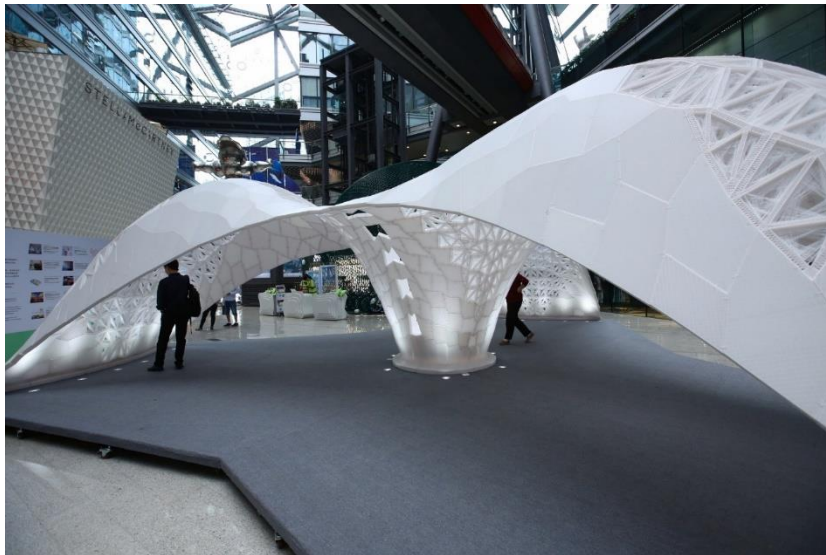


Figure 3. Largest 3D printed shell structure at the Laboratory of Creative Design, Beijing [3]

2 RESEARCH QUESTION

This paper aims to investigate how traditional elements can be reinvented thanks to the 3D printing process. Studies on the application of this technology on small steel loadbearing parts can be already be found in the literature. [4], [5]. However, no information is publicly available on how to design big structural elements with 3D printed steel. Therefore, this research tries to close this gap with a case study on a simply supported straight column. Through this case study the author tries to answer the following questions:

- How would an optimized 3D printed column look like?
- Is it already possible to achieve better performances with 3D printing?

3 RESEARCH METHODOLOGY

The research is organised so that the reader can gain the basic knowledge of the key elements that are utilized in the actual analysis.

Chapter 4-5

A literature review on the following topics is presented:

- 3D printing of steel: printing process and consequent material properties
- Basic concepts of structural optimization
- Buckling of steel structures

Chapter 6

A case study is used to answer the research questions identified in the previous chapter, thus, also basic information on the reference building and its structural requirements are presented. Technical details on the properties of the reference column are given.

Chapter 7-8-9-10

From this basic information, the analysis is developed. Settings and properties of the structural model and the optimization algorithm are presented.

Chapter 11-12

The optimum solutions are presented and analysed. Effects of imperfections on the optimization problem and on the structural performance are investigated

Chapter 13-14

Comparison between the various solutions that have been found, 3D printed circular hollow tubes and the original steel column in place.

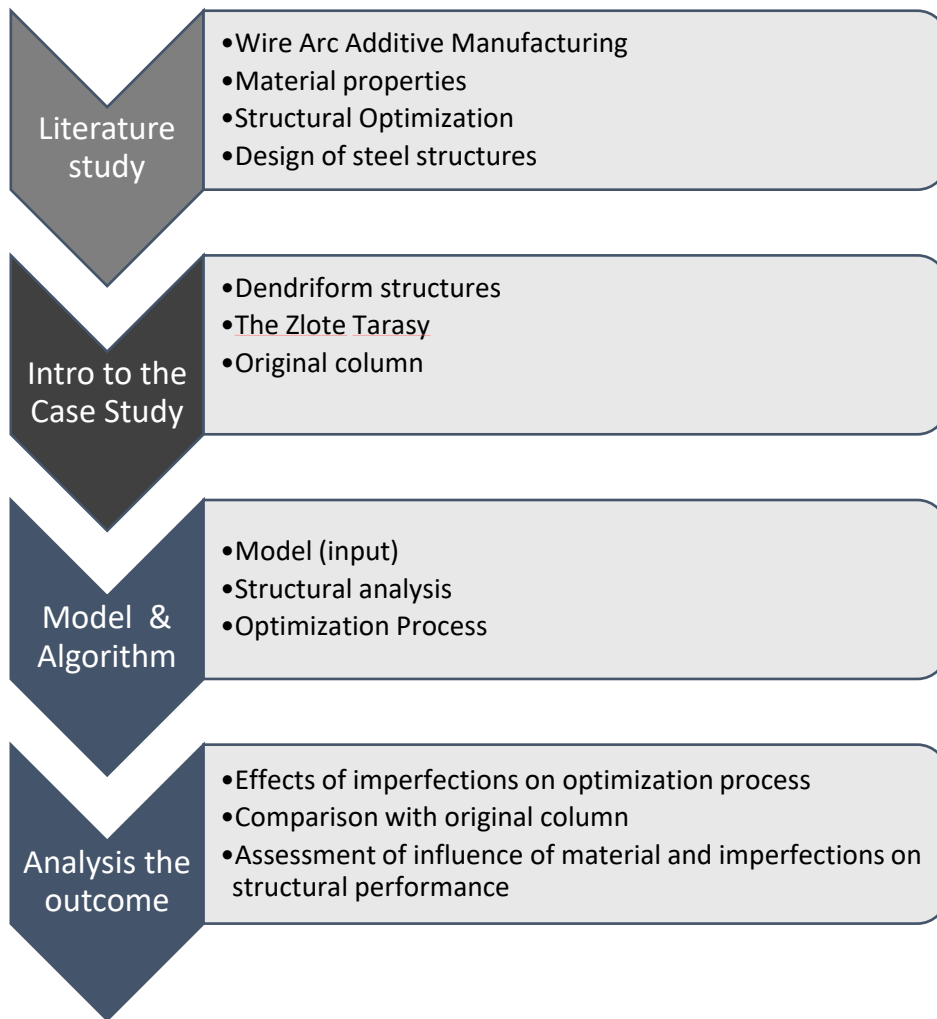


Figure 4. Structure of the report

BACKGROUND OF THE RESEARCH

4 3D-PRINTING PROCESS AND MATERIAL PROPERTIES

4.1 OVERVIEW ON ADDITIVE MANUFACTURING

Additive Manufacturing, also known as 3D-printing, consists in the layer-upon layer deposition of material to build a three-dimensional product. The technique has grown significantly in the last few decades thanks to the increase of the computer power and the consequent improvement of the automation and CAD industry.

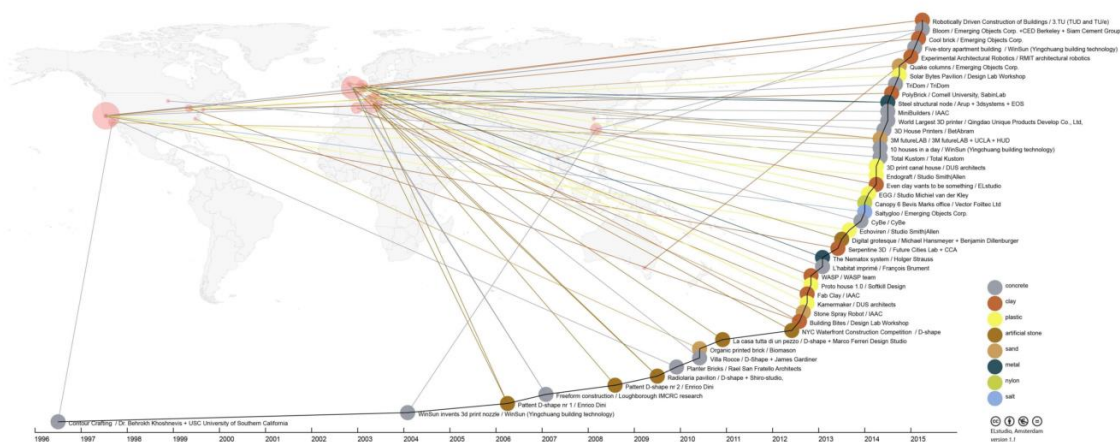


Figure 5. Timeline of AM growth [6]

These two elements are essential for the development and diffusion of AM. Automation is fundamental to achieve standardized, high quality products. Similarly, high quality CAD models are necessary to convert the design into a numerical input to guide the printing machine. The direct link between machines and CAD software packages allows to move from the computational model to the actual product in few ours, or even minutes (depending on technique, complexity and size and the product). At the same time, automation ensures that the product will have specific characteristics as human error cannot interfere. This allows to achieve a more standardised quality, both in terms of

accuracy but also in terms of defects. The combination of speed of production and the quality control brings to the conclusion that it is possible to achieve highly customized products, on demand, with a certified quality. In his thesis, van Bolderen [6], based also on the analysis of Attaran [7], the identified all the advantage reported in Table 1.

Table 1. Overview of advantages of additive manufacturing [6]

Areas of Application	Advantages over Traditional Manufacturing
<i>Rapid Prototyping</i>	Reduce time-to-market by accelerating prototyping Reduce the cost involved in product development Making companies more efficient and competitive at innovation
<i>Production of Spare Parts</i>	Reduce repair times Reduce labour cost Avoid costly warehousing/stock
<i>Small Volume Manufacturing</i>	Small batches can be produced cost-efficiently Eliminate investment in tooling
<i>Customized Unique Items</i>	Enable mass customization at low cost Quick production of exact and customized replacement parts on site Eliminate penalty for redesign
<i>Machine Tool Manufacturing</i>	Reduce labour cost Avoid costly warehousing/stock Enables mass customization at low cost
<i>Rapid Manufacturing</i>	Directly manufacturing end-use components Relatively inexpensive production of small numbers of parts
<i>Component Manufacturing</i>	Enable mass customization at low cost Quality improvement Shorten supply chain Reduce development costs Help eliminate excess parts
<i>On-Site Manufacturing & Repair</i>	Eliminate storage and transportation costs Save money by preventing downtimes Reduces repair costs considerably Shorten supply chain The need for large inventory is reduced Allow product lifecycle leverage
<i>Rapid Repair</i>	Significant reduction in repair time Opportunity to modify repaired components to the latest design
<i>Very Complex workpieces</i>	Produce very complex work pieces at low cost

4.2 METAL ADDITIVE MANUFACTURING

AM is suitable for a large series of materials including metals, ceramics, polymers, composites and biological systems. [8] For structural applications the most suitable material is certainly metal as demonstrated from the common practice. Successful experiments have been already conducted with Metal Additive Manufacturing (MAM) on aluminium, titanium, copper alloys, carbon and stainless steel. [6]



Figure 6. Certified WAAM propeller made of copper built at RamLAB, Rotterdam [9] [10]

Application in the automotive, aerospace, maritime and medical industry are already common practice [7] , and as demonstrate by MX3D, new applications are coming up also in the building sector.[11][12]

The technologies related to MAM are classified depending on the heat source and the form of the material source (feedstock). According to this classification we can distinguish the technologies in Figure 7.

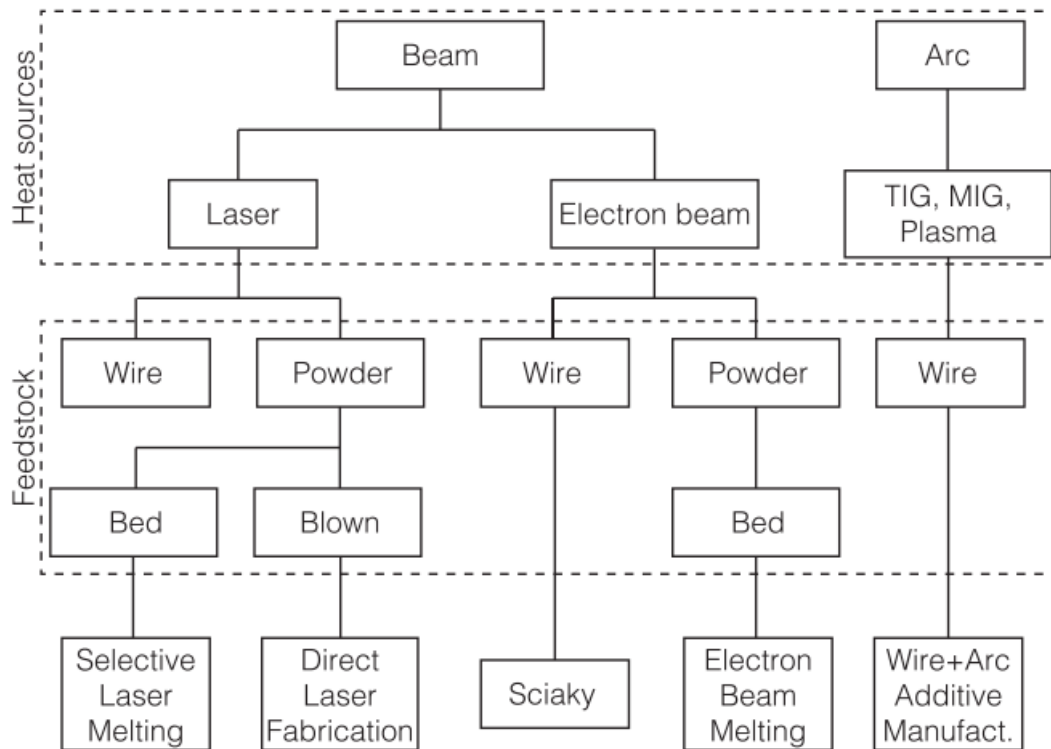


Figure 7. MAM technologies [13]

4.2.1 Powder Bed Process

This process is very similar to a normal thermal printing process for receipts, where a heat source is focused on photosensible paper. The only difference is that instead of printing on paper we are melting metallic powder.

The process consists in alternating a specific cycle:

1. A powder bed is spread in the printing chamber.
2. The heat source melts the upper layer (20 to 100 μm) that solidifies onto the previous layer
3. The support of the powder bed moves down and a new layer of powder is added to balance the vertical downward displacement of the support.
4. The cycle restarts.

This technique is particularly suitable for mechanical parts of limited dimensions as allows to achieve accuracies of the order of 100 μm with very low printing errors. However, it has the drawbacks of being confined into a chamber, thus it cannot be applied to print voluminous elements.

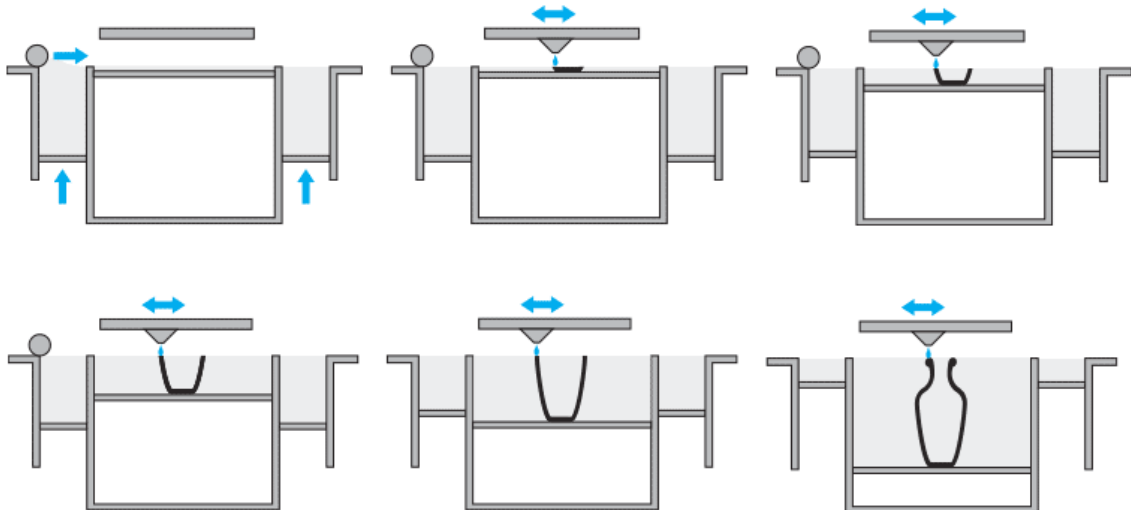


Figure 8. Powder bed MAM [14]

4.2.2 Powder Feed Process and Wire Additive Manufacturing

These two processes are similar in terms of printing process and heat source, but differ for the feedstock. The former usually requires a power beam (either laser or electron) mounted on a robotic arm, to concentrate the heat on the metallic powder that is “sprayed” or deposited by means of another nozzle on the previously deposited layer of material. With this process accuracies of the order of 200 μm can be achieved. It is usually applied to fabrication or repair of small parts and take place in a protected environment. Its advantage is the high accuracy and that it is theoretically possible to switch from one material to the other without any interruption in the printing process.[15]

The second technology utilizes a similar printing process, based on a robotic arm, but utilizes a traditional welding wire as input material. The heat source can be either a power beam or an arc. The use of a traditional wire in combination with the arc technology are

key elements as allow, with specific modifications, the use of traditional welding robots to 3D print steel elements. This is a major economical advantage as both robots and input material have already been available on the market for a long time, making them more affordable.

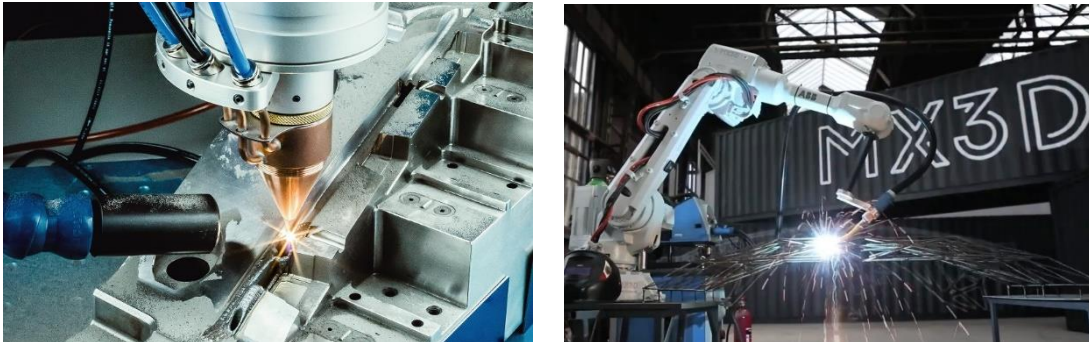


Figure 9. Powder feed AM vs WAAM [12] [16]

Another advantage of Wire Arc Additive Manufacturing is the most suitable to construct parts of relevant dimensions. This is because the printing area is not constrained into the boundaries of a chamber. However, it has to be noticed that the actual technology is still not capable to be applied to very large scale. This is because of robot limitations. Unless further movable supports are provided to the robots, the printing space is still limited to a certain volume. Another practical limitation of this printing process is that the material properties are deeply influenced by the deposition sequence (toolpath) and orientation both due to how the material settles onto the previous layer, and due to the thermal residual stresses induced by the cooling down of the fused material. This means that, despite the arm of the robot has 6 degrees of freedom, usually a movable base plate is used as a support for the object to be printed in order to add other 3 degrees of freedom, and ensure the correct deposition angle¹. This condition further restrains the printable area and the dimensions of the printable products.

Nevertheless, the diagram depicted in Figure 11 clearly shows how this technology is the most suitable when high accuracies and geometrical complexities are not needed.

¹ Note that RamLAB applies this technology while MX3D does not yet



Figure 10. Printing set up at RamLAB

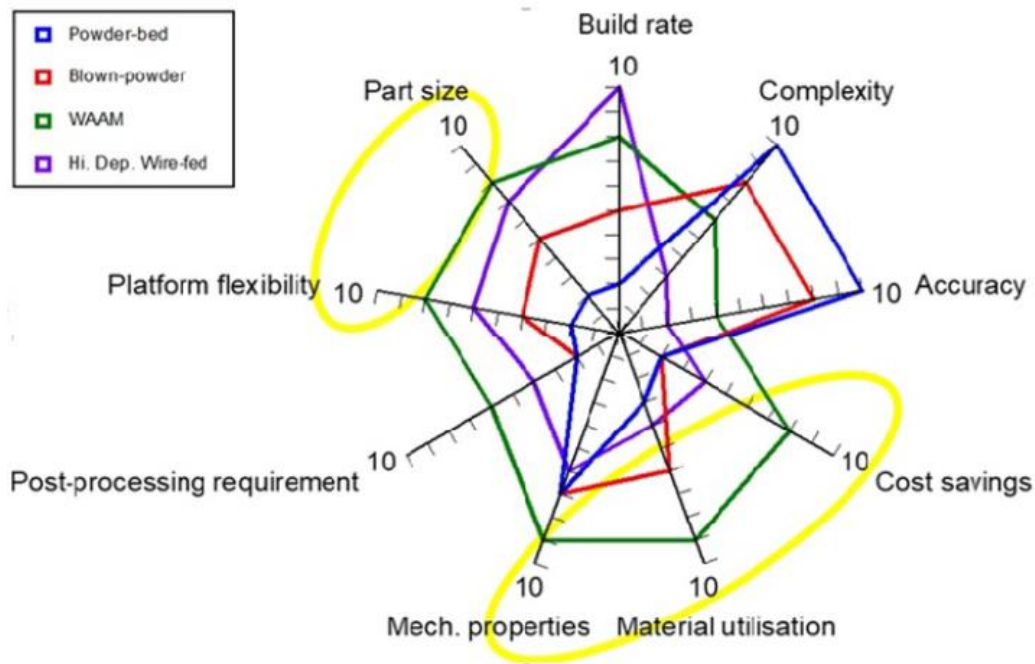


Figure 11. Comparison of the MAM techniques [6]

4.3 PRINTING PROCESS FOR WAAM

The printing process involves 4 steps:

1. Conversion of the CAD model to a remodelling software specific for 3d printing
2. Creation of the optimal toolpath
3. Import the toolpath model into the software of the robot.
4. Send the input to the robot and set up the printing parameters.
5. Actually print the element



Figure 12. WAAM propeller, finished vs raw surface

In most cases a 6th phase is also needed. Due to imperfections, defects and the thickness of the layers, very often a milling phase is required to achieve a smooth finish

4.4 PROPERTIES OF 3D-PRINTED STEEL

Since most of the data utilized in this thesis are extracted from researches on MX3D WAAM products, this chapter aims to collect all the base information needed to develop a computational model of a structure made of such a technique and material.

Both Van Bolderen (TUDelft) and University of Bologna (UNIBO) have investigated the properties of 3D-printed steel [6], [17]. The base material used in the tests, that is also the most commonly used by MX3D, is the ER 308L stainless steel.

This material is generally the choice due to its weldability, its ability to be corrosion resistant, but also due to its mechanical properties. Another alloy, SS ER 316L is also a valuable choice, due to its better mechanical properties and better resistance to corrosion, but the price over advantages ratio is usually in favour of the ER 308L. It is not a case in fact, that the famous bridge printed by MX3D is made of this material.

Since all the test performed so far by the referenced sources are based on SS alloy ER 308L, the only possible design assumption is to utilize this material in the model.

According to the studies conducted by TU Delft [6] and UNIBO [11] the feedstock material conserves most of its properties. More details about SS ER 308L used in the specimen can be found in Appendix V.

In the following sections the material properties of 3D-printed steel will be discussed. Note that the results refer to continuously printed columns as this is the production technique that has been assumed for the model that will be presented later.



Figure 13. Printing process of tubular specimens

4.4.1 Specimens and tests overview

3 types of specimens have been used for determining the material properties of 3D printed steel. Rectangular and plates have been tested in tension to determine the elastic modulus of the material. Tubular specimens have been tested in compression, bending and buckling to assess all the other mechanical properties.

However, before performing these destructive tests, some geometrical measurements have been performed. Figure 14 describes all the measurements that have been collected.

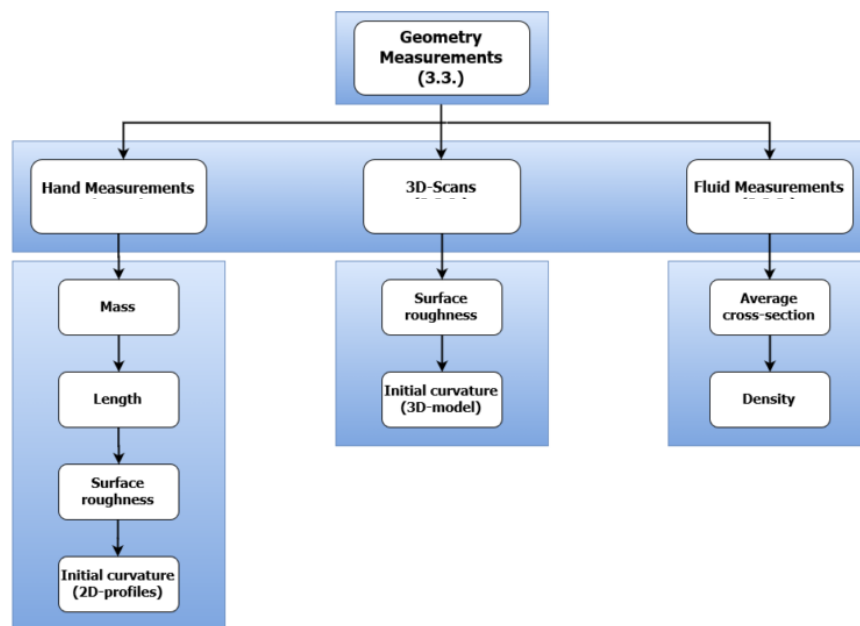


Figure 14. Diagram of geometrical measurements [6]

These tests provide the basic information to elaborate the data obtained from the mechanical test. Figure 15 summarises the mechanical tests that have been performed and their relative output.

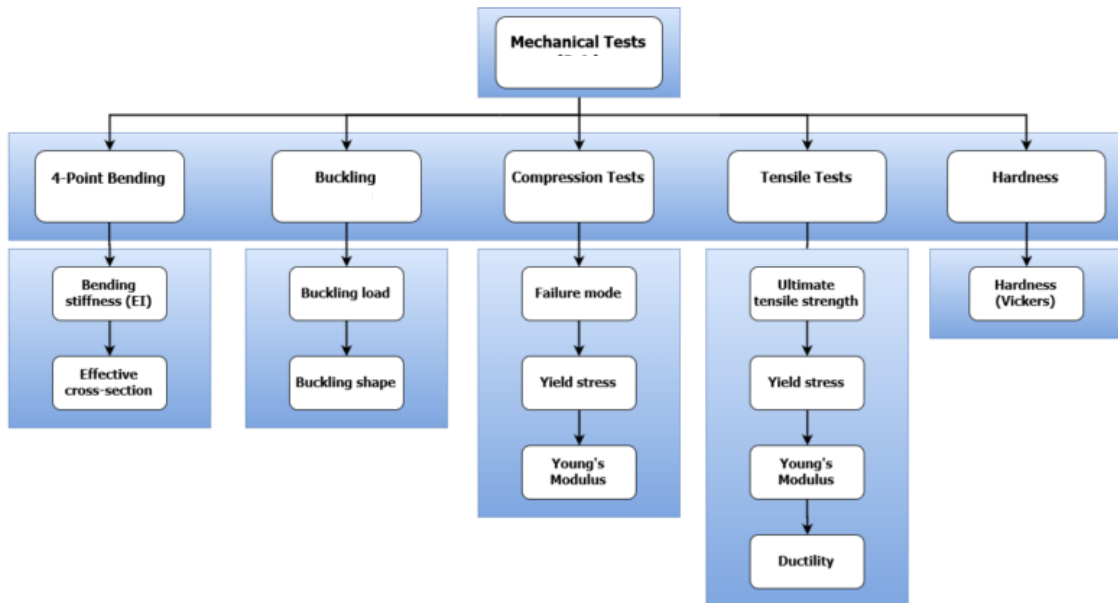


Figure 15. Mechanical tests and corresponding outputs [6]

4.4.2 Hand Measurements

These measurements have been performed with traditional mechanical tools like scale, square and paper. Mass and length of the specimens are the most important outputs of this analysis. However some other measurements can also be collected to have a rough idea of the general geometrical properties. Nevertheless, more advanced techniques have been used to refine these measurements.

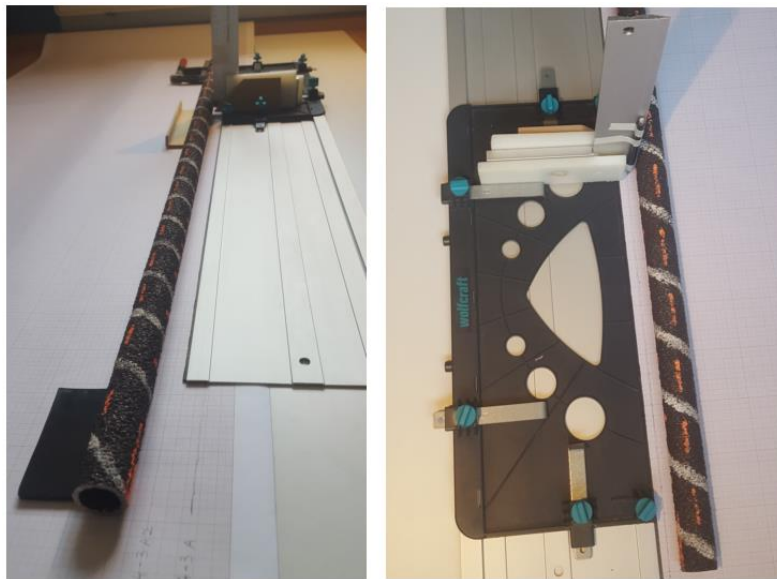


Figure 16 Set up for hand measurements [6]

4.4.3 Superficial imperfections

3D scans have been used to investigate the raw surface of plates and tubes and to check for misalignments in the axis of tubular specimens.

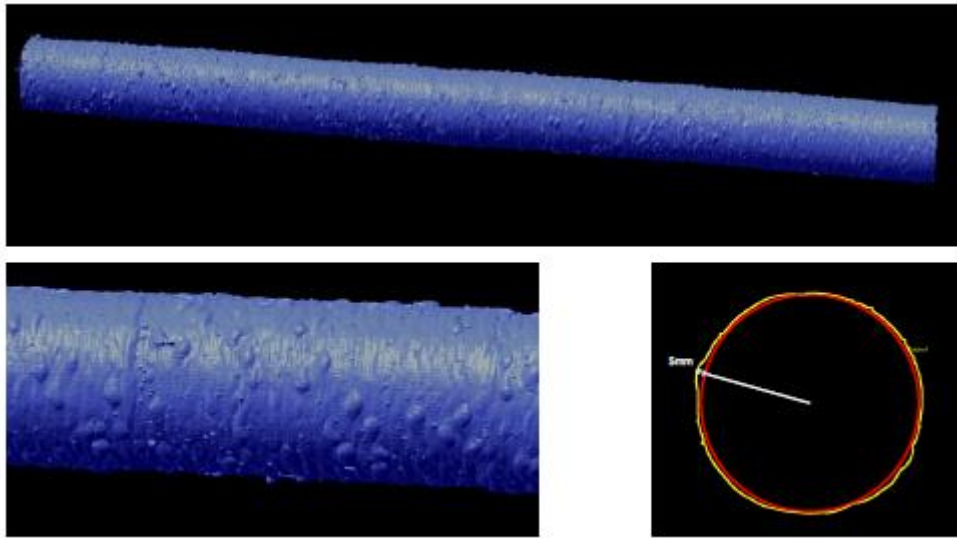


Figure 17. High resolution 3D laser scanning of tubular elements

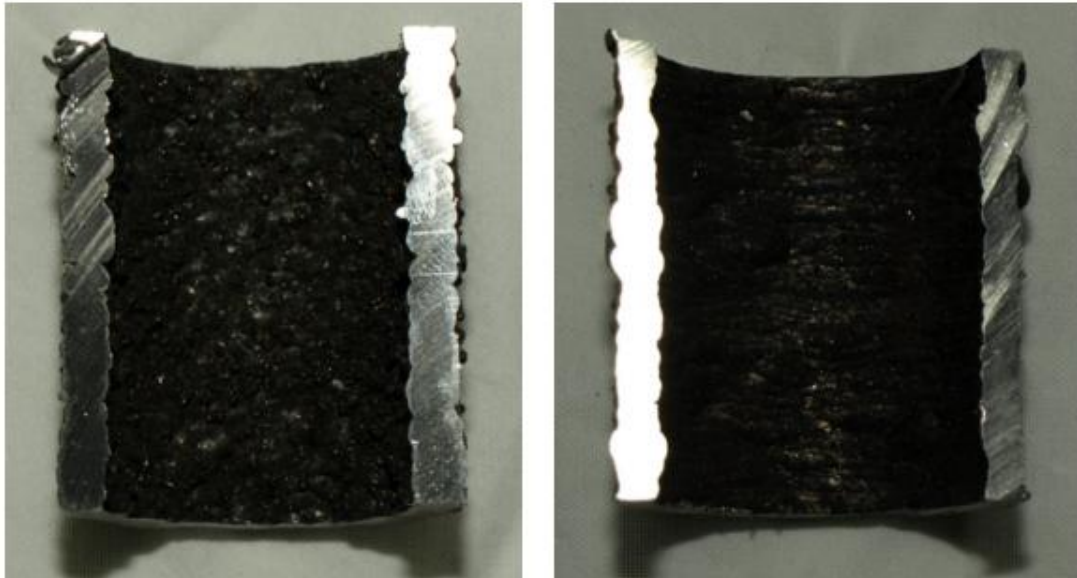




Figure 18. Investigation on the imperfections of the specimens [6]

This analysis is meant to define whether recursions can be identified in the pattern of the imperfections and eventually the leading parameters that generate such imperfections.

4.4.4 Density

Archimedes principle has been used to determine the total volume of the specimens. The specimens are totally submerged into a PVC tube with a known quantity of water. By measuring the increment in the level of water after the submersion of the specimen it is possible to retrieve the volume of the specimen.

Finally knowing the mass, also the density can be found. Measured densities on continuously printed elements stood at 7.94 g/cm^3 which is very close to the value of 7.90 g/cm^3 declared by the producer of the feedstock. [6]

4.4.5 Tensile test: Young Modulus- Yield and Ultimate Tensile Strength -

One of the key input of a structural model is the Young modulus of the material as it affects the stiffness of the elements. In order to determine its value a total of 35 tensile tests have been analysed by Van Bolderen and UNIBO. As highlighted in Chapter 4, the material properties are deeply influenced by the printing process hence two different typologies of specimens have been tested: one with the toolpath parallel to the testing direction (longitudinal,x) and one perpendicular (transversal,y).



Figure 19. Longitudinal (▲) and Transverse specimens (▶)

Table 2. Results of tensile test performed at UNIBO [11]

Specimen name	Yielding tensile strength	Ultimate tensile strength	Ultimate deformation	Young modulus
A-X	307 MPa	485 MPa	29.30%	99.21 GPa
B-X	307 MPa	533 MPa	27.91%	98.51 GPa
C-X	257 MPa	449 MPa	33.00%	103.14 GPa
D-X	285 MPa	511 MPa	39.96%	129.49 GPa
A-Y	270 MPa	439 MPa	22.25%	82.89 GPa
B-Y	290 MPa	469 MPa	21.68%	81.56 GPa
C-Y	269 MPa	485 MPa	20.38%	67.30 GPa
D-Y	262 MPa	481 MPa	23.84%	70.28 GPa

Table 3. Summary of results obtained by TU Delft [6]

	0.2% Proof Stress $\sigma_{0.2}$ [N/mm ²]	Ult. Tensile Strength σ_u [N/mm ²]	Young's Modulus E_0 [GPa]	Ultimate Strain ϵ_u [%]	Fracture Strain ϵ_f [%]
Oerlikon - as welded 20°C	>350	>520	-	>35	
Ugiweld - as welded 20°C	360	600	-	>35	
Longitudinal (print dir.)	307	544	137	21.2	22.0
St. deviation σ	5	28	6	3.5	3.8
Transversal	321	568	121	30.9	34.9
St. deviation σ	6	11	6	0.9	4.7

As we can see from Table 2 and Table 3, the results are quite variable. Since a unique value has to be chosen, in accordance with the assumptions made in [18], an average value of $E=100$ GPa and $f_y = 350$ MPa are assumed as design value for the FEM model.

4.4.6 Compression Tests: Young modulus, Yield and Compressive strength

Unibo performed compression tests to assess the behaviour of the material also in compression. Table 4 summarises the results for C-S areas measured with callipers. As we can see from the mean values reported in the last row, the values are far lower than traditional steel and those highlighted by the tensile test. The Young modulus, yield strength and ultimate strength are about 40%, 65% and 80% of the values of the feedstock material.

Unfortunately these results have been available only at the end of the research, hence there has been no time to include them in the model.

4.4.7 Imperfections

According to the wide experimental campaign conducted by the ECCS (European Convention for Construction Steelwork) on standard hot rolled, cold-formed and welded steel elements, there are three main sources of imperfections.

- Tolerances in the geometrical properties of steel products
- Residual stresses, due to uneven cooling of steel
- Variations of yield strength

From these tests, the curves reported in Figure 20 have been developed.

Table 4. Summary of results of compression test for measured cross sections

<i>I.D</i>	<i>A_m</i> <i>[mm²]</i>	<i>E_m</i> <i>[MPa]</i>	<i>F_{MAX}</i> <i>[kN]</i>	<i>f_y</i> <i>[MPa]</i>	<i>f_u</i> <i>[MPa]</i>
850 A	830.88	69865.96	327.56	228.68	394.23
850 B	838.14	69054.53	305.63	233.50	364.65
850 C	828.78	66513.10	208.70	214.31	251.81
1050 A	773.15	82033.50	289.93	230.19	375.00
1050 B	810.54	71916.22	305.16	235.38	376.50
1050 C	811.88	76878.37	279.69	237.27	344.49
1200 A	766.97	80222.87	303.38	244.55	395.56
1200 B	841.25	72603.90	254.74	212.31	302.82
1200 C	750.45	76959.24	304.34	242.01	405.54
		74005.30		230.91	356.73

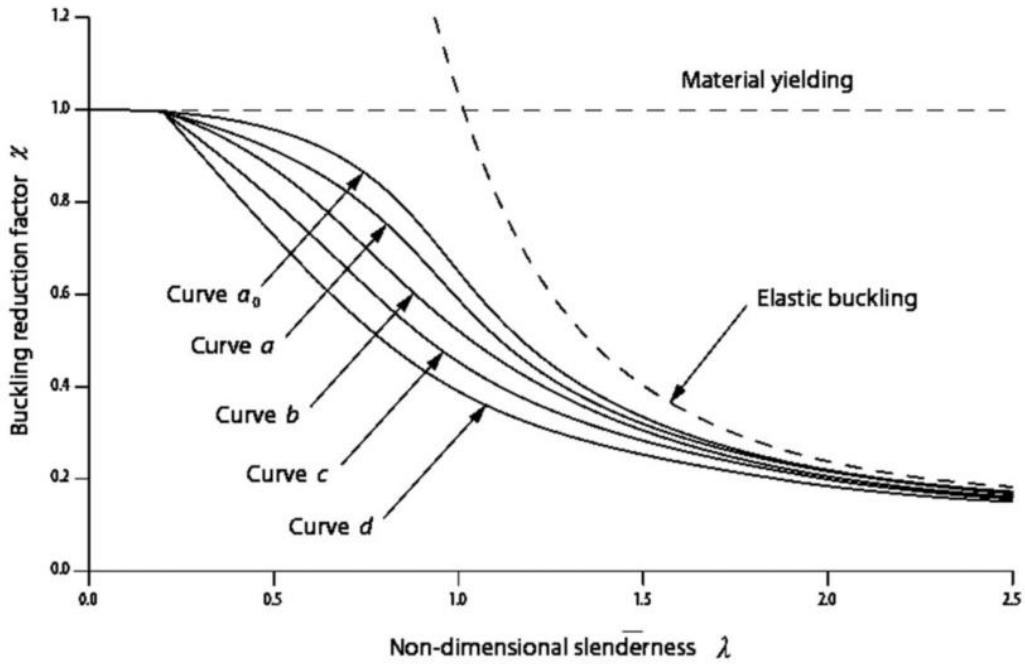


Figure 20. Buckling curves according to Eurocode 3

Where a_0 , a , b , c , d depend on the classification of Table 6.2 of EC3 (Figure 22).

However, these curves are not developed for 3D-printed elements. Hence TUDelft and UNIBO have performed also buckling tests on tubular specimens with different slenderness. The goal of this analysis was to identify the reduction factor as function of the member slenderness for 3D printed columns.

Figure 21 depicts the proposed curve. It has to be stressed that these curves have been developed with the assumption of $E = 100 \text{ GPa}$ and $f_y = 350 \text{ MPa}$ (retrieved from the test described here above).

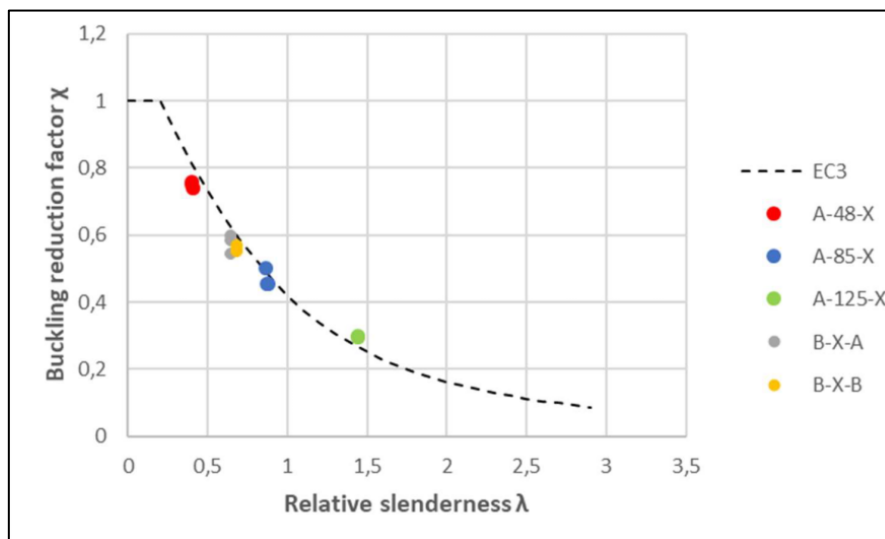


Figure 21. Interpolation of the experimental results for mean-2standard deviations with EC3 formulation ($\alpha = 1.00$; $\bar{\lambda}_0 = 0.2$) [18]

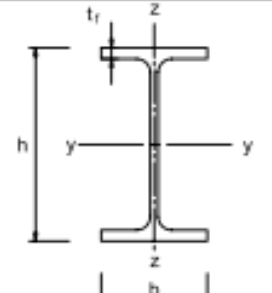
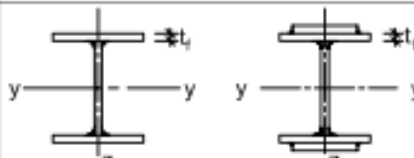

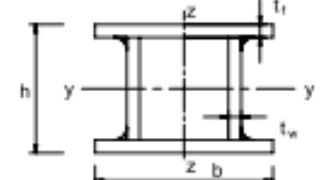
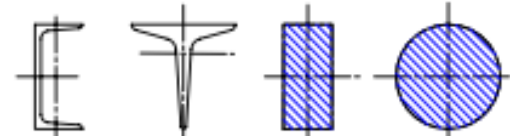

Cross section	Limits	Buckling about axis	Buckling curve		
			S 235 S 275 S 355 S 420	S 460	
Rolled sections 	$h/b > 1,2$	$t_f \leq 40 \text{ mm}$	y-y z-z	a a ₀	a ₀ a ₀
		$40 \text{ mm} < t_f \leq 100$	y-y z-z	b c	a a
	$h/b \leq 1,2$	$t_f \leq 100 \text{ mm}$	y-y z-z	b c	a a
		$t_f > 100 \text{ mm}$	y-y z-z	d d	c c
Welded I-sections 	$t_f \leq 40 \text{ mm}$	y-y z-z	b c	b c	
	$t_f > 40 \text{ mm}$	y-y z-z	c d	c d	
Hollow sections 	hot finished	any	a	a ₀	
	cold formed	any	c	c	
Welded box sections 	generally (except as below)	any	b	b	
	thick welds: $a > 0,5t_f$ $b/t_f < 30$ $h/t_w < 30$	any	c	c	
U-, T- and solid sections 		any	c	c	
L-sections 		any	b	b	

Figure 22. Table 6.2 EC3

5 STRUCTURAL OPTIMIZATION

With the growth of the population and the limited amount of resources on planet Earth, the reduction of the usage of material in becoming more and more important. The goal of structural optimization (SO) is exactly this: assess where the material is most needed within a domain to achieve a specific task.[19] SO is suitable to achieve the following tasks:

- Minimum cost
- Minimum weight
- Resources usage
- Limitation of stress concentrations
- Limitation of displacements (stiffness)

Three different levels of SO are usually recognised in literature [19]:

- Topology Optimization: most general form of optimization, defines where higher material densities are needed.
- Shape Optimization: allows to identify form and contour of the domain.
- Size Optimization: the design is known, only the size of the components needs be determined.

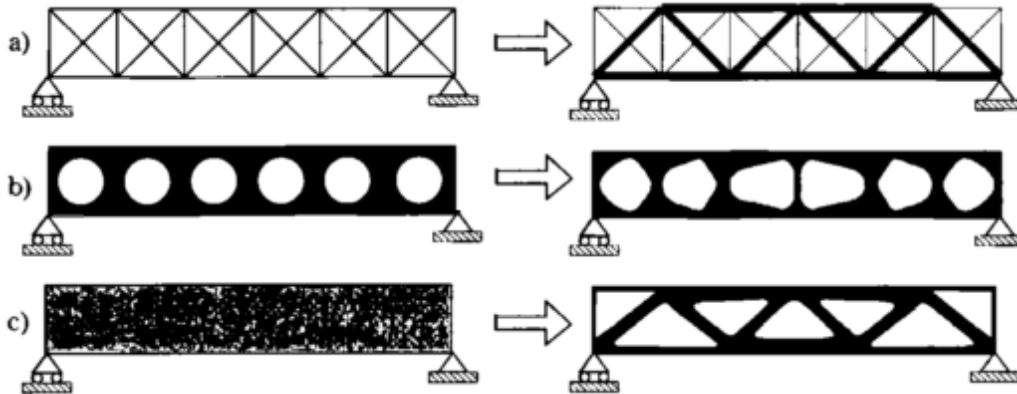


Figure 23. Example of different levels of optimization. a) Size optimization of a truss, b) Shape optimization of holes in a beam, c) Topology optimization for a simply supported beam. [20]

5.1 MATHEMATICAL PROGRAMMING PROBLEM

The word “optimization” itself has no meaning unless a goal is set. This is usually performed by defining a so called “*objective function*” $f(x)$. Hence the structural optimization problem can be reduced to the following stamen [21]:

Find x , to minimize $f(x)$, subject to $g(x) \leq 0$.

where $f(x)$ is a scalar, x is n -dimensional vector and g , the “*constrain function*”, is an m -dimensional vector and can be rewritten as:

$$g(x) \leq 0 = \begin{cases} g_1 \leq 0 \\ g_2 \leq 0 \\ \vdots \\ g_m \leq 0 \end{cases}$$

These constrains can have multiple origins:

- Geometric constraints: due to external limitations in the domain
- Technological constraints: due to production or construction issues
- Performance constraints: to ensure minimum performances with respect to other functions.

5.2 MULTI-OBJECTIVE OPTIMIZATION

Usually in real life problems tools are required to satisfy multiple requirements. Despite boundary values can be set as constrains for a single objective optimization, it is usually necessary to find a balance between the optimum solution with respect to an objective and the general performances of the object. Here is where the multi-objective optimization starts to play.[22]

In general Multi-Objective Optimization (MOO) is applied when a trade-off of the objectives is needed. The classic example is the minimization of the weight of a structure and the maximization of the stiffness. As a general rule, the more material we remove, the smaller the stiffness, the higher the displacements. If we want to achieve our goal a balance has to be found between the removal of material and the reduction of the stiffness. In order to have a quantitative evaluation of which design leads to the optimum design, a new mathematical problem has to be written.

The mathematical multi-objective problem can be formulated as:

$$\begin{cases} \text{minimize} & F(x) = (f_1(x) \dots f_{n_f}(x)) \\ \text{subject to} & G(x) = (g(x) \dots g(x)) \\ \text{with} & x \in \mathbb{R}^n \end{cases}$$

The solution of this mathematical problem has been widely studied by Pareto, an economist lived in the 19th century[23]. After his studies he formulated the following principle [24]:

“ A Pareto optimal solution is one for which any improvement in one objective will result in the worsening of at least one other objective. Mathematically, a point f^* (which is a vector of length n_f) is called Pareto optimal if there does not exist a point f^p in the feasibility domain such that:

$$f_j^* \geq f_j^p \quad \forall j$$

$$f_j^* > f_j^P \quad \text{for at least one } j$$

“

The set of all the Pareto optimum solutions is then defined as the “*Pareto front*”.

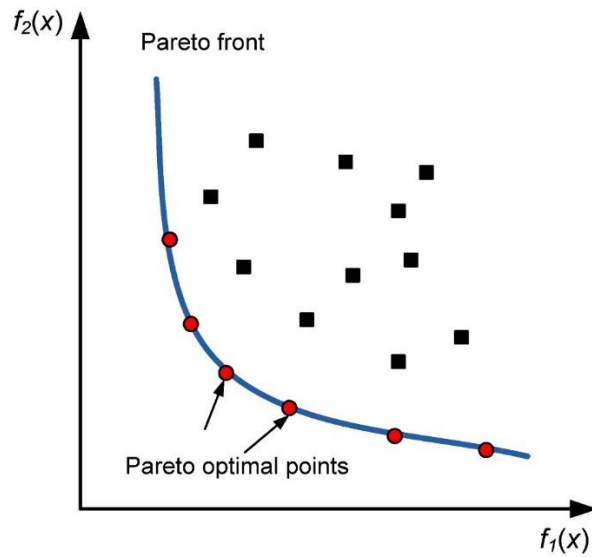


Figure 24. Geometric diagram of Pareto Front [25]

Mathematically, none of the Pareto solution is objectively better than any other solution. [24] To define the most suitable for the design, subjectivity has to be introduced. So, the final choice is in the hands of the designer. However, some quantitative evaluations are usually artificially created. The general approach is to generate utility functions with arbitrarily defined weighting factors (here is the subjectivity).

There are different types of utility functions in the literature, however the most utilized are:

- weighted sum
- exponential weighted sum

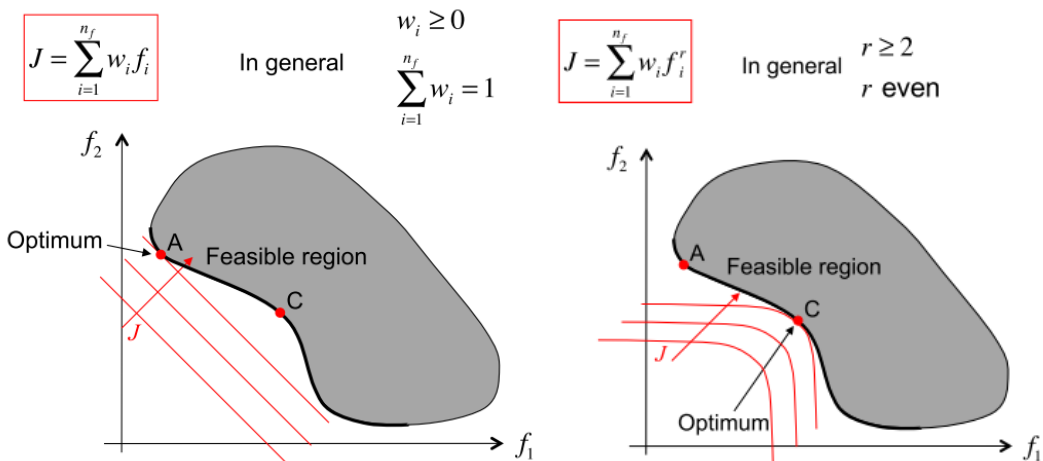


Figure 25. Pareto front and utilities function approach, weighted sum and exponential weighted sum [24]

However, as shown in Figure 25, if the domain has some convexities, these solutions could lead to a limitation in the possible achievable solutions and hence in a reduction options for the designer.

A more general, but also complex, approach is also available to designers to identify the whole Pareto front. The so called “objective function normalization”, that consist in scaling the objective functions so that the Pareto front falls into a hypercube of unitary side can also be applied.

$$f_i^{j^*} = [f_i^{1^*}, f_i^{2^*}, \dots, f_i^{n_f^*}]^T \quad i = 1, \dots, n_f$$

The transformed domain is given by:

$$\bar{f}_i(\mathbf{x}) = \frac{f_i(\mathbf{x}) - \min_j f_i^{j^*}}{\max_j f_i^{j^*} - \min_j f_i^{j^*}}$$

$f_i^{j^*}$: value of f_i obtained minimizing separately f_j subject to constraints

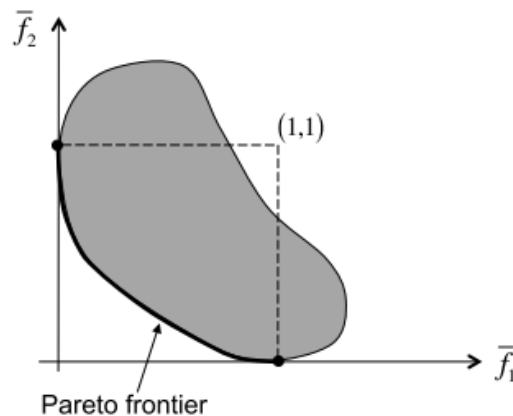


Figure 26. Objective function normalization approach [24]

Nowadays, thanks to the computer aided design, the convergence to the Pareto front can be “guided” to the desired solution. This method is the so called “Goal Programming” and consists in allowing the designer to specify a target value and two weights w , that represent the slopes of the preference functions, one per side of the target value. Any deviation (d) from the target value leads to an increase of the preference function value that is proportional to the weights. The program then tries to converge to the solution that minimizes the sum of the preference functions.

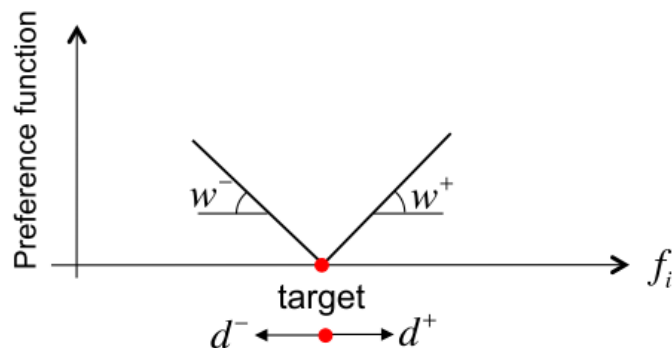


Figure 27. Graphical explanation of the definition of the deviation d for Goal Programming [24]

6 CASE STUDY: ZLOTE TARASY

6.1 OVERVIEW OF THE BUILDING

The building under analysis is located in Warsaw, Poland. The Zlote Tarasy, “Golden Terraces” in English, takes its name from the street where the building is located: Zlota Street. The building has been structurally designed by Aroup for ING Real Estate with the goal to enrich the city centre of the city with multi-purpose centre. 40 000m² of underground car parking, 6000m² truck service yard, 24 000m² of offices, 54 000 m² of restaurants, retail and department stores, eight cinema halls and a 780 seats auditorium, 14 000m² of public areas and malls, 6000m² of terraces and gardens, for a total area of 200 000m², these are the numbers the Zlote Tarasy.

The space is organised as depicted in Figure 28. As we can see there are 6 main areas: two office blocks: the “Lumen” and the “Skylight”, the roof terrace, the food court, the “Drum” (a 3-storey tower containing all the escalator to allow connection between the car park and the different floors) and the Cinema. [26]

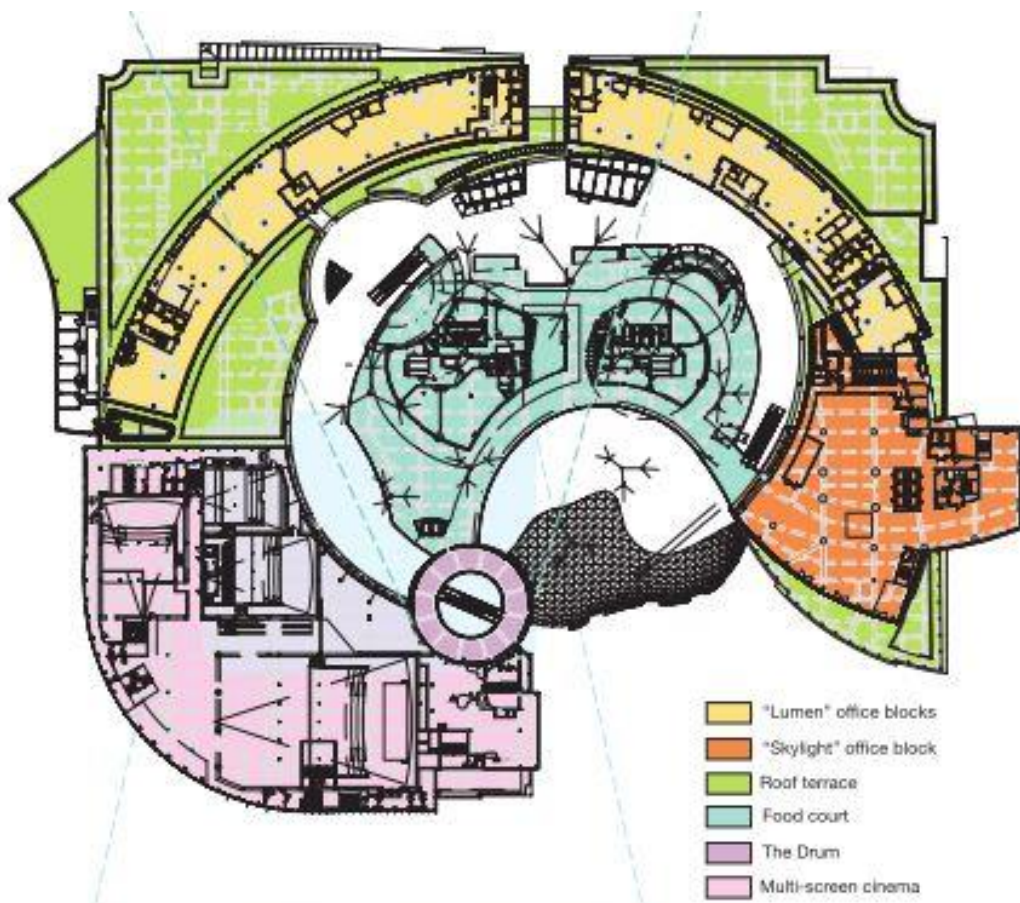


Figure 28. Conceptual distribution of the areas and aerial view of the complex [26] [27]

6.2 THE ATRIUM ROOF

6.2.1 The concept

One of the main peculiarities of this complex is the roof of the atrium that hosts part of the retails and the food court. Its iconic design has been proposed by Jerde Partnership with the purpose of giving the customers the idea of walking in a tree forest. This feeling is further strengthened by the shape of the dendriform columns. The concept has been developed via a computational simulation of the falling of a cloth over series of spheres. From this simulation a series of geometries have been extracted and the most suitable, a 8-domes canopy, has been finally chosen for the architectural design.



Figure 29. The “cascade”, external view of the atrium [28]

6.2.2 Geometry and Structural Properties

The atrium roof develops on an elliptical plan, 160m long and 100 m wide, for a total covered area of $10\,240\text{m}^2$ and reaches about 35m above the ground level. According to Arup [26], it is made of 7123 200mmx100mm steel RHS beams with variable steel class and thickness, 2300 steel nodes and 4788 glass panels, none of them equal to the other. The result is a grid shell with a variable triangular mesh.

Some attempts have been made to standardise the geometry, in order to allow the repetition of similar elements and cut the costs, but the architectural design and other design constrictions, such as the water drainage of the roof, the snow sliding, and the smoke concentration required such a free form grid made it impossible.

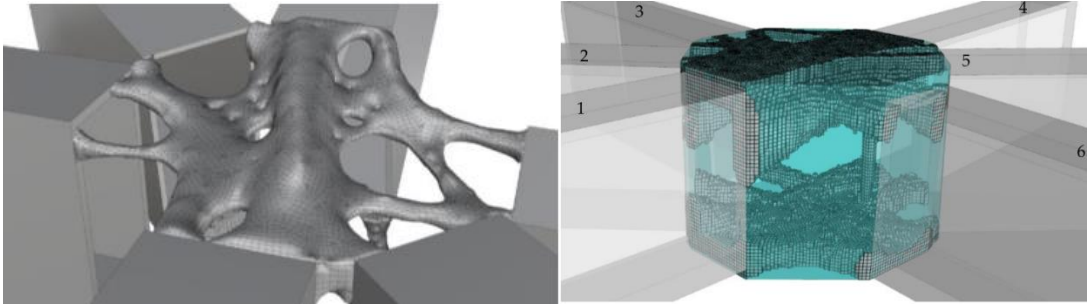


Figure 30. Topology optimization studies applied to the nodes to investigate the possibility of 3D printing customized nodes for the building [4]

Another relevant constrain that led to this choice is the complexity of the support. The structure is supported at different levels both due to its irregular shape but also due to the its “hugging” function among all the nearby buildings. The final design required a complex combination of supporting structures: 11 internal tree-like columns, 26 perimeter posts at level 3, 2 sliding bearings at the drum, 2 rotational bearings, 2 “flying struts”, and 16 supports at the base of the cascade.

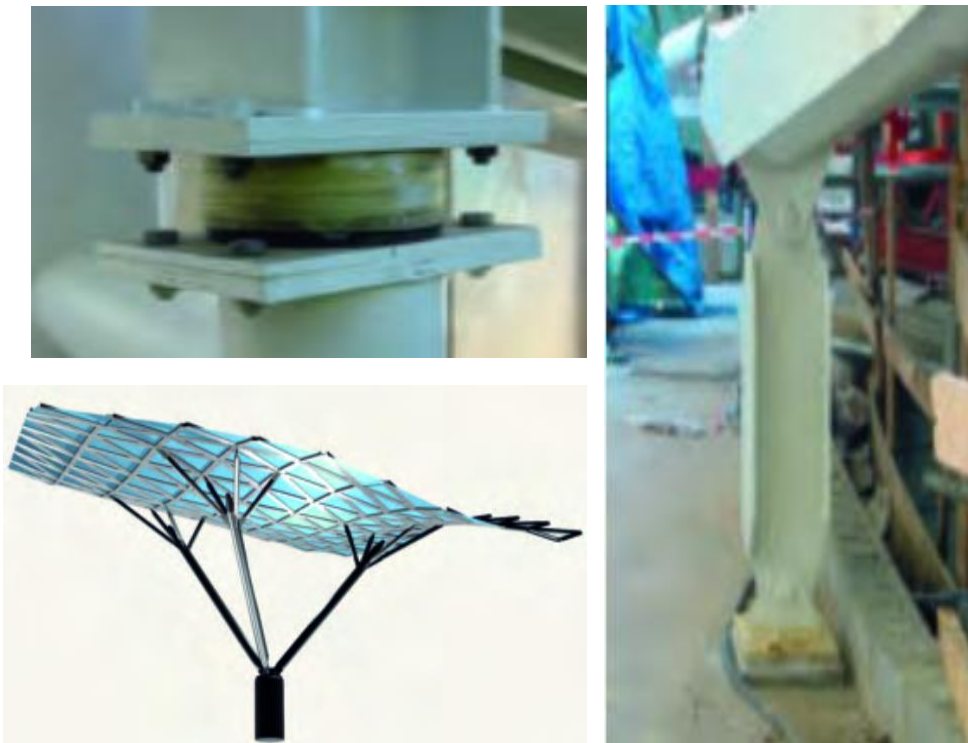


Figure 31. Atrium roof supports[26]

These solutions are the outcome of a complex design study aimed to ensure the structure to be:

- structurally efficient, minimising displacements and stress concentrations due to thermal expansion of steel
- architectonically appealing and visually “light”
- easy to maintain

6.2.3 Branched Columns

The over 100m span of the roof required some internal supports. A total of 11 tree-like columns has been carefully placed in order to minimize displacement and stresses but also to ensure a clear view of the walkways.

Each tree is composed of a trunk, a tapered 2m high steel tube filled with reinforced concrete, 3 primary branches, each of these diverging into other 4 secondary branches. All the branches have different inclinations and are made of tubular steel beams of different lengths.

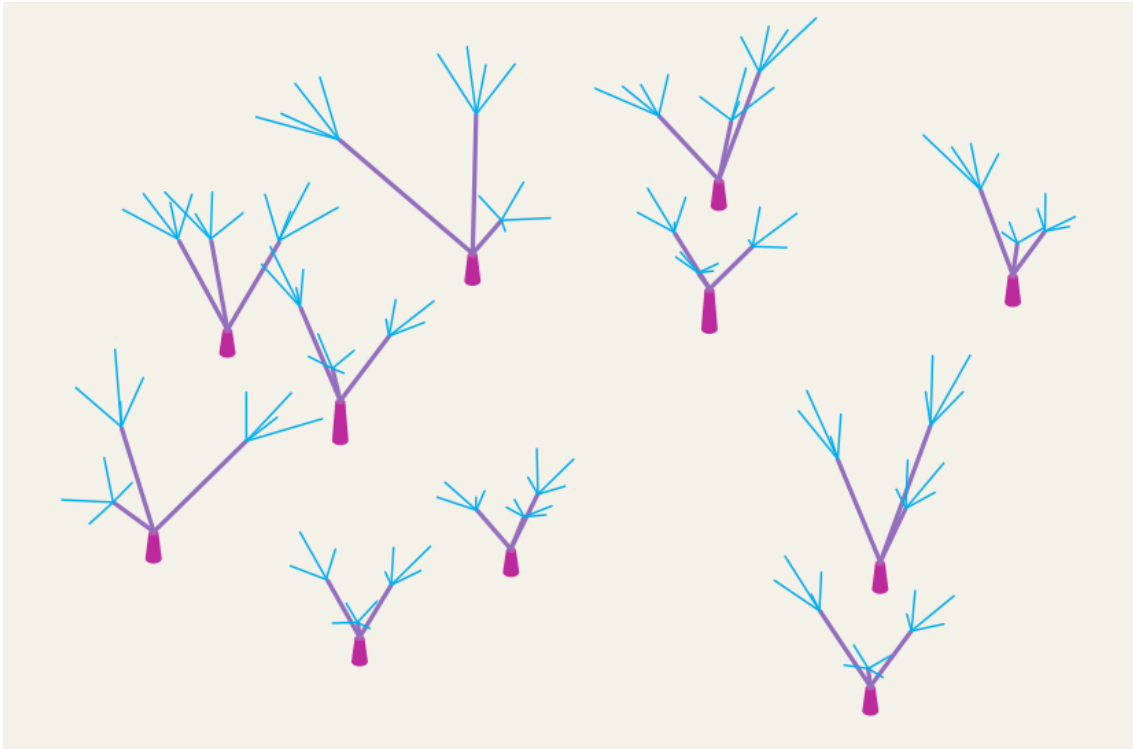


Figure 32. Dendriform roof supports

6.3 STRUCTURAL PROPERTIES OF THE ELEMENT

Since the objective of this study is to define an optimization method, a simple but significant case has been chosen. A slender simply supported column working in compression has been chosen as case study.

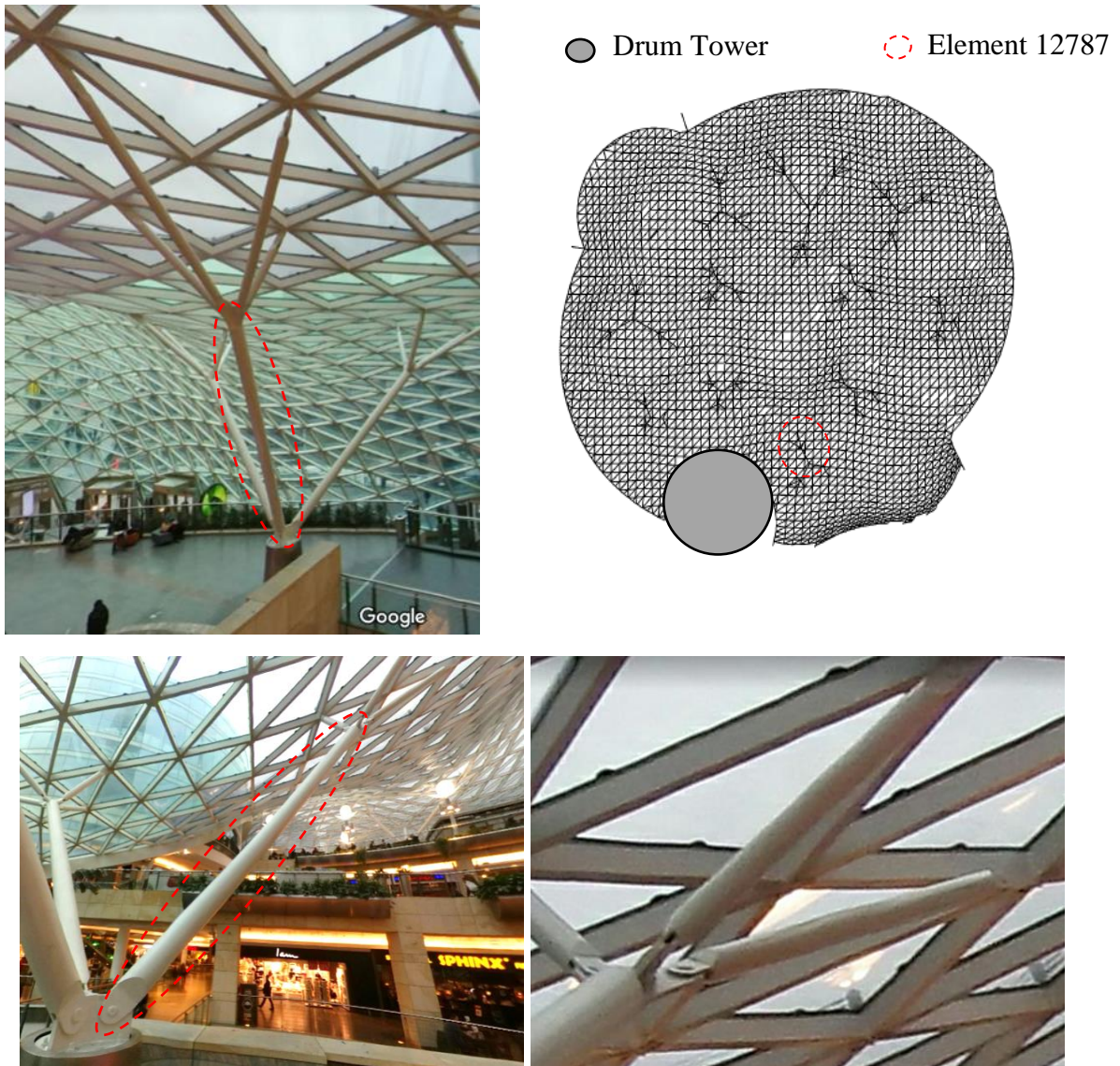


Figure 33. Overview of the dendriform column and detail of element 12787 and connection [29]

The structural details of the element have been retrieved from the GSA [30] structural model used by Arup for the design. Due to the complexity of the canopy over 1700 ULS load cases have been applied to over 7000 beams, making it the biggest GSA structural model ever analysed by Arup at that time. [26]

The element chosen is the first order branch of the tree that is closest to the drum tower. The element is a CSH273x12.5 tubular section with a total length (L_0) of 7m.

SECTION PROPERTIES		MATERIAL PROPERTIES	
Type	CSH273x12.5	Type	S355
\emptyset (mm)	273	E (MPa)	205
t (mm)	12.5	ν	0.3
m (kg/m)	80.3	G (MPa)	77850
A (cm ²)	102	γ (kg/m ³)	7850
I_{yy} (cm ⁴)	8697	α (/°C)	1.20E-05

As discussed in Appendix I, dendriform structures are usually designed so that they work only in compression. Seems like this approach has been followed also by the Arup designers as shown by the choice of the restrains in the structural model. Both the connection with the trunk and with the second order branches are pinned.

RESTRAINS		
Direction	Top	Bottom
Tx	Fix	fix
Ty	Fix	fix
Tz	Fix	fix
Rx	Fix	fix
Ry	Release	Release
Rz	Release	Release

Looking at Figure 33, in particular at the picture of the connection with the minor branches, we can observe that the axes of rotation of the connections are not aligned, hence, assuming that the roof is stiff and that the elevate number of minor branches offer a stiff connection with the roof (all connections of the grid shell are bending resistant), we can assume that the only degree of freedom allowed is along the axis of the beam.

According to these assumptions, the structural system for the single branch has been simplified to the scheme reported in Figure 34.



Figure 34. Structural system assumed for the analysis

COMPUTATIONAL MODEL AND OPTIMIZATION ALGORITHM

7 STRUCTURAL ANALYSIS FOR PARAMETRIC DESIGN

7.1 PARAMETRIC DRAWING

The possibilities open by additive manufacturing require CAD programs with high flexibility. At the time being, few software packages are capable of such a flexibility. Rhinoceros [31] in combination with Grasshopper [32] are probably the most used in the Building industry. Parametric design is a fundamental tool to achieve and mathematically describe complex shapes. At the same time, it offers an incredible flexibility as changing few parameters completely new forms can be found.

On the other hand, free form design has some drawbacks. Sometimes the complexity of the shapes is so high that the physical and engineering sense can be lost. Hence it is fundamental to ensure that the developed geometry is physically possible. Later on, an example of how geometrical and physical compatibility must be verified will be discussed (see Chapter 8.8).

Another drawback is that traditional FEM software packages are not suitable to draw such complex geometries so usually CAD models have to be converted into a format readable by the FEM software and then imported. However, this process is usually not so smooth as not always the CAD software can export in the desired format, hence intermediate steps are needed and the risk of losing accuracy and details gets higher and higher. Furthermore, whenever changes on the design needs to be performed, the process has to be repeated over and over again.

For this reason, Karamba [33], a FEM software fully embedded in the Grasshopper environment, has been used for solving the structural analysis for the optimization problem.

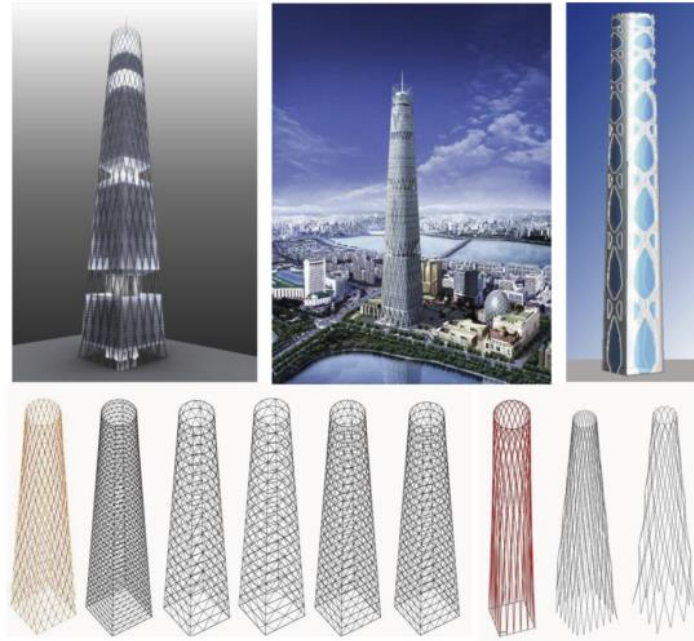


Figure 35. Parametric studies for the design of the Lotte tower, retrieved from [34], based on [35]

7.2 NON-LINEAR ANALYSIS

7.2.1 Non-linear analysis in GSA

Karamba offers a variety of possible types of structural analysis and tools to examine the results. Due to the imperfections associated to the printing process a non-linear analysis was the only choice for the analysis.

Differently from a linear analysis, in a non-linear analysis the load is applied incrementally. At each step, the stiffness matrix, loads and displacements are computed in order to find the following equilibrium state and update the input for the following iteration. This allows to include geometrical, material and constrains non-linearities.

When large deformations occur, the assumption of small displacements is no more true, hence the deformed shape, the geometrical non-linearity, has to be taken into account. Similarly, when the material is subjected to high stresses and deformations the assumption of a linear relation between the two units is no more realistic. Hence different models need to be included.

Finally, loading and boundary conditions may be affected by the behaviour of the system (displacements or actions). Hence, these behaviours can be captured with the iterative process of a non-linear analysis.

The drawback of a non-linear analysis is that, due to the iterative process, is computationally much more expensive than a traditional linear analysis, where the solution needs to be computed only once.

For the optimization process only geometrical non linearities will be considered as plastic analysis is not implemented in the software and the constrain condition are assumed to be

independent from the behaviour of the system. Details on how the non-linear analysis is implemented in Karamba can be found in Rubin's work. [36] [37]

However, for steel structures plastic analysis is fundamental hence, in order to perform a complete analysis and verify the results obtained in Karamba, non-linear analyses with both geometrical and material non linearities have been used. For this purpose, Oasys GSA[30] has been used. According to the user manual, the software uses the relaxation method to perform the analysis.

This involves the following steps[38] :

- 1. Compute equivalent nodal forces and moments. In this process, member loads are converted into nodal force or moments. These are the forces that initiate vibration.*
- 2. Construct dummy mass and dummy inertia for the unrestrained (active) nodes according to the translational and rotational stiffness of the members at the nodes*
- 3. Compute the acceleration, speed and displacement for each node at each cycle.*
- 4. Compute a new nodal position and rotation for each node at each cycle; update the nodal stiffness and member force acting on the nodes.*
- 5. Check the force and moment residuals at each node at the current position.*
- 6. If no residual exceeds the limit, the analysis is considered to have converged and the final position is considered as the equilibrium position of the structure.*
- 7. If any residual is not satisfied, the analysis is continued to the next step.*
- 8. Compute the total kinetic energy of the structure. If the kinetic energy at a cycle overshoots the maximum, it is considered that the equilibrium position has been passed. Therefore, all nodes will be re-positioned so that they are closer to the equilibrium position. Reset the speed and acceleration to be zero and let the structure start to vibrate again from the new position.*
- 9. After analysis has been converged, the element forces, moments and stresses are calculated according to the final equilibrium position of the nodes.*

7.3 SECOND ORDER EFFECTS

According to EN 1993-1-1: 2005 (E) chapter 5.2, the second order effects (deformed geometry) and initial imperfections should be included if they affect significantly the structural behaviours. The verification can be performed totally by global analysis, partially by global and local analysis, or, for simple structures, by individual check on individual members using buckling length according to the buckling mode of the structure. Another option is to take into account second order effects is to apply equivalent forces to destabilize the structure. Figure 36 depicts, how to implement these forces.

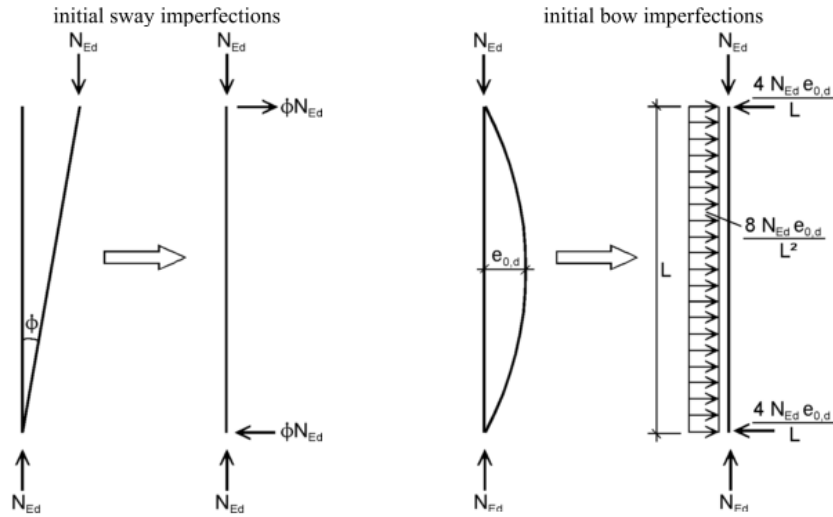


Figure 36. Equivalent forces for modelling global imperfections of frames

For traditional columns, the initial crookedness e_0 can be retrieved from Table 5.1 of EN 1993-1-1: 2005 (E), and L is the actual length of the member. However, since we are dealing with 3D-printed steel elements a different value has to be assumed. University of Bologna (Unibo) conducted some tests on WAAM columns. The results are summarized in Table 5.

Table 5. Summary of e_0 , based on UNIBO [18]

SPECIMEN I.D	L/x
850-A	137
850-B	137
850-C	149
1050-A	204
1050-B	172
1050-C	172
1200-A	196
1200-B	175
1200-C	128

Since a unique value has to be assumed, the average value of all the tested specimens will be assumed, hence from now on $e_0 = L/157$.

The sway imperfection can be computed instead as

$$\Phi = \Phi_0 \alpha_h \alpha_m$$

Where:

$$\Phi_0 = 1/200 \quad (\text{basic value})$$

α_h is a reduction factor due to height of the structure h (in meters):

$$\alpha_h = \frac{2}{\sqrt{h}} \quad \frac{2}{3} < \alpha_h < 1.0$$

α_m is a reduction factor that takes into account that the more the columns in a row, the smaller the sway effect:

$$\alpha_m = \sqrt{0.5 \left(1 + \frac{1}{m}\right)}$$

However, due to the properties of the system, the sway imperfections have not been considered. Only global imperfections, on the axis of the column, have been used instead.

7.4 INITIAL IMPERFECTIONS OF STEEL COLUMNS

Chapter 6.3 of EN 1993-1-1: 2005 (E), suggests also a procedure to estimate the reduction in strength of steel columns due to the initial imperfections introduced by the production process of steel elements.

The verification for buckling of uniform members in compression is based on the following formula:

$$\frac{N_{Ed}}{N_{b,Rd}} \leq 1.0$$

Where N_{Ed} is the design value of the compression force and $N_{b,Rd}$ is the design buckling resistance of the compression member, defined as (Class 1,2,3):

$$N_{b,Rd} = \frac{\chi A f_y}{\gamma_{M1}}$$

Where $\chi \leq 1$ is the reduction factor that takes into account the imperfections.

χ can be computed as:

$$\chi = \frac{1}{\Phi + \sqrt{\Phi^2 - \bar{\lambda}^2}}$$

With:

$$\Phi = 0.5 \left[1 + \alpha(\bar{\lambda} - 0.2) + \bar{\lambda}^2 \right]$$

$$\bar{\lambda} = \sqrt{\frac{A f_y}{N_{cr}}}$$

Where N_{cr} is the Eulerian load $N_{cr} = \pi^2 \frac{EI}{(kL)^2}$ and k is a factor depending on the boundary conditions of the element.

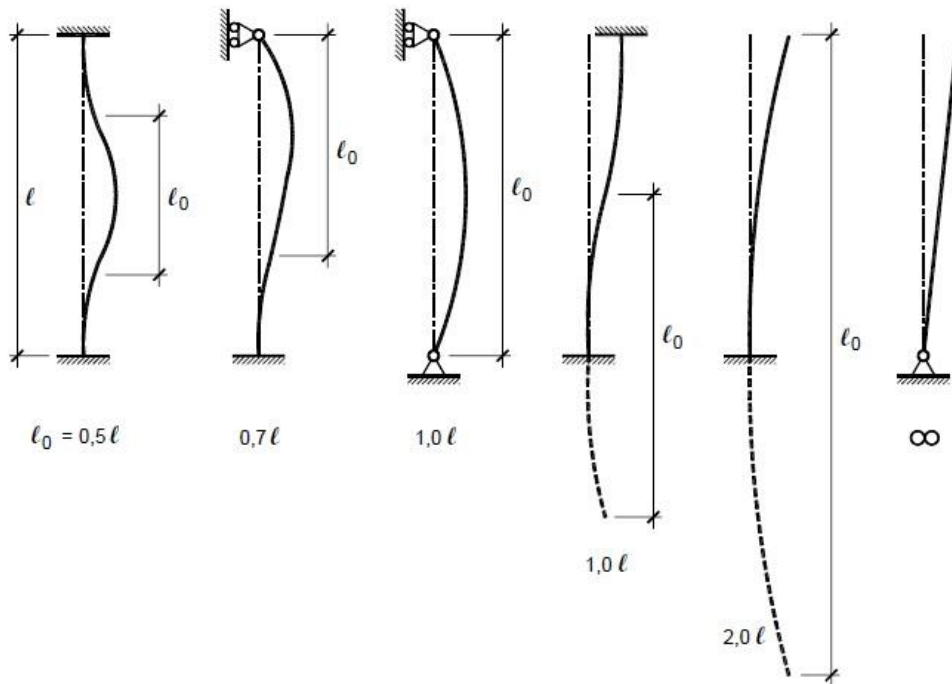


Figure 37. *k* coefficients for different boundary conditions

Finally, the imperfection factor, α , can be retrieved from Table 6.1 of EC3 according to the classification of the Table 6.2 of EC3 (Figure 22).

Table 6. EC3: Imperfection factors for buckling curves

Buckling curve	a_0	a	b	c	d
Imperfection factor α	0,13	0,21	0,34	0,49	0,76

8 SETTINGS AND CALIBRATION OF THE MODEL

8.1 LOADING CONDITIONS AND MATERIAL

In order to make a fair comparison between the original element, made of a traditional hollow cross section, and a 3D printed element, the two elements have to be designed for the same loading conditions. Therefore, the structural model highlighted in Chapter 6.3 have been applied to study the buckling load of the column.

Table 8 summarises the results obtained by applying the procedures reported in Chapter 7.4, to the properties of the column (summarised in Table 7).

Table 7. Input values for buckling analysis of original column

<i>Geom properties</i>		<i>Section properties</i>		<i>Material properties</i>		<i>Imperfection properties</i>		
L (mm)	K	A (cm ²)	I (cm ²)	E (MPa)	f _y (MPa)	Curve	α	γ _{M1}
6963	1.00	102	8697	205000	355	C	0.49	1

Table 8. Numerical results for buckling analysis with initial imperfections

<i>N_{cr}</i> (KN)	<i>λ̄</i>	<i>Φ</i>	<i>χ</i>	<i>N_{b,R,d}</i> (KN)
3'629.36	1.00	1.19	0.54	1957

Hence the design load used for the structural analysis P , will be assumed as $P = P_0 = 1957$ kN. Furthermore, the self-weight of the structure has been considered as additional loading condition in order to trigger the buckling of the column in a specific direction and assign the imperfections accordingly. (see Figure 49 for direction of g force)

As already anticipated in Chapter 4.4.5, the material properties are assumed according to the properties identified by previous researches and EC3:

$$E = 100 \text{ GPa}$$

$$f_y = 350 \text{ Mpa}$$

$$v = 0.3$$

8.2 TOPOLOGY OPTIMIZATION

A verification with a Topology optimization tool [39] have been performed to assess the optimal distribution of material to withstand a vertical load acting along an axis. The tool utilizes the density approach implemented in [20] to a 4 nodes finite element mesh used to solve the elasticity problem. More information about how the tool is implemented can be found in the link reported in reference [39].

As we would expect, for the problem under analysis the material needs to be distributed along the thrust line, that for this simple case, is the straight line that connects load and supports. However, since we are dealing with a continuous, the solutions are infinite as there are infinite shapes according to the amount of material that is to be removed. Thus,

further research is needed to assess how much material can be removed without compromising the safety of the column.

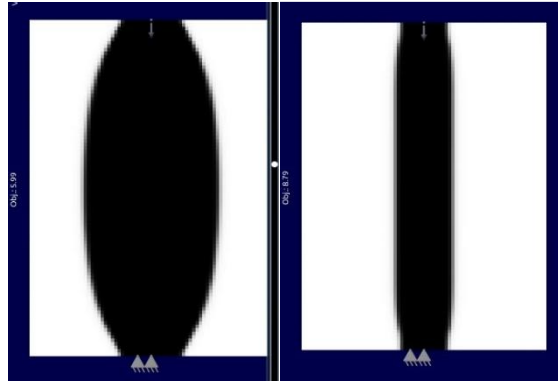


Figure 38. Results of topology optimization for 50% and 70% volume reduction respectively.

8.3 SHAPE OPTIMIZATION

As discussed above, there are infinite feasible shapes for the problem under analysis. Hence an investigation of the optimal has been made.

In order to define univocally the external shape of the column mathematical functions are needed. As a general formulation the external shape has been defined as the surface of revolution described by:

$$R(x) = r_r + a p_i(x)$$

where a is the shape amplification, that describes how stocky the column is, x , is the coordinate of the point along the axis, and $p_i(x)$ that is a mathematical function (pattern) that describes the shape of the column.

Finally, r_r , the reference radius, describes the radius of the column at the extremities. In fact a minimum radius is needed both at the top and at the bottom to ensure that there is sufficient room for the minimum quantity of material needed to withstand the load. At the same time, we have to consider that the branch has to be connected to the other branches and to the trunk, hence a minimum area has to be ensured for the constructability of the connection. $r_r = 100mm$ has been assumed as minimum radius to ensure the correct load transfer from the connection to the column. However, it is to be said that this is a pure assumption based on the observation of the size of the elements constituting the tree-like columns.

This minimum radius has been compared with the minimum radius to prevent yielding of the column.

$$\frac{N}{A} = \frac{P_0}{A} \sigma_{max} = f_y$$

$$\frac{N}{f_y} = \frac{1957 \text{ kN}}{350 \text{ MPa}} = A_{min} = 1780 \text{ mm}^2$$

According to this result the minimum r_r to prevent yielding is 42.2 mm that is smaller than the radius assumed for constructability of the connection.

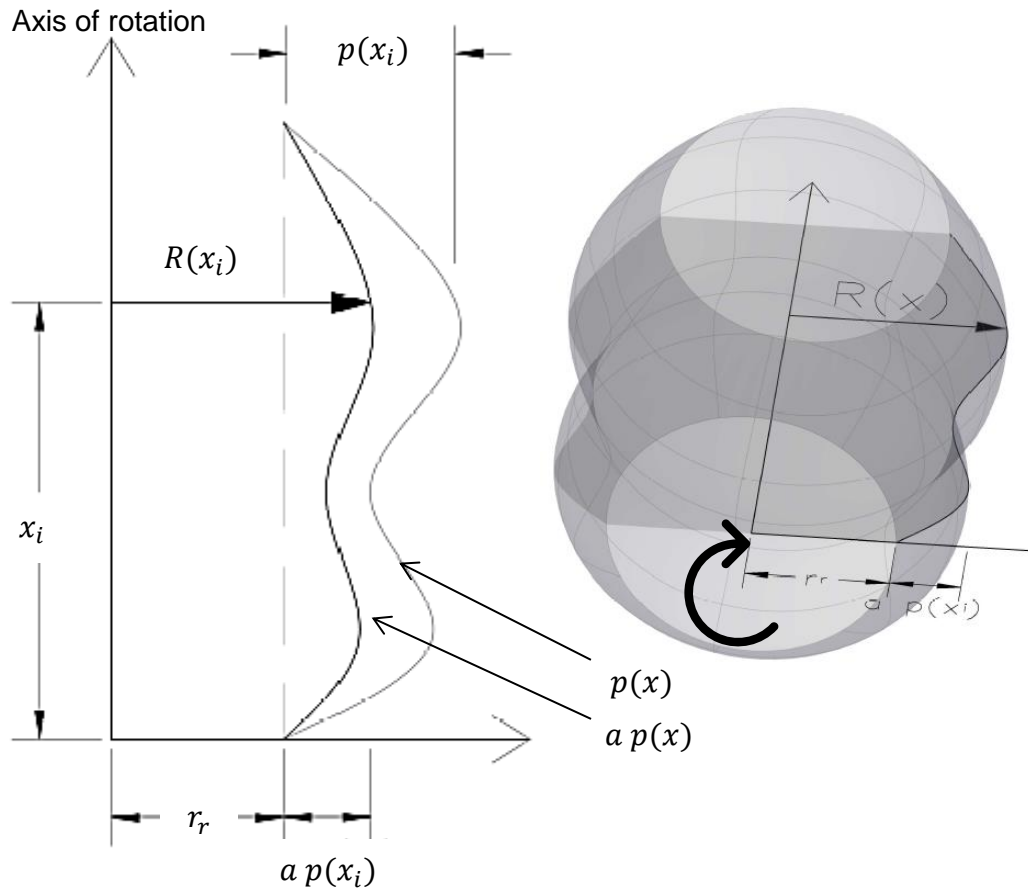


Figure 39. Parametrization of the shape

It is to be mentioned that r_r could have been maimed as a free parameter and the constructability and strength constrains simply used as limit values of the optimizations. However, the evolutionary algorithm implemented in Grasshopper has a limit in the number of input parameters. Due to this limitation, an assumption had to be made.

Another assumption has been made in the shape optimization process. Despite any shape is theoretically achievable with the 3D printing process, from an engineering point of view we still need to utilize shapes that are known. Hence two different shapes have been proposed for the analysis: a sine shape, and a shape retrieved from the literature.

The sine shape (pattern p_1) has been assumed by approximating the shapes obtained from the topology optimization. Again, there are infinite functions that can approximate those shapes, but, according to EC3, the imperfections are modelled applying a sinus shape to the axis of the column, hence in order to have a uniform distribution of bending moments, seems reasonable to assume a sine-shape for the external shape of the column. (See Figure 40 b)

On the other hand, the other pattern has been found in the literature. According to analytical studies on columns under compression, the most optimized shape for a circular hollow strut would be described by the following expression [40]:

$$p(\theta) = \frac{1}{\pi} \left(\theta - \frac{1}{2} \sin 2\theta \right) \quad 0 \leq \theta \leq \pi$$

Where, in order to refer to the coordinates on the axis we need to apply: $x = \frac{\theta}{\pi} \left(\frac{L_0}{2} \right)$

The difference between the two patterns is depicted in Figure 40.

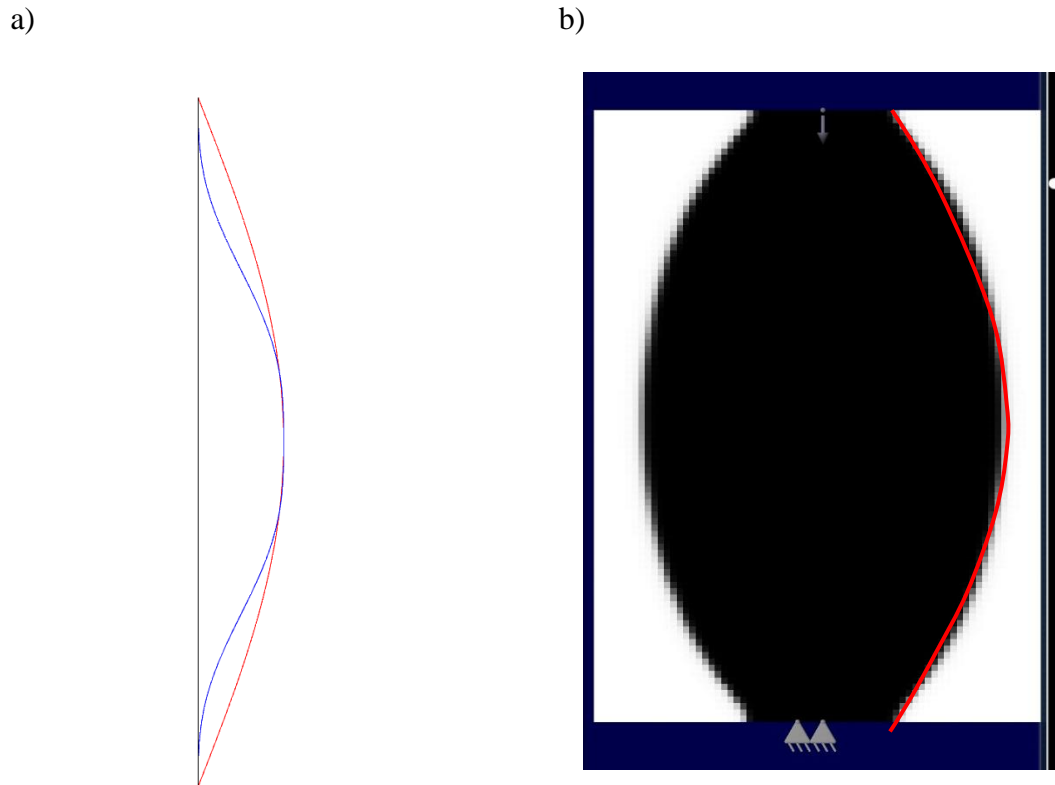


Figure 40. a) Difference between sine-shaped pattern $p_1(x)$ (in red) and $p_2(x)$ (in blue)

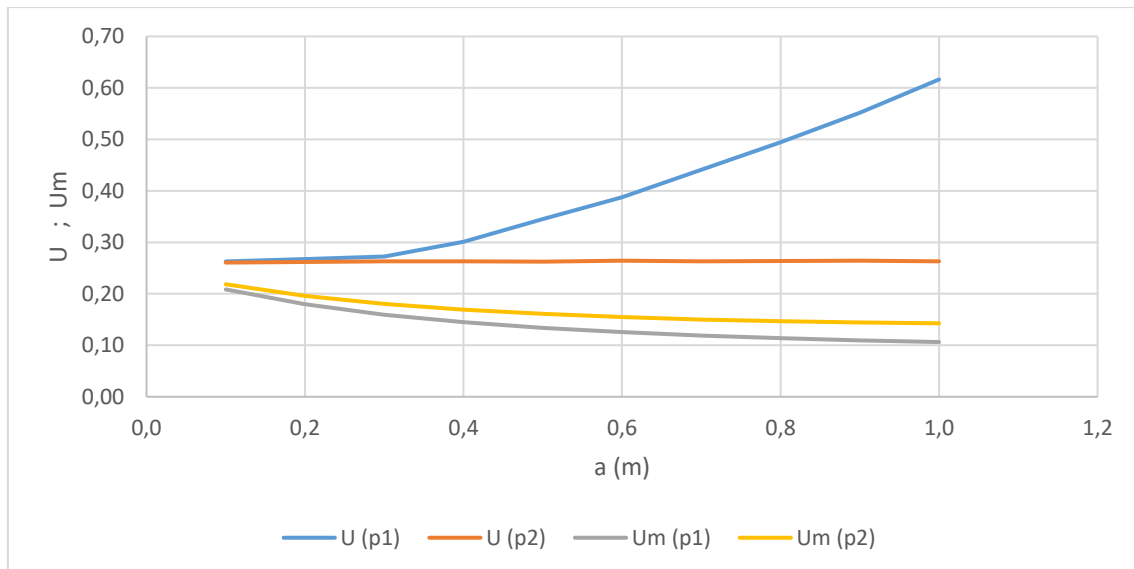
b) Topology optimization with 35% vol. reduction and sine approximation

In order to have a first estimate of the performance of the two patterns a preliminary analysis has been performed in Karamba with shell elements. As we can see from Table 9 and Graph 1, both patterns have pros and cons. On one hand, p_1 have a lower average utilization that means that on average the elements are less loaded, that gives more room for optimization. On the other hand, higher maximum utilizations U have been registered, that means that more peaks of stresses are likely to occur, and failure with it.

The same reasoning, but inverted, is valid for p_2 .

Table 9. Results of investigation on performances of different shapes patterns with shell elements

a	MAX UTILIZATION			AVERAGE UTILIZATION		
	$U(p_1)$	$U(p_2)$	$U(p_1)/U(p_2)$	$U_m(p_1)$	$U_m(p_2)$	$U_m(p_1)/U_m(p_2)$
0.1	0.263	0.261	1.01	0.209	0.219	0.95
0.2	0.267	0.262	1.02	0.180	0.196	0.92
0.3	0.272	0.263	1.04	0.159	0.181	0.88
0.4	0.301	0.263	1.14	0.145	0.169	0.86
0.5	0.345	0.263	1.31	0.134	0.161	0.83
0.6	0.388	0.264	1.47	0.125	0.155	0.81
0.7	0.441	0.263	1.68	0.119	0.150	0.79
0.8	0.495	0.264	1.88	0.114	0.147	0.77
0.9	0.551	0.264	2.09	0.109	0.144	0.76
1	0.616	0.263	2.34	0.106	0.143	0.74



Graph 1. Graphical interpretation of the Utilization for the two patterns

8.4 DEFINITION OF THE GEOMETRY

8.4.1 General Observations

So far, only the outer shape of the strut has been defined. However, in order to reduce the use of material a criterion has to be determined. In this work, a discrete parametric mesh, made of 1D beam elements has been used to investigate the optimization. It has to be underlined that, although the mesh is parametric, the possible combinations of distribution of material are still limited. This limitation could have been avoided by utilizing 3D topology optimization. However, as reported in [4], [5] the computation of the solution and the post processing are very expensive, time consuming and involve the direct intervention of the designer to make the final adjustments.

On contrary, using beam elements allows for direct control on the geometry. The only drawback of such an approach is that we are dealing with 1D elements, lines, to which only in the FEA a cross section is assigned. Hence, particular attention has to be paid to ensure compatibility between the cross section and the actual distance between elements.

8.4.2 Parametrization of the Geometry

As discussed in the previous chapter, a parametric geometry made of 1D elements have been assumed as base geometry for the optimization. The choice of the mesh is justified by the observations on the structural performances of this type of mesh highlighted by [41] in the parametric studies performed on these geometries. Furthermore, this type of mesh is particularly suitable to achieve a large number of possible designs.

The geometry is obtained by the composition of a parametric base module. This module is made of 3 elements: a bottom circle, a top circle, and the inclined element. Figure 41 depicts the procedure to produce the mesh (further details can be found in Appendix II.

1. The two circles are drawn and a segments is generated between two alligned points.
2. The top circle, and the reference point with it, is rotated of a given angle.
3. The same procedure is repeated for the desired number of inclined elements
4. Changing the parameters, like the dimensions and angle of rotation of circles, the number of elements and adding a elements running in the other direction, more complex geometries can be achieved.

The basic modules are then combined to produce the 7m column, so that:

- The number of inclined elements is the same in all modules
- The inclined elements of two adjacent modules converge in the same point in the circles
- The radius of the circles is scaled according to the pattern $p(x)$ identified in Chapter 8.3.

Figure 42 depicts some of the geometries that can be achieved with this process. All of them are possible combinations of the following parameters:

- r_r and a : reference radius and shape amplification factor (alredy introduced in Chapter 8.3)
- n_i : number of inclined elements
- n_h : number of hoops
- θ : total angle of rotation of the hoops per meter in degrees

For ore information on how the mesh is generated refere to Appendix II

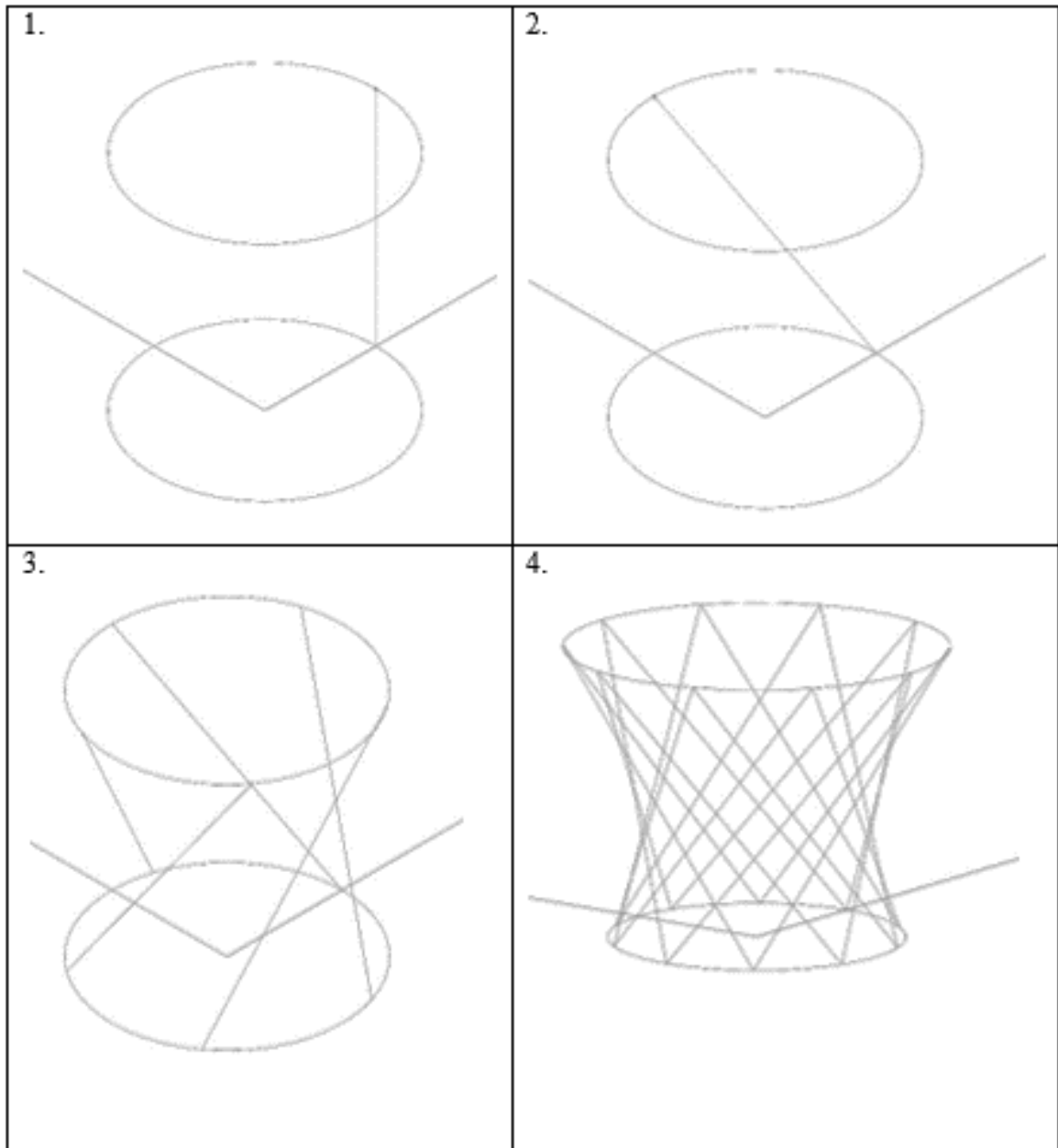


Figure 41. Process used to generate the module of the mesh

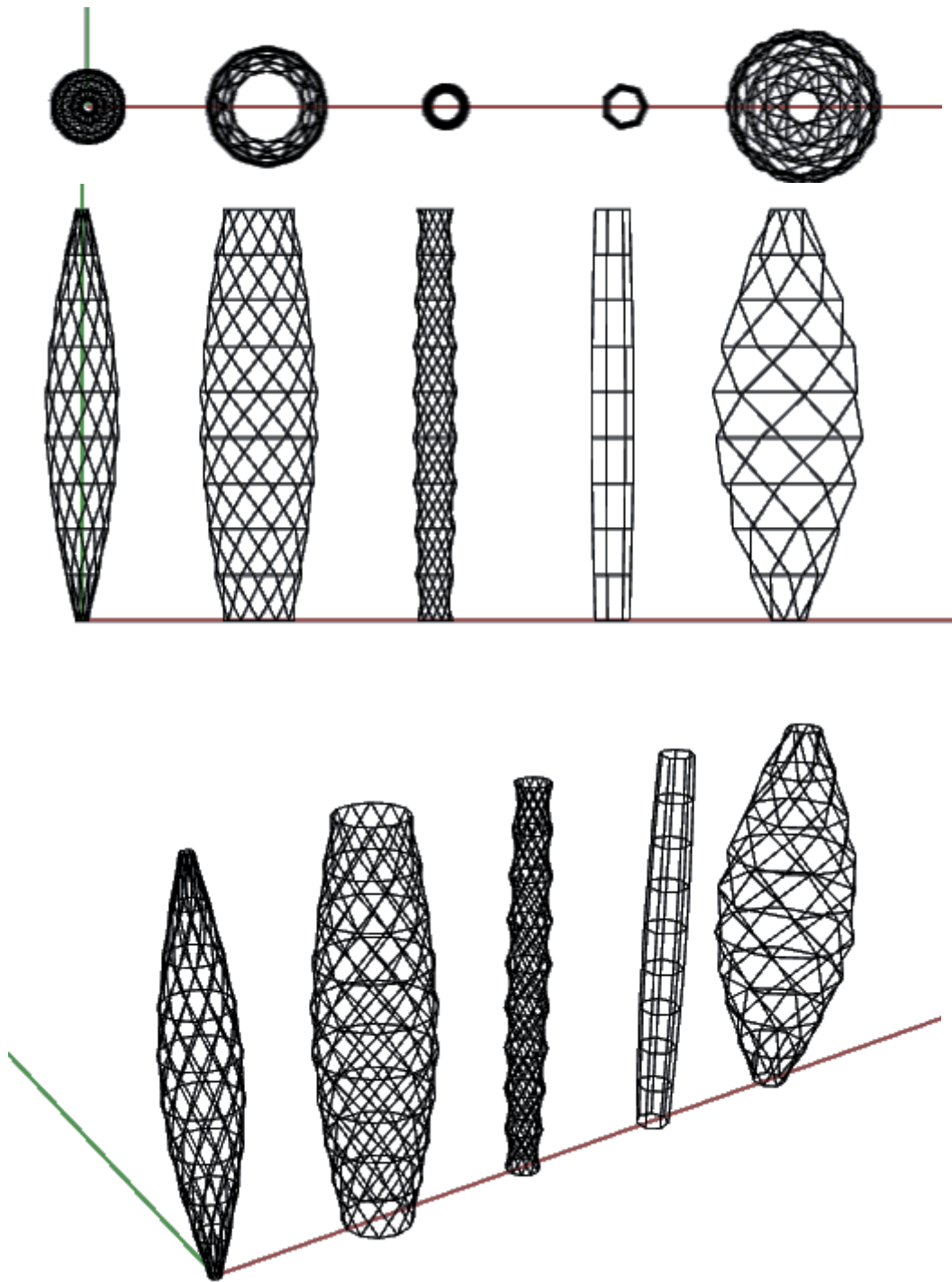


Figure 42. Examples of geometries achievable by varying the parameters for p_1

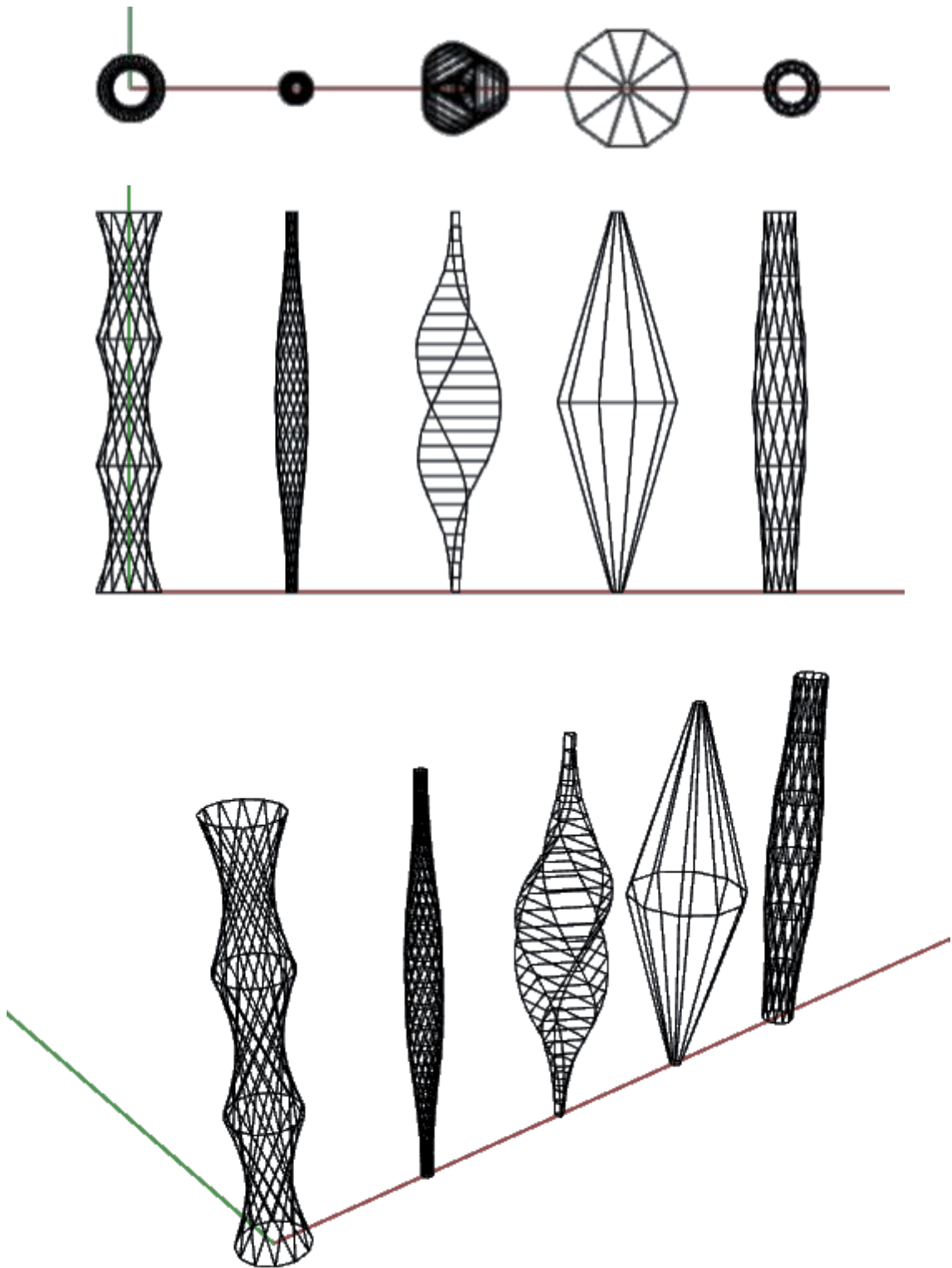


Figure 43. Examples of geometries achievable by varying the parameters for p_2

8.5 OPTIMIZATION ALGORITHM

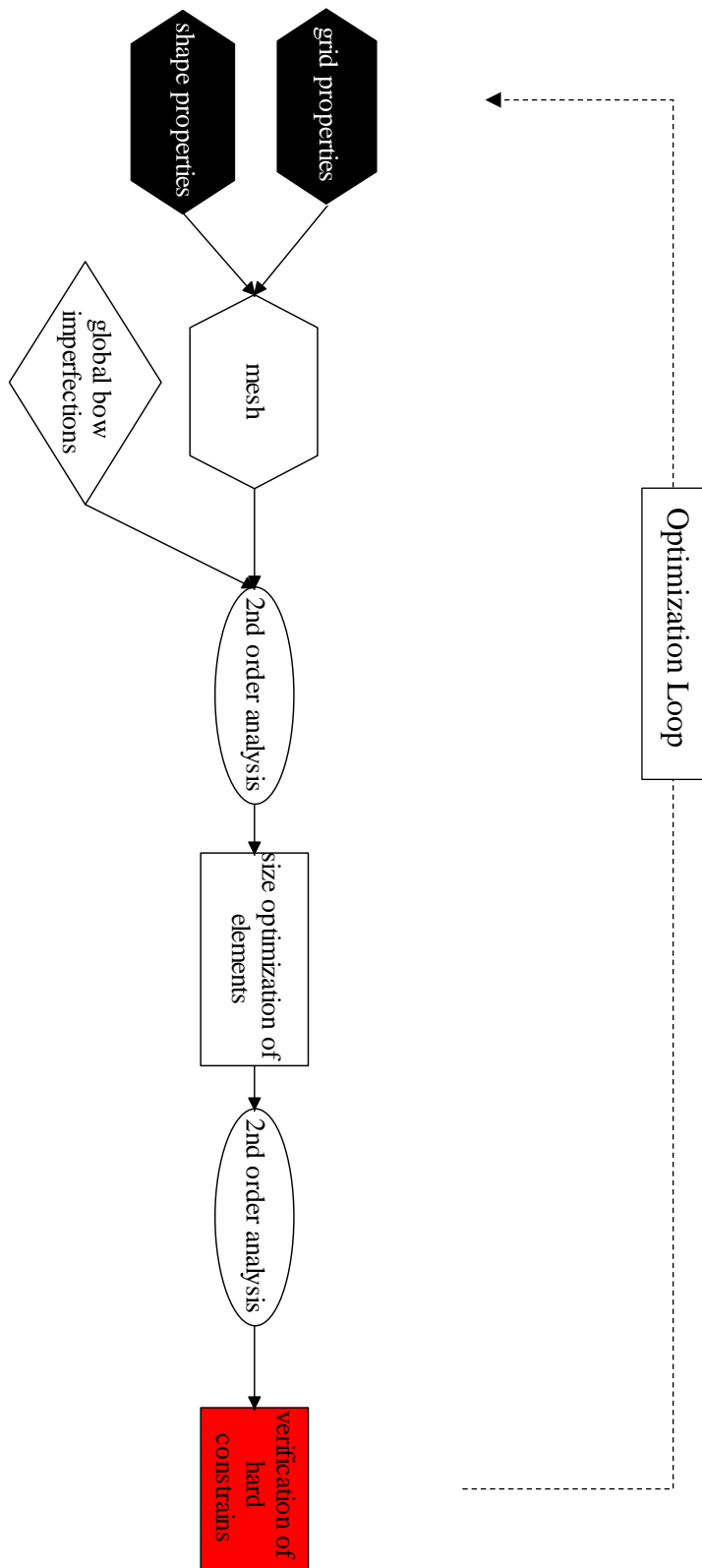


Figure 44. Optimization algorithm

Figure 44 shows the algorithm that has been implemented in Grasshopper. The algorithm takes as input: the parameters described in Chapter 8.4.2, the material properties, the loading and boundary conditions, a generic cross section (the minimum C-S has been used) to perform a second order analysis.

In this very first stage, if the analysis requires to take into account global imperfections, initial global bow imperfections are applied to the axis of the column to reproduce the imperfections analysed in Chapter 7.3.

Once the second order analysis is completed the software automatically performs the size optimization according to the list of C-Ss fed to the algorithm. A final second order analysis is needed to assess the redistribution of the actions due to the changes of the stiffness of the elements. Mass, displacements, forces, buckling load and utilization of elements are then retrieve and used to assess whether the constrains of are respected or not.

These processes are iteratively repeated by the evolutionary solver implemented in Grasshopper to converge to the combination of parameters that minimises the mass.

8.6 SETTINGS FOR THE EVOLUTIONARY SOLVER

Evolutionary solvers, thanks to their versatility and affinity with non-linear problems are particularly suitable for structural optimization of structures.[42]

In order to converge to the geometry that satisfies the constrains and minimises the mass, Galapagos, the evolutionary solver already implemented in Grasshopper, has been used. Due to the elevate computational cost of the analysis the number of individuals per population has been kept quite low (15 individuals), except for first population were a Boost Factor of 3 has been applied in order to have an initial higher range of choice for the following generation. The convergence conditions depended on the goal of the analysis. For intermediate analysis time constrains have been used (generally 1 hour) while the full convergence has been assumed when the fitness value was not changing for the following 5 generations.

8.7 APPLICATION OF CONSTRAINS

In order to limit the feasible domain of the optimization problem, two types of hard constrains have been used: one on the strength of the structure and one on the serviceability.

The strength constrain have been already introduced in the Size Optimization chapter. In order to satisfy the requirements of EC3, a limit on the utilization on all the elements has been set (note that U represents the maximum value of utilization recorded between all the elements):

- $U < 1.0$

The serviceability of the column has been verified by imposing a limit on the maximum horizontal displacement at any node, and on the vertical displacement at the tip.

The assumed limits are:

- $\delta_v = \frac{L}{400} = 18mm$ $\delta_h = \frac{L}{150} = 47mm$

which are slightly less conservative than the $\frac{L}{500}$ and $\frac{L}{200}$ that are typically assumed for steel structures. This reduction is added in order to take into account that the safety coefficients for the loads are generally lower in the SLS than for the ULS. Furthermore, we have to consider that we are still in the preliminary phase of the design hence it is not reasonable to be too strict on the SLS constrains.

8.8 SIZE OPTIMIZATION

Karamba comes to the users with a size optimization component already implemented. Due to time limitations and the possible computational cost added to the algorithm in the eventuality of an algorithm developed by the author (the component would probably result much more optimized and stable) the size optimization has been performed with the component “*Optimize Cross section*” already implemented in software package. According to the manual [43] this component performs checks on axial force, local buckling, lateral torsional buckling, bending, shear and torsion in accordance with EC3 EN 1993-1-1.. However, dealing with straight beams discretized in multiple elements, the buckling length cannot be computationally estimated correctly, hence the software consider as buckling length the minimum distance between two nodes with more than 3 elements converging (unless there is a free end, in that case it is doubled). This result in an inappropriate estimation of the buckling length, but still lies on the safe side for the geometry under analysis, where all the physical connections between the beams are assumed as bending resistant and have at least other 5 elements that converge into the nodes. (except for the initial and final elements but, as discussed in the following chapter, they will be considered as restrained).

According to the manual the “*Optimize Cross Section*” component performs all the verifications cited above iteratively on a list of cross sections assigned as inputs. The algorithm starts with the first cross section of the list and, if it doesn’t satisfy the limits that are set (either utilization or displacements, or both) it moves to the following C-S on the list and so on. Hence, to achieve the maximum performance and reduce the usage of material it is fundamental to calibrate the model correctly. In the calibration process a lot of effort has been put into the definition of the list of cross sections and into the definition of the limits set for the optimization.

The calibration of the latter was particularly complicate because during the iteration process the forces are not updated to take into account the different stiffness of the elements. Hence, ideally an iterative process that alternates size optimization and calculation of forces would be needed. However, these processes are some of the computationally most demanding of the entire model. Hence, the iterative process is not suitable for an optimization. The only other option was to set a lower term for the

estimated final utilization (0.9), so that when the forces of the model with the new stiffnesses are computed, the utilization is still lower than the limit set by the constraints of the optimization (1.0). According to the manual the total optimization is computed as:

$$\frac{N_{Ed}}{N_{Rd}} + \frac{M_{y,Ed}}{M_{y,Rd}} + \frac{M_{z,Ed}}{M_{z,Rd}} \leq 1$$

Where N_{Rd} , $M_{y,Rd}$ and, $M_{z,Rd}$ are the design values taking into account also the reduction due to shear.

As introduced previously another important setting for achieving an optimized column is the definition of a list of cross sections (C-S) correctly organized. This, process can result not too complicated when dealing with traditional C-S but, it is when theoretically any shape is available. Since most of the test performed so far on 3D printed material have been performed circular C-S, hollow and solid circular C-S have been used.

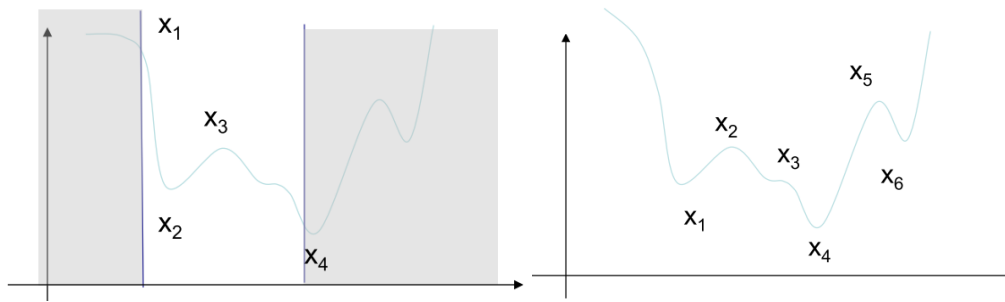


Figure 45. Constrained vs unconstrained domain

From an optimization point of view, the more freedom is left to the system the most optimized the final product would be (convergence to absolute maxima). However, some boundaries have to be introduced in order to ensure that the result was physically compatible. An example is the cross section of the elements at the base, where the stresses are concentrated and bigger C-Ss are needed, but the available space is limited. In order to take this into account, initially a limit was set to the number of inclined elements according to the maximum cross section in the list in order to ensure that no superposition occurs between different elements. However, this resulted too limiting for the optimization process, thus the constrain was later on deleted and assumed as part of the post-processing.

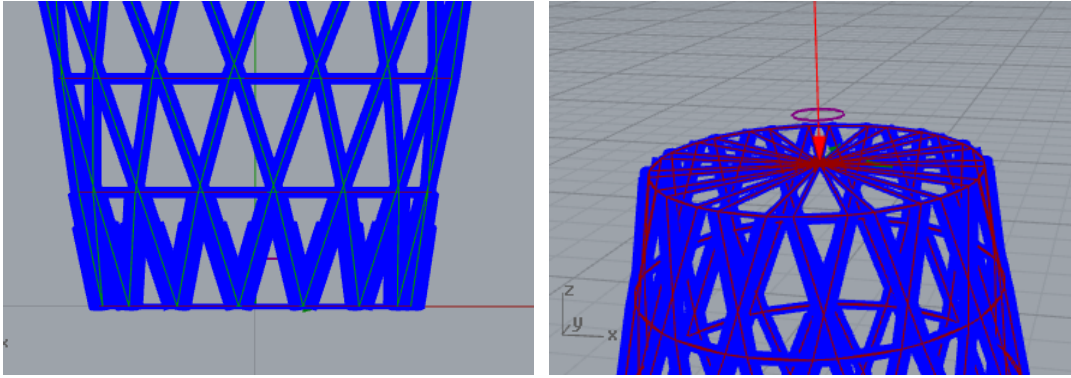


Figure 46. Detail of the collision between C-S at the base of the column and modelling of point of application of loads and boundary conditions at the top.

In fact, once the final design is known, it is possible to intervene directly on the elements and assess if they are compatible or if the compatibility can be achieved by manually changing the cross section. A final countermeasure could also be substituting part of the grid mesh with a solid hollow cross section, in order to exploit the shell behaviour and stat the grid mesh as soon as the stresses are more suitable for beam elements. This solution is particularly interesting as it is also compatible with the traditional ways of performing the connections with hollow C-S, but of course would also ensure sufficient strength to an equivalent 3D printed connection.



Figure 47. Traditional pinned connection for a hollow cross section. [44]

Nevertheless, this is still not achievable in Karamba where the choice of elements is limited to only two types (beams or shell). For such an analysis more complex FEM software packages are needed. In addition, such a complex analysis would probably require an elevate computational cost itself, making it not appropriate for an optimization problem.

Therefore, for this early design stage, the assumption of compatibility has been removed, and only visual checks on the final mesh have been performed. Nevertheless, a limitation in the dimension of the C-S has been set. 100mm have been assumed as the limiting threshold both for architectural appearance and compatibility. On the other hand quite some freedom has been left for the internal wall thickness. In accordance with the printing process settings at RamLAB and MX3D, the average bead size is 5mm. Hence, assuming that the cross sections are created as concentric circles with radii that are multiples of the bead size the minimum C-S is 10mm and the maximum is 100mm. The same reasoning has been applied for the determination of the possible wall thicknesses. The wall thickness varies from one width bead, 5mm, up to a solid cross section, with steps of 5mm. With this solution, not only the singular cross sections are certainly printable, but also the transition between one cross section to the other can be more easily performed.

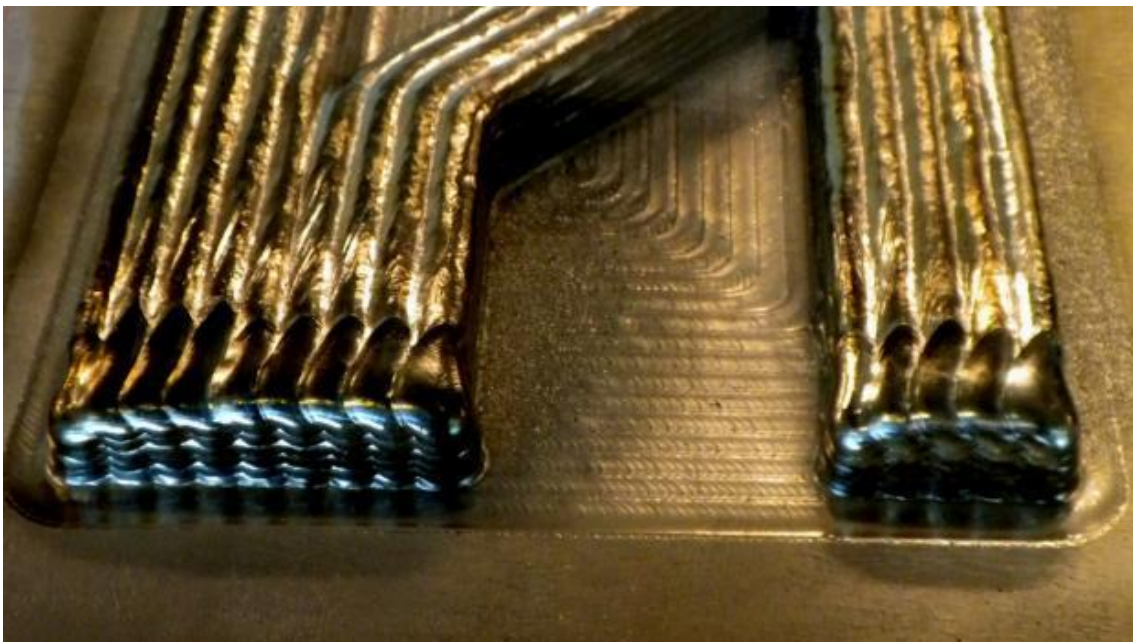


Figure 48. Detail of the bead thickness [45]

8.9 BOUNDARY CONDITIONS

Since we are dealing with a three-dimensional mesh, it was not possible to simply restrain the degrees of freedom according to the structural model identified in Chapter 6.3. For this reason, additional stiff elements, representing stiff steel plates, have been added to the end points of the mesh. The central points of these element have finally been used to assign load and restrains, and to ensure a realistic redistribution of the actions. (see Figure 46).

Furthermore, in addition to the actual load, the self-weight of the structure has been added to the loading conditions. This is not due to the relevance of the load itself but it is important to trigger buckling in a given direction and hence allow to assign correctly the direction of the initial imperfections.

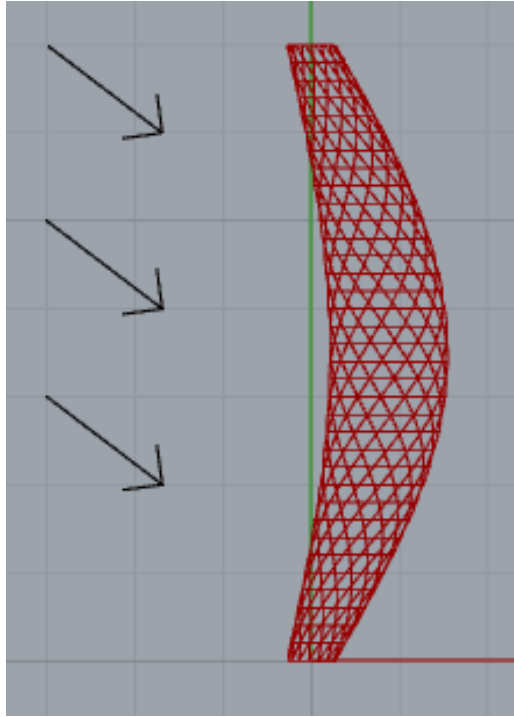


Figure 49. Direction of g force and initial global bow imperfection 20 times scaled.

9 ANALYSIS OF CONVERGENCE

Since there is no direct control on the convergence of the analysis, some post-analyses have been performed. The results showed that some geometries were included in the feasible domain only because the random numbers generated by the non-convergence of the analysis were satisfying the constrains.

In order to verify how to detect when these random solutions are erroneously included in the feasible domain, 10 geometries have been tested. The values of the most relevant output of the analysis (see Figure 50) have been recorded as a function of the compressive load P . Here follows the analysis of the results, further details on geometries and general results can be found in Appendix III.

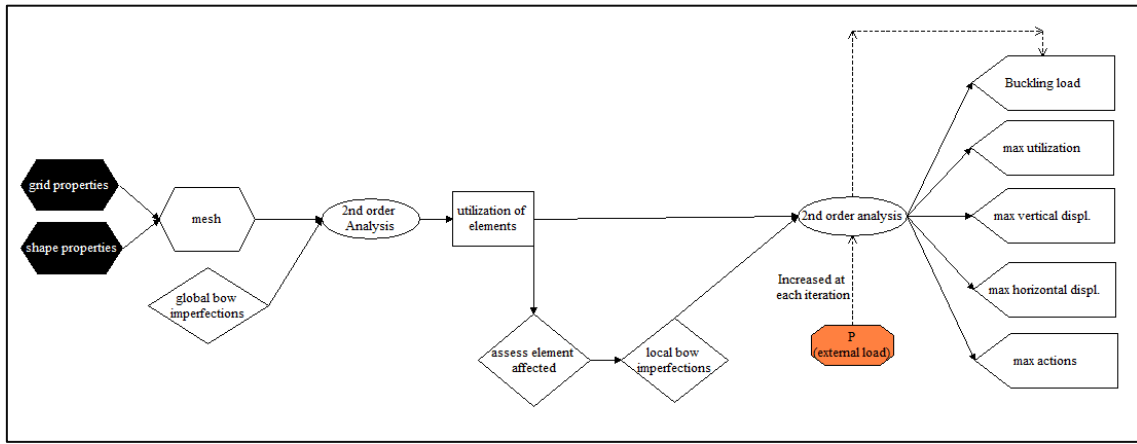


Figure 50. Algorithm for the definition of outputs as a function of applied load P

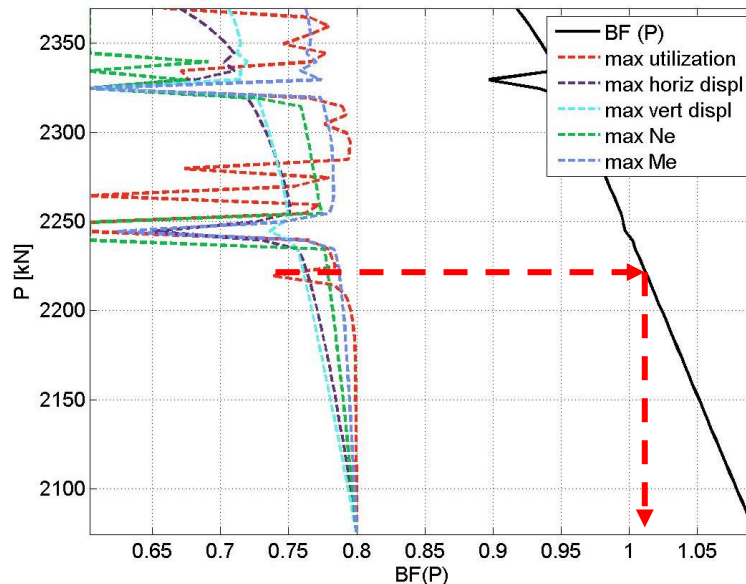


Figure 51. Plot for the analysis of convergence for geometry2

Figure 51 reports the graph that has been used to assess the stability of the solution. The black continuous line represents the plot of the “Buckling load factor” (BF), output of the

component “*Buckling Mode*” implemented in Karamba, as a function of load P . The dashed lines instead represent the trend of the other outputs (horizontally rescaled for the comparison).

Despite this component is not meant to analyse imperfect geometries, such as those that we are under investigation, a correlation between the stability of the analysis and this BF has been found. As we can see when $BF \approx 1$ peaks occur.

These peaks are clearly a computational spurious behaviour as it is physically impossible that increasing the vertical load on an imperfect column values like the vertical and horizontal displacement reach a certain value and then start to decrease again.

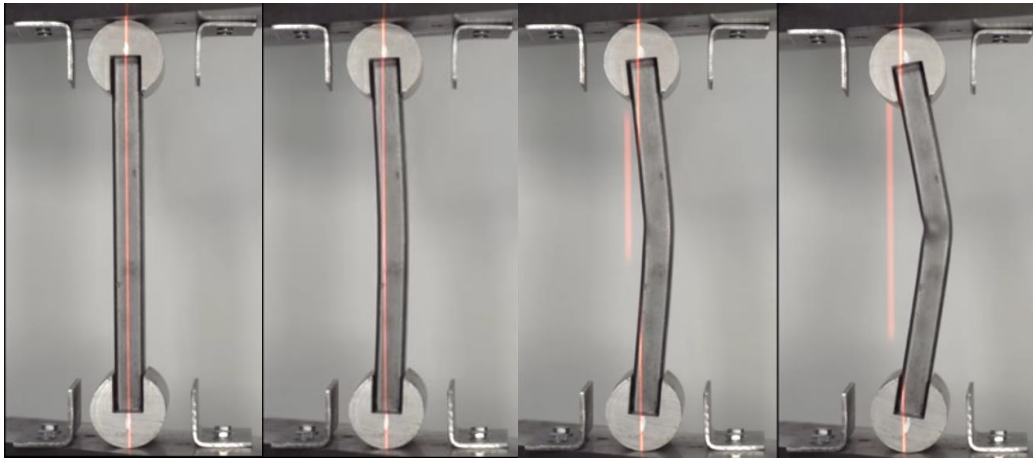


Figure 52. Time lapse of failure of imperfect column [46]

The same behaviour was found for the other geometries. For values of $1.0 < BF < 1.1$, spurious peaks in the outputs occurred. Hence, despite no final conclusions can be drawn, it is clear that whenever BF is smaller than 1.1 (that is the maximum value of BF for which peaks have been identified), the solution needs to be verified with the procedure here presented.

It has to be underlined that theoretically it would have been possible to include this check directly in the algorithm, however this would have almost doubled the time required to find a solution. Thus, it resulted more efficient to apply the following procedure:

1. Save the solution at the end of every optimization loop
2. Once the optimization process is completed, verify the convergence with the procedure here highlighted
3. Exclude the spurious solutions
4. Retrieve the “best non-spurious” solution from the saved ones.

10 SUMMARY OF SETTINGS FOR OPTIMIZATION PROCESS

10.1 SETTINGS FOR FINITE ELEMENT ANALYSIS

10.1.1 Material

$$E=100\text{Gpa}$$

$$\nu = 0.3$$

$$G = \frac{1}{2(1+\nu)} = 38.5 \text{ MPa}$$

$$f_y = 350 \text{ MPa}$$

10.1.2 Geometry

$$L_0 = 6996 \text{ mm}$$

$$\text{Reference radius: } r_r = 100 \text{ mm}$$

$$\text{Shape amplification: } 0 \leq a \leq 1$$

$$\text{Number of inclined elements: } 1 \leq n_i \leq 15$$

$$\text{Number of hoops: } 1 \leq n_h \leq 35$$

$$\text{Total angle of rotation of the hoops per meter: } 0^\circ \leq \theta \leq 100^\circ$$

10.1.3 Analysis

Due to limitations in the capabilities of the software, only non-linear geometry is considered. The material is considered linear elastic and the boundary conditions are independent from the load.

10.1.4 Boundary Conditions

Since the column is inclined and an axial symmetric geometry is used it is reasonable to assume that the column buckles in the direction of the gravity force (assumed as acting on plane xz) where the self-weight triggers the buckling of the column. Hence:

Table 10 Boundary condition for redesigned geometry

DOF	NODE 1	NODE 2
TX	Fix	fix
TY	Fix	fix
TZ	Fix	free
RX	Fix	fix
RY	Free	free
RZ	Fix	fix

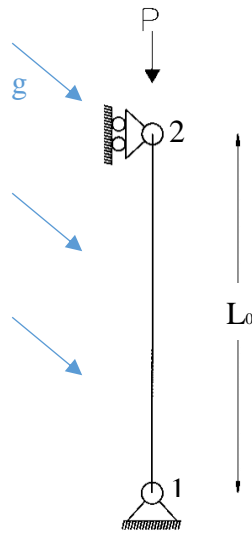


Figure 53. Structural model along plane xz

The design load instead is the buckling load of OC: $P_0 = 1957 \text{ kN}$

10.2 SETTINGS FOR OPTIMIZATION ALGORITHM

10.2.1 Imperfections

Since no models are available for the design of free form 3D printed steel columns the imperfections have been assigned in accordance with EC3. A sine shape has been assigned to the axis of the column with $e_0 = \frac{L}{157} = 44.5 \text{ mm}$

10.2.2 Optimization goal and Constrains

The goal of the optimization process is the identification of the column capable of withstanding the load $P_0 = 1957 \text{ kN}$ (strength constrain: $U < 1$) with reasonable deformation (serviceability constrains: $\delta_v = \frac{L}{400} = 18 \text{ mm}$ $\delta_h = \frac{L}{150} = 47 \text{ mm}$) and minimum mass.

10.2.3 Convergence

The evolutionary loop is stopped whenever the best solution is not updated in the following 5 generations.

In order to ensure that the solution is not spurious a verification has to be performed by applying the method described in Chapter 9.

ANALYSIS OF RESULTS

11 DEFINITION OF THE OPTIMUM SOLUTION FOR p_1

11.1 SOLUTION OF OPTIMIZATION WITHOUT IMPERFECTIONS

11.1.1 Optimization and Analysis in Karamba

As a first step, the optimization process has been performed on a geometry without initial imperfections (NI). Table 10 and Figure 54 depict the geometrical properties of the geometry found through the optimization process.

Table 11. Parametric description of the optimized solution

<i>Imp.</i>	<i>m (kg)</i>	<i>a</i>	<i>n_i</i>	<i>n_h</i>	<i>θ</i>
NI	557	0.11	4	22	71



Figure 54. Optimized geometry

According to the results of the non-linear analysis performed with Karamba, this structure has a maximum utilization of the elements $U = 0.95$, while the vertical and horizontal displacements stood at 17.20 and 4.16 mm respectively. As we can see these results respect the boundaries imposed as hard constrains for the optimization process.

11.1.2 Verification of the structural performance

In order to assess the reliability of Karamba the results obtained from the optimization process have been compared with those obtained from an analysis with a more reliable FEM software: Oasys GSA. The geometry obtained in Rhino has been exported with a plugin called Geometry Gym [47] (available for free for academic use) and imported directly in GSA. Geometric and material² non-linearities have been taken into account for the analyses in GSA.

According to the results the maximum vertical and horizontal maximum displacements are 17.35 and 14.65 mm respectively. As we can see, the vertical displacement is almost unaltered while the horizontal displacements are significantly different with respect to the one identified in Karamba.

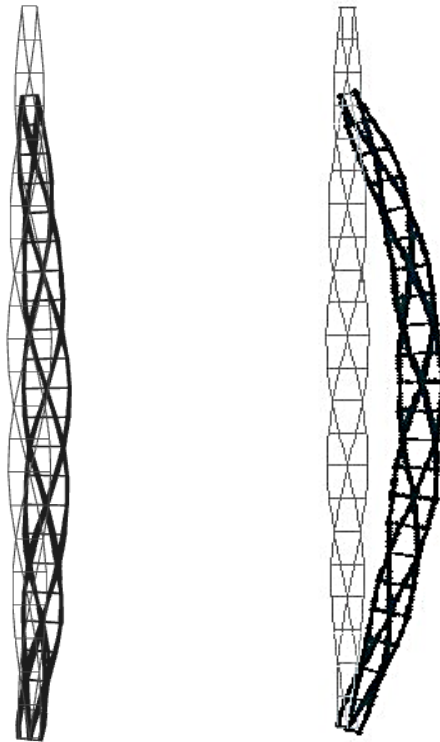


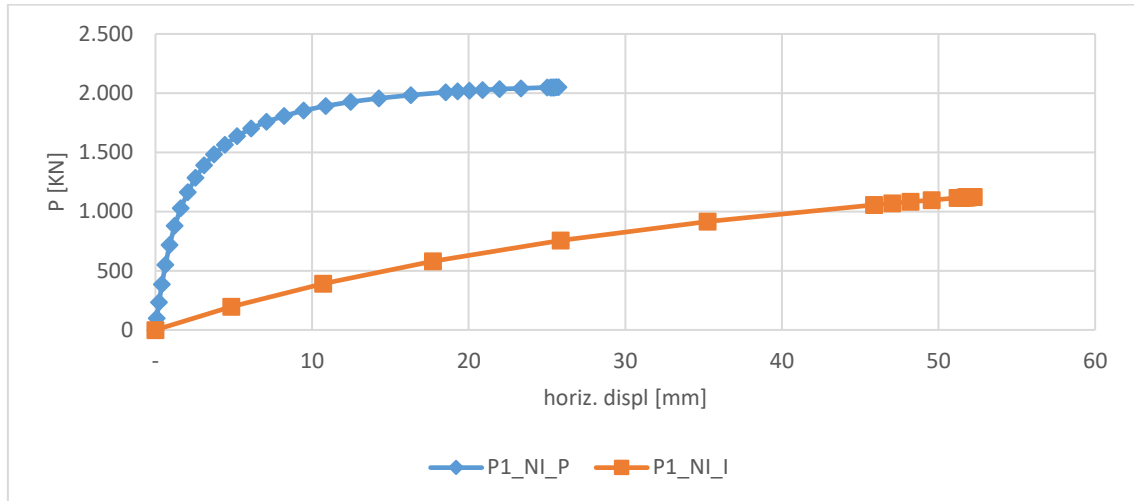
Figure 55. 50-times scaled deformed configurations in Karamba (left) and GSA (right)

² GSA is only capable to model Elasto-plastic material

11.1.3 Assessment of robustness

The same geometry has been tested after the application of imperfections ($e_0 = \frac{L}{157} = 44\text{mm}$) on the axis. (id: P1_NI_I)

An incremental analysis has been performed in GSA to assess the ultimate load of the imperfect column.



Graph 2. Load factor VS horizontal displacement of node 108 for perfect and imperfect shape



Figure 56. Location of the node where displacement is traced (node 108)

As we can see the maximum achievable load is about 60% of the applied load $P_0 = 1957\text{ kN}$. Therefore, we can conclude that, despite the perfect structure is capable to withstand the design load ($P_{cr}=2050\text{ kN}$), as soon as imperfections are considered, the structural system is not stable and hence cannot be considered sufficiently robust.

11.2 OPTIMIZATION WITH IMPERFECTIONS

11.2.1 Optimization and Analysis in Karamba

The Optimization algorithm has been applied to an initial geometry with global axial imperfections (GI) already included in the initial geometry (id: P1_GI_I). The algorithm converged to a solution with the geometrical properties reported in Table 12 and Figure 57.

Table 12. Parametric description of the Optimized geometry

<i>Imp.</i>	<i>m (kg)</i>	<i>a</i>	<i>n_i</i>	<i>n_h</i>	<i>θ</i>
GI	584	0.13	9	35	55

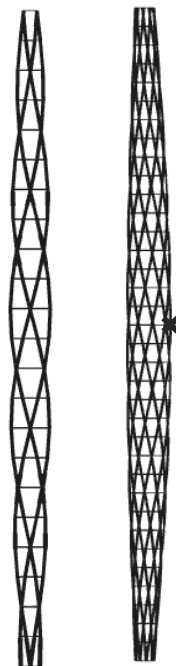


Figure 57. NI (left) vs GI(right) optimized geometry with reference node

As we can see the structure is significantly different from the one identified previously. The optimization process converged to a solution characterized by higher values of each parameter, making the mesh much denser.

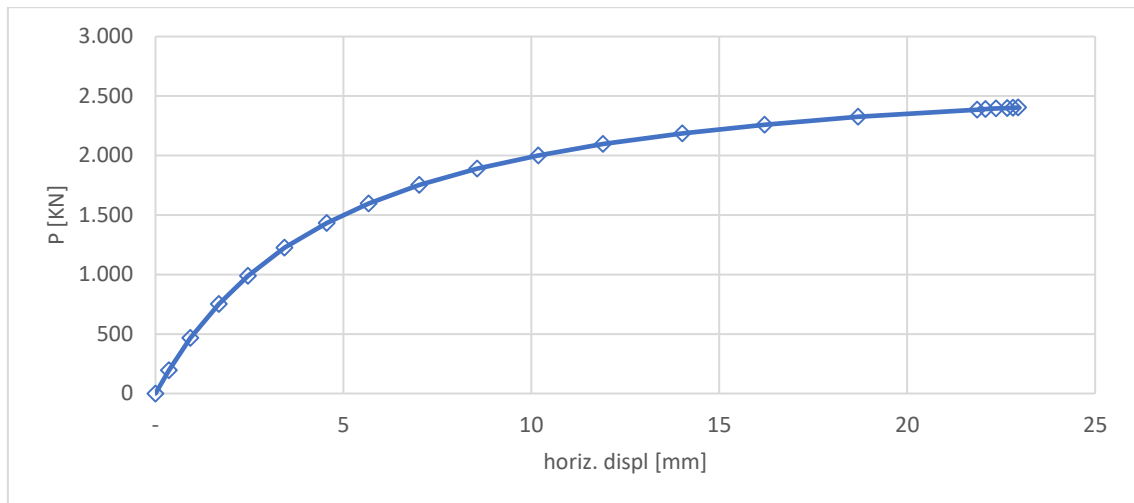
11.2.2 Verification of geometry optimized with imperfections

Despite not completely correct from an engineering point of view (the structure is not axial-symmetric, also in the C-S), the structure with initial imperfections identified with Karamba have been checked in GSA (id: P1_GI_I).

	KARAMBA	GSA
IMP.	GI	GI
$\delta_v(mm)$	16.53	16.54
$\delta_h(mm)$	17.69	17.78

As we can see in this case the two Software packages converged to almost the same solution. Furthermore, the structure results verified under the design load.

In order to investigate the ultimate load of this configuration, an incremental analysis has been performed in GSA.



Graph 3. Results of incremental analysis for geometry optimized with global imperfections

As we can see this structure is capable to withstand the design load with a safety margin equal to $1 - \frac{P_{ult}}{P_0} = 1 - \frac{2426 \text{ kN}}{1957 \text{ kN}} = 0.24 = 24\%$

11.3 SOLUTION FOR RANDOM IMPERFECTIONS

Despite an optimized solution has been found an observation is necessary. It is not reasonable to assess the robustness of the imperfect structure under the same conditions for which the structure has been designed for due to the randomness of imperfections.

Hence, in order to take into account the randomness of imperfections, only the parametric description of the mesh has been used while the definition of the cross sections has been performed on a straight column, so that the structure results symmetric.

11.3.1 Verification of structural performances and robustness verification for modified GI

The same parametric description of the geometry obtained from the optimization process with GI has been used as input for a size optimization. Hence this structure is characterized by a totally equal mesh but different C-S with respect to P1_GI_I

The structure with and without imperfections (id: P1_GI_P_M and P1_GI_I_M) has been tested in GSA.

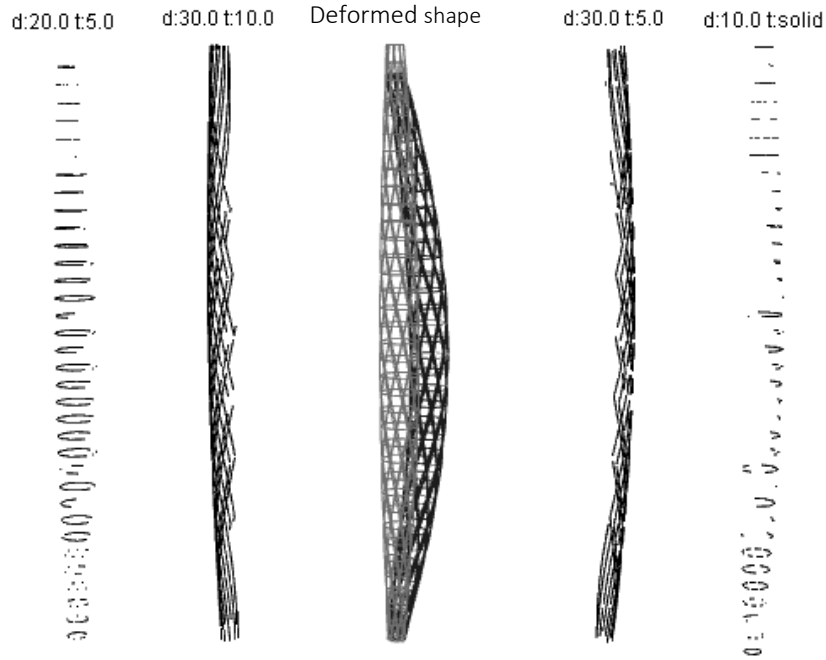
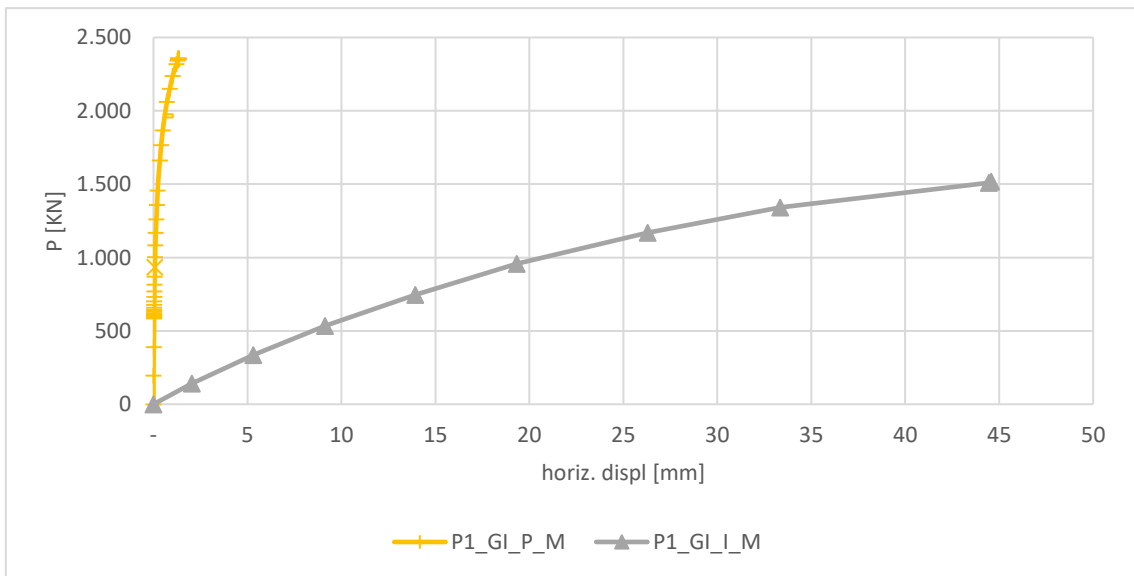


Figure 58. Exploded view of distribution of C-S, inclined elements and hoops for geometry optimized with initial imperfections (P1_GI_I)



Graph 4. Results of incremental analysis on geometry modified, optimized with initial global imperfections

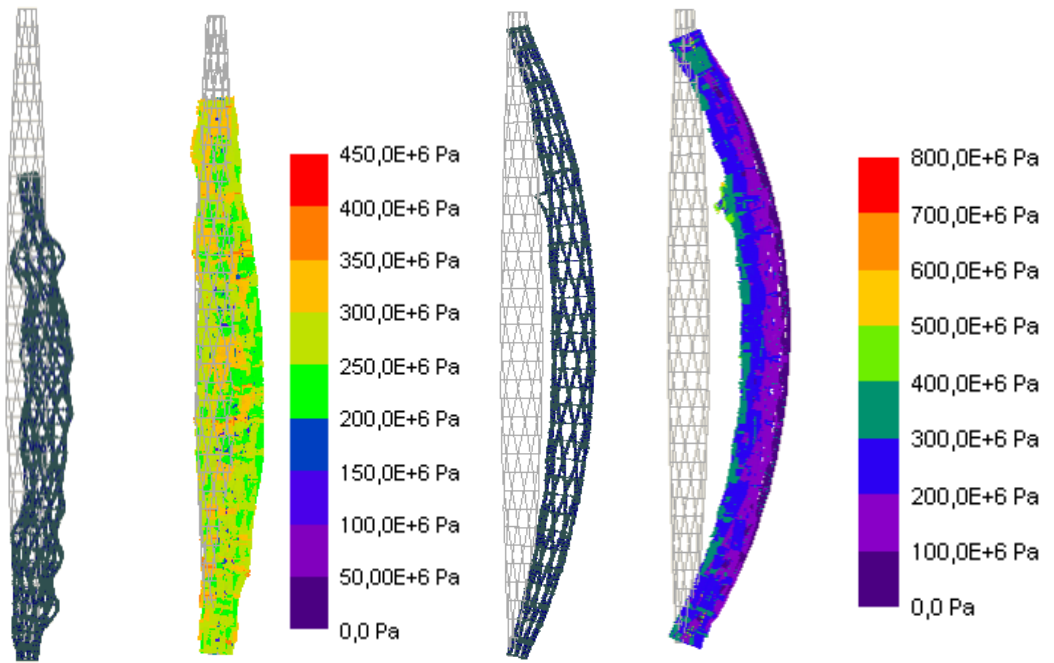
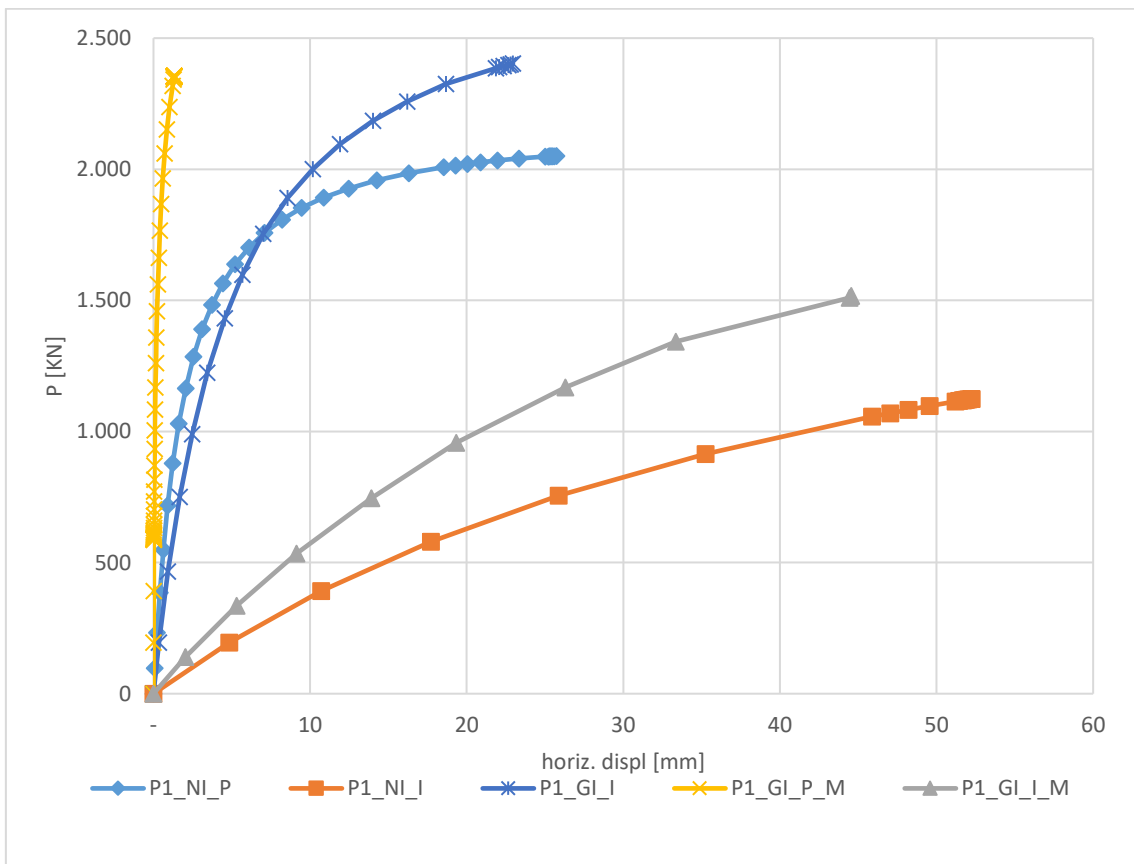


Figure 59. Failure mode and corresponding stresses for P1_GI_P_M (left, scale 1:100) and P1_GI_P_M (right, scale 1:10)

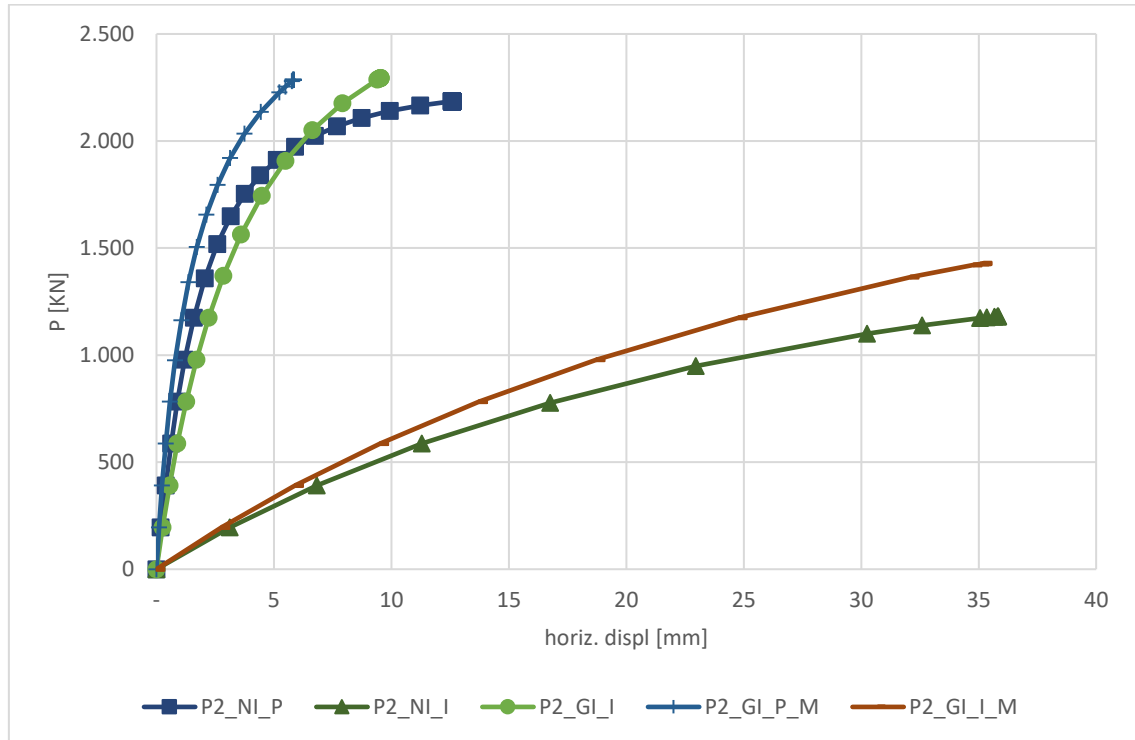


Graph 5. Summary of results of incremental analyses for p1

12 DEFINITION OF THE OPTIMUM SOLUTION FOR p_2

The same procedure described above have been applied also for geometries with external shape defined by p_2 .

All the results have been summarized in Graph 6.



Graph 6. Summary of results for pattern 2.

As we can see, again the structures without imperfections are much stiffer and have higher ultimate load. Between the imperfect geometries, only the geometry with both mesh and C-S optimized for global imperfections (P2_GI_I) is sufficiently strong to withstand the design load.

Figure 60 depicts the failure mode of the columns for the different configurations. As shown, the central “bulb” is not significantly affected by deformations, while the bearings are highly deformed, and as we know, the higher the deformations, the higher the stresses. This hypothesis is confirmed by the analysis of the stress distribution reported in Figure 61. From the picture we can clearly see that both the area of the bulb in compression and the area next to the supports are particularly stressed.

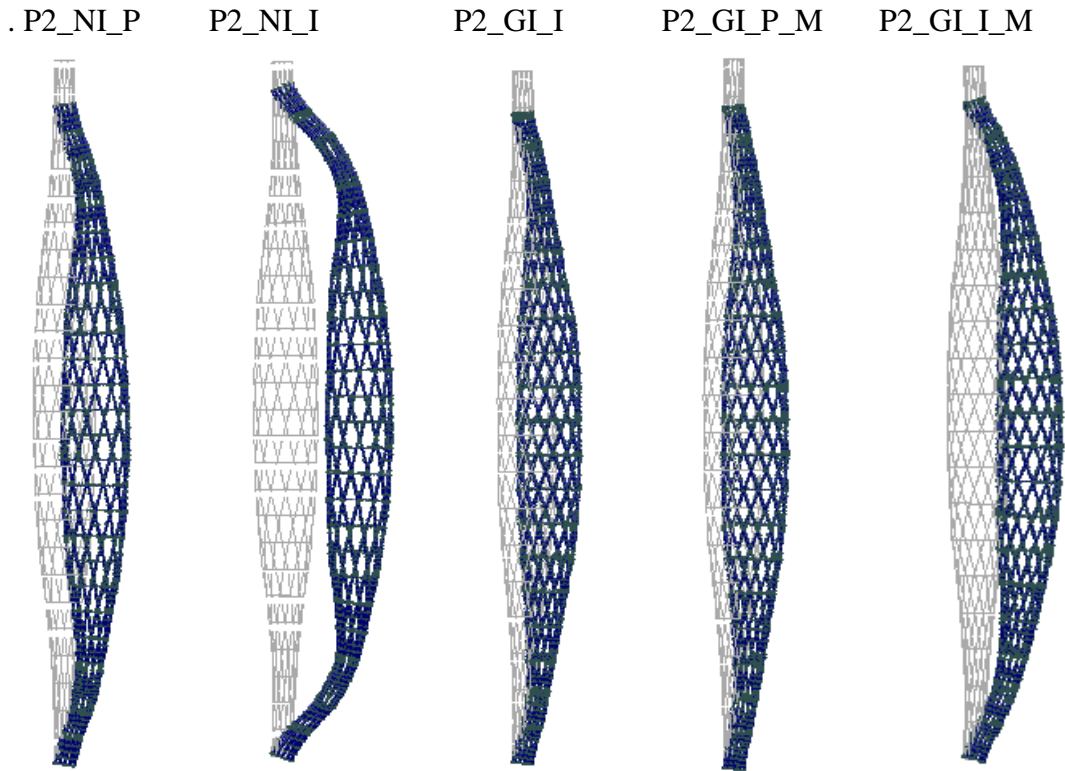


Figure 60. 1:25 deformed shapes at failure

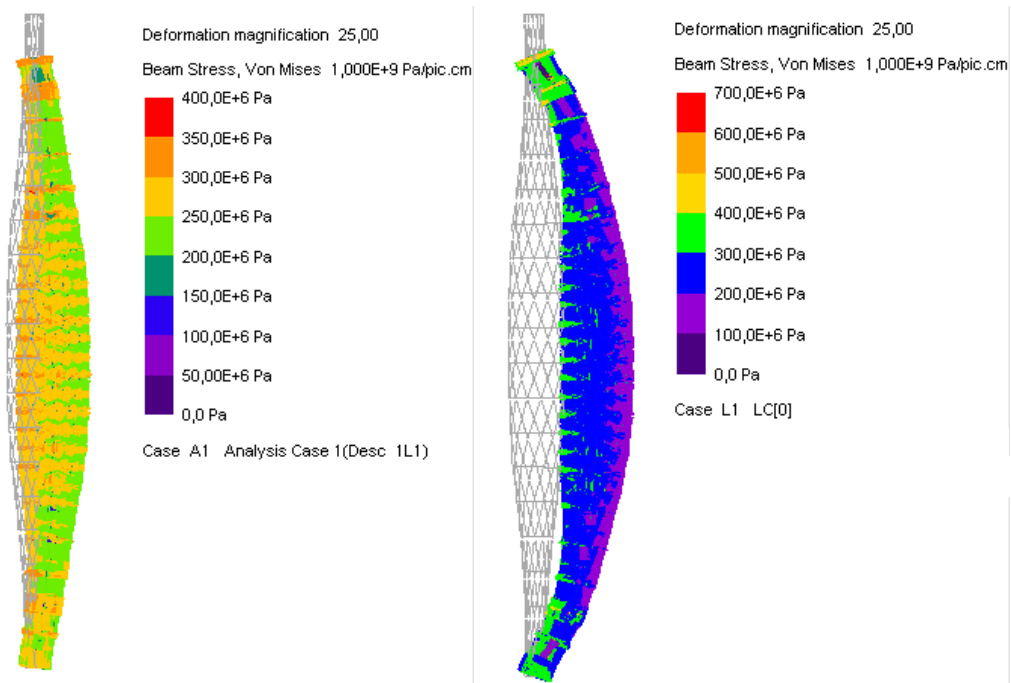
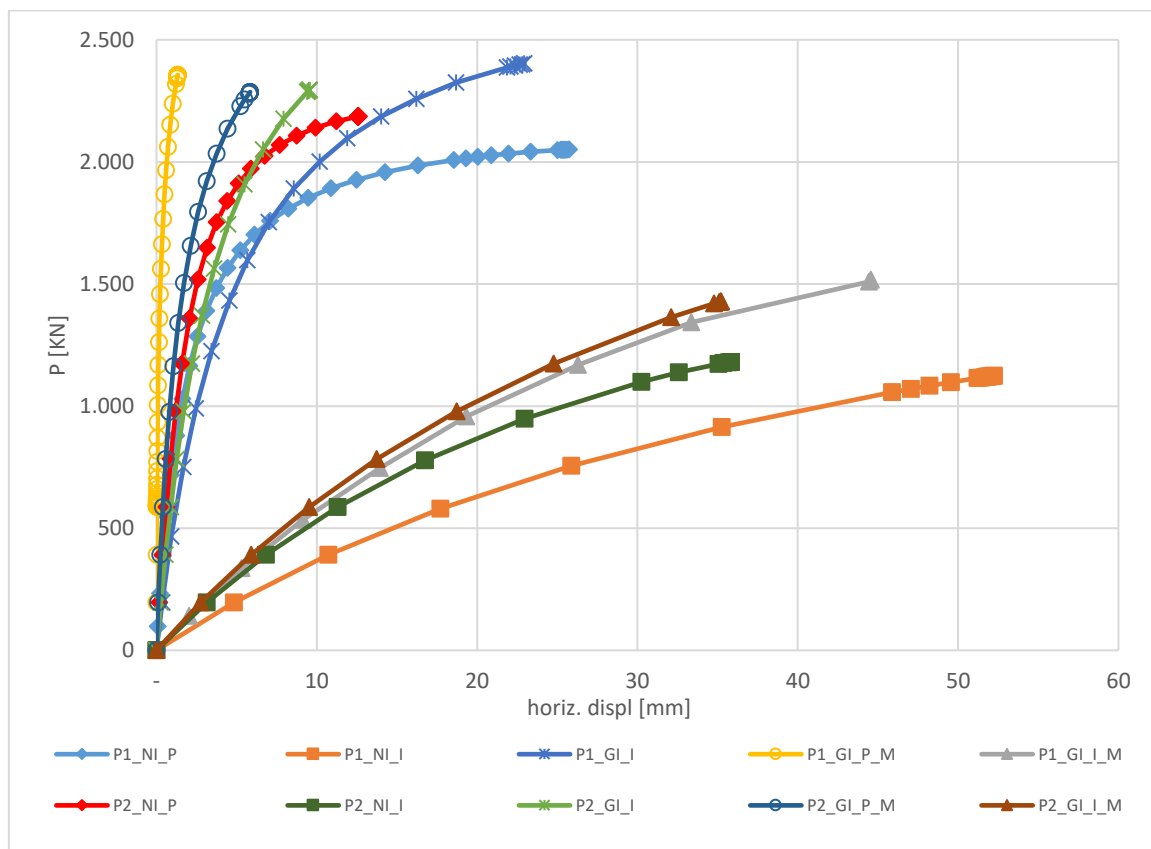


Figure 61. Analysis of stress distribution at failure for P2_NI_P and P2_NI_I

13 COMPARISON OF RESULTS

All the results of the non-linear analyses performed on the different models have been summarized in Graph 7 and Table 13.



Graph 7. Summary of incremental analyses of all model tested

Table 13. Summary of strength performances of different solutions (highlighted in red those that fail under the design load)

imp. opt. ³	P1						P2				
	NI		GI		GI_M		NI		GI		GI_M
m (kg)	557		584		607		560		685		609
imp	P	I	I	P	I	P	I	I	P	I	
P_{cr}⁴ (kN)	2192	-	-	3072	-	2388	-	-	2955	-	
P_{ult} (kN)	2050	1124	2426	2387	1507	2309	1037	2293	2286	1428	
P_{ult}/m (kN/kg)	3.68	2.02	4.15	3.93	2.48	4.12	1.63	3.35	3.75	2.34	
LF⁵ = P_{ult}/P₀	1.05	0.57	1.24	1.22	0.77	1.18	0.53	1.17	1.17	0.73	

³ Imperfections used in the optimization process and eventual modifications

⁴ Computed via modal analysis in GSA

⁵ Load Factor

13.1 ASSESSMENT OF THE OPTIMIZATION LEVEL

Since it is the main goal of this thesis, it is now time to assess whether these structures are actually optimized. Despite the structures resulting highly optimized in Karamba, the limitations of the software to perform accurate analysis led to discrepancies between the performances used in the optimization and the “real performances” assumed to be the one provided by GSA. It is to be said that this inaccuracy is due to the type of analysis implemented in Karamba, where only geometric non-linearities can be taken into account. However, probably this type of analysis has been preferred as material non-linearities increase dramatically the time for the analysis. Consider that, for these types of geometries, the analysis in Karamba takes about 5-10 seconds, against the 6-12 hours for the one in GSA. Taking this into consideration, the speed of Karamba is fundamental when dealing with optimization problems, where thousands of models have to be analysed.

On the other hand, it is to be said that all the structures sized in Grasshopper via Karamba resulted verified in the conditions for which they have been designed for. Only when imperfections are added to structures designed for a perfect system (all those not in red in the table), they did not result verified.

On the other hand all the structures tested in the conditions for which they have been designed performed with about a 20% margin (LF-1), except for geometry P1_NI_P that have only 5%, with respect to the minimum strength. Hence, we can conclude that the structures are still not fully optimized.

As already mentioned, the reason for this margin is probably due to the difference in the type of analysis performed, but also due to the constraint used for the optimization problem (constraint on U), that do not relate directly to the stresses.

13.2 ASSESSMENT OF STRENGTH AND EFFICIENCY

13.2.1 Comparison between geometries

As discussed in the previous chapter, the geometries resulted not completely optimized from the point of view of the load carried. However, it is interesting to verify whether these geometries are at least efficient.

Looking at the ratio between the critical load P_{ult} and the design load P_0 it can be clearly seen that most of the design are not strong enough to withstand the load (highlighted in red). As expected these are all geometries with imperfections applied on the axis. The only imperfect geometries that are capable to resist the load are those that have been sized with imperfections already applied (GI_I). These geometries not only are able to resist the actions with the imperfections, but have ultimate load that is equivalent or higher than perfect structures. However, this is not completely for free as in order to achieve these performances higher quantities of material are needed.

Despite this, when looking at the ratio between P_{ult}/m , that is a factor that express the efficiency of the usage of material, the load carried per unit of mass, we can clearly see that these structures also have the highest efficiencies.

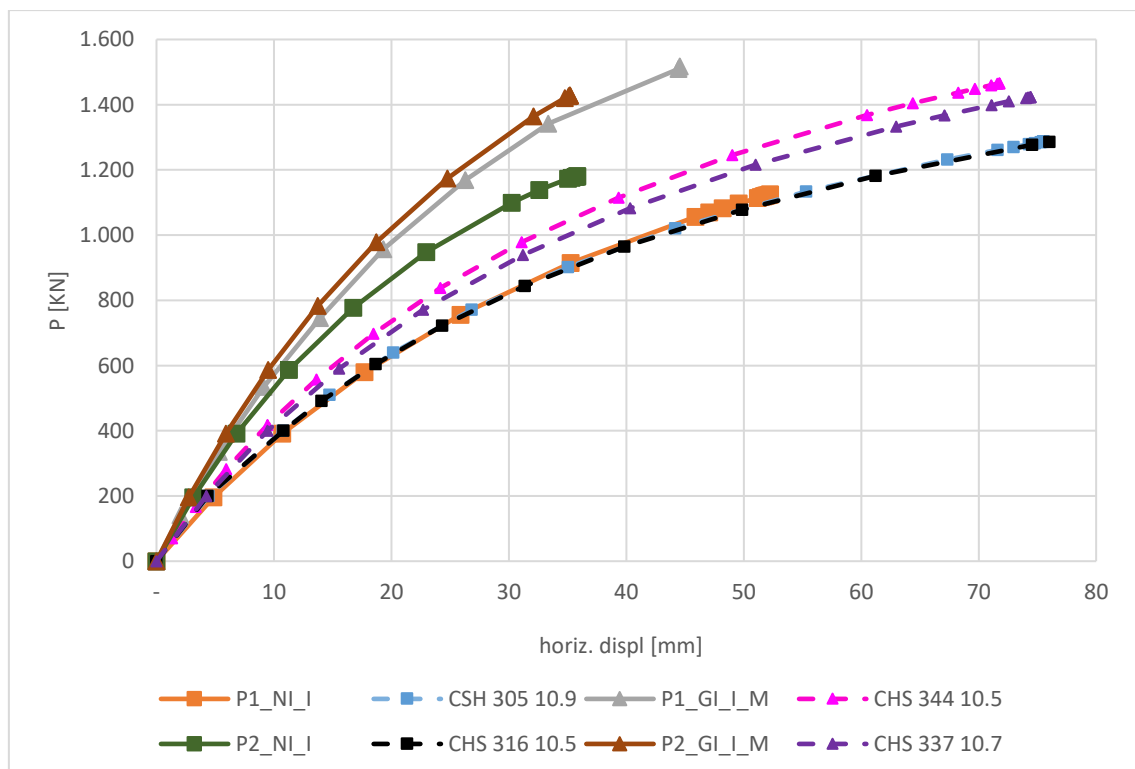
13.2.2 Comparison with a Simple Hollow C-S

In order to verify if these geometries are actually more efficient than a traditional hollow cross section, some test have been performed. Circular Hollow tubes of 3D printed steel have been designed so that they had the same weight and the same Eulerian load as the P_{ult} of perfect geometries.

The results of the non-linear analyses performed on GSA under the same loading and boundary conditions, and same level of imperfections are summarized in Graph 8 and Table 14.

As we can see from the table the ultimate load of the columns designed without imperfections (NI_I) is lower than the CHS column. Hence these columns cannot be considered better than traditional hollow C-S. The process of optimization with initial imperfections (GI), instead, brought to geometries with slightly advantageous bearing capacity.

Another major advantage is the serviceability of the column. In fact, as we can see from the graph, all the designed columns result significantly stiffer than the traditional hollow C-S with the same material properties.



Graph 8. Results of Incremental analysis for comparison with traditional hollow C-Ss

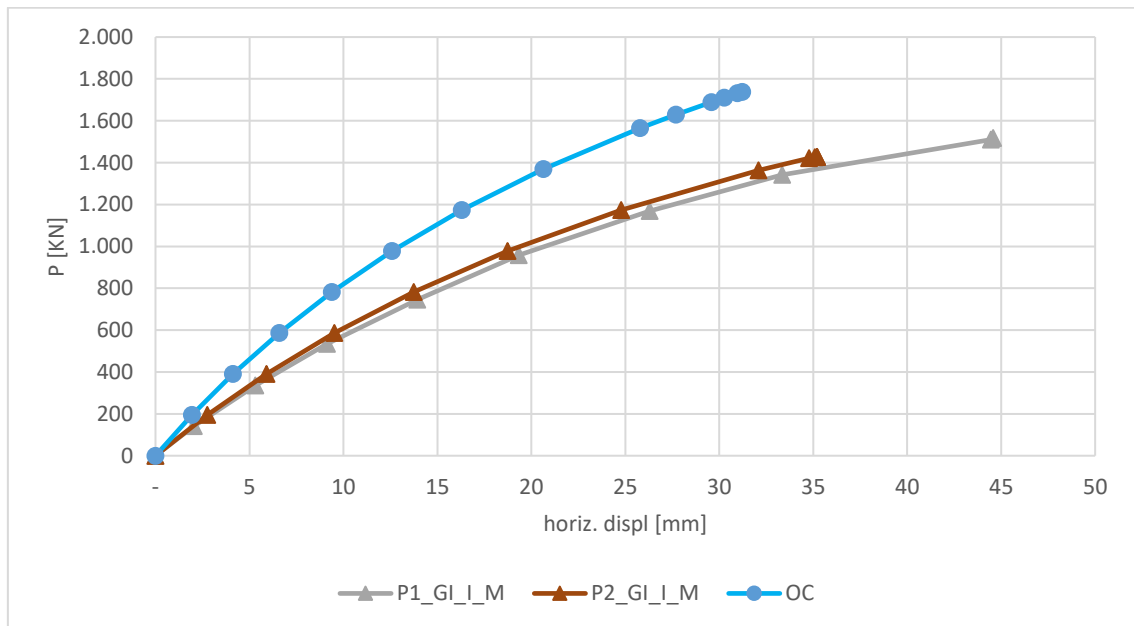
Table 14. Comparison of derived geometries and traditional hollow cross sections

I.D	CHS 305 10.9	CHS 344 10.5	CHS 316 10.5	CHS 337 10.7
REFERENCE COLUMN ⁶	P1_NI_P	P1_GI_P_M	P2_NI_P	P2_GI_P_M
m (kg)	557	607	560	609
d (mm)	305	344	316	337
t (mm)	10.9	10.5	10.5	10.7
P_{cr} (kN)	2192	3072	2388	2955
P_{ult} (kN)	1287	1466	1286	1424
P_{ult}/m (kN/kg)	2.31	2.42	2.30	2.34
$P_{ult}/P_{ult,rc_I}$ ⁷	1.14	0.97	1.24	1.00

13.3 COMPARISON WITH ORIGINAL COLUMN

Part of the analysis involves also the comparison with the element in place, the original CHS column (OC). For this study, a non-linear analysis on OC with the imperfections prescribed by EC3 has been performed.

The comparison is performed with the worst-case scenario, that means that both geometries are affected by global imperfections. The reason for this choice is obvious. Since the real structure would be affected by imperfections, it is not reasonable to perform a comparison with a design that is technologically not achievable. Hence, between all the structures presented in the previous chapters, only the GI_I_M are considered.



Graph 9. Incremental analysis for optimised geometries with imperfections and original column.

⁶ Column with same Eulerian load and mass

⁷ P_{ult,rc_I} is the critical load of the solution of the reference column with imperfections

Table 15. Summary of performance of the imperfect geometries

I.D	P1_GI_I_M	P2_GI_I_M	OC
m (kg)	607	609	554
P_{ult} (kN)	1507	1428	1738
P_{ult}/m (kN/kg)	2.48	2.34	3.14
P_{ult}/P_0	0.77	0.73	0.89

As we can see from Graph 9, thanks to a Young modulus that is more than twice the Young modulus of 3D printed steel, OC displaces less than the 3D printed columns and hence less stresses are developed. As a consequence, OC is capable to carry higher loads compared to the geometries that have been found.

Furthermore, the element in place has a lower mass. The combination of strength and lightness make OC much more efficient than the 3D printed columns that have been developed.

DISCUSSION

14 CONCLUSIONS

14.1 SUMMARY OF THE PROCESS

The basic knowledge needed to approach the world of structural optimization for WAAM elements has been summarised. The advantages and disadvantages of 3D printed steel columns have been introduced and further discussed in the analysis. The unit of comparison used for assessing these advantages and disadvantages was the structural optimization of a 7 m branch of a dendriform column. In order to evaluate the level of optimization of the element a mathematical approach, based on identification of the geometry with the lowest mass, has been used.

In order to find the optimized geometry an algorithm has been generated. This algorithm takes as input the parametric geometry its boundary conditions and performs two non-linear analysis: the first to identify the internal forces and perform the size optimization and a second to compute the actions on the elements. This algorithm was integrated with an evolutionary solver to solve the optimization problem and find the parametric description of the optimized geometry were the resistance (limit on U) and the stability of the structure (limit on displacements).

Some initial assumptions have been made to limit the feasible domain of the optimization problem: These assumptions were necessary to take into account external constraints like:

- the compatibility of the distribution of the material (limit on the size of the cross sections and minimum spacing)
- the constructability of the connections (definition of r_r)
- the computational cost of optimization problems

Due to the complexity and novelty of the topic, some other assumptions had to be made concerning the shape of the column. Despite, theoretically any shape is achievable thanks to 3D printing, in order to perform the structural analysis a mesh made of only 1D elements was chosen. Hence one of the assumptions was the mesh to be optimized. Another assumption was the external shape. From the literature a solution for a circular hollow strut has been retrieved. As a further analysis, this has been compared with a sine-shaped column.

Once the problem was fully defined, the optimization algorithm has been applied and the parametric description of the optimum solution identified. For this task the evolutionary solver was used. In order to ensure the stability of the algorithms, displacements, actions and utilization of elements are plotted as a function of the applied load. The location of the spurious peaks is then compared to the output the “*Buckling Mode*” component of the

FEM software to identify a threshold to the solutions that are considered safe from non-convergence ($BF > 1.1$).

Two types of constrains have been used as hard constrains for the analysis: one based on resistance ($U < 1$) and one based on serviceability, based on displacements as fractions of the length. The analysis has been run for 4 different combinations of external shape and levels of imperfection.

Imperfection Pattern	NI	GI
p1	P1_NI	P1_GI
p2	P2_NI	P2_GI

14.2 SUMMARY OF RESULTS

The geometries obtained from the optimization process have then been analysed and compared with the element on site and with circular hollow tubes with same imperfections, material, critical load and weight. According to the results, moving from Karamba, where the structures resulted very optimized for the constrains set, to GSA, where the actual strength properties are tested (geometrical and material non-linear analysis), the structures resulted still slightly oversized, with about a 20% safety margin that make the structures not fully optimized. These behaviours are identified only when the structures have been tested under their design conditions. In fact, as soon as imperfections (note that $e_0 \approx 44mm$) are added the load capacity is reduced of about 50%.

GEOM.	P1_NI	P1_GI_M	P2_NI	P2_GI_M
$P_{ult,I}/P_{ult,P}^8$	55%	63%	45%	62%

Comparing the structural performances of the optimized geometries with circular hollow 3D printed tubes with same imperfections and critical load the results varied depending on the condition under which the structures had been optimized. When no imperfections were added in the optimization process the geometries resulted weaker than the normal tubes. When GIs were added instead, the resulting geometry (GI_M) performed equally or better (3% of additional load bearing capacity) than the tubes.

Contrarily, when the geometries are compared to the original column, made of traditional steel and produced according to the traditional processes (imperfections according to EC3), the geometries resulted 14% and 17% weaker for p_1 and p_2 respectively.

Considering the results of the two comparisons, we can conclude that, under the conditions studied in this thesis and the actual state of the technology, the reduced Young modulus and the higher level of imperfections, make 3D printed steel elements not suitable for improving the structural performance of steel columns.

⁸ Ultimate load of imperfect geometry divided by ultimate load of perfect geometry

15 ANSWERS TO THE RESEARCH QUESTIONS

- How would an optimized 3D printed column look like?

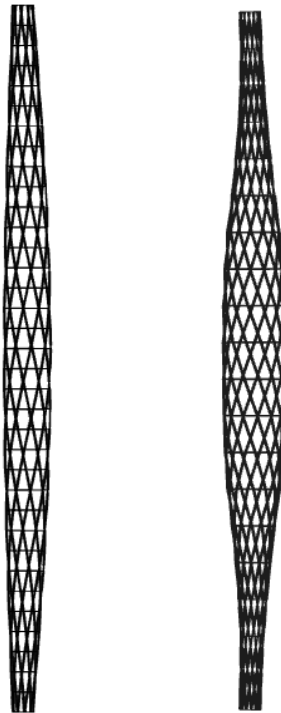


Figure 62. Optimized 3D printed geometries

According to shapes, mesh, boundary conditions, design load and hard constraints set for the analyses the appearance of column is the one reported in Figure 62. The sine-shaped one weights about 607 kg and has a radius of 330mm in the centre. The other one has a mass of 609 kg and is 400mm thick in the centre (GI_M geometries).

- Is it already possible to achieve better performances with 3D printing?

Although general conclusion cannot be drawn, according to the results obtained from the case study, thanks to a higher Young modulus and lower imperfections traditional steel elements should still be preferred for structural applications.

16 FINAL REMARKS AND FUTURE RESEARCH

As highlighted in the conclusions the Young modulus is the key element for the design and optimization of structural elements. Further research is needed to reduce the uncertainties related to its value. Furthermore, the material shows highly anisotropic behaviours depending on the printing direction and angle [6], [48]the designer should be conscious and take into account the differences in properties according to the printing

direction. Hence, specific knowledge and familiarity with the printing process would be required to engineers to correctly predict the toolpath and hence the material properties.

However, this may not be compatible to the computational cost of optimization problems, where the structural analysis needs to be performed iteratively. This rises the following research questions:

- Is it possible to solve the optimization problem taking into account the printing process?
- Is it actually worth it to include it in the optimization process or the assumption of a unique Young modulus, depending on the general printing direction is sufficient?

Finally, some observations need to be done on the assumption of the imperfections of WAAM elements. As highlighted in this thesis the imperfections play a significant role in the design and optimization of the structural elements. In this thesis the imperfections have been modelled in accordance with the EC3, that is not meant to 3D printed steel structures. As highlighted by van Bolderen [3] the imperfections of 3D printed elements are mainly associated to misalignment in the deposition of one layer onto the other, than due to general crookedness of the structural elements. Hence the following research question:

- Are the procedures suggested in EC3 suitable to ensure a correct modelling of 3D printed structures?

REFERENCES

- [1] I. Block, “Robots complete span of 3D-printed bridge for Amsterdam canal,” 2018. [Online]. Available: <https://www.dezeen.com/2018/04/17/mx3d-3d-printed-bridge-joris-laarman-arup-amsterdam-netherlands/>. [Accessed: 17-Jun-2018].
- [2] E. Williamns, “3D-Printing the Most Ornate Room | Hackaday,” 2015. [Online]. Available: <https://hackaday.com/2015/12/12/3d-printing-the-most-ornate-possible-room/>. [Accessed: 17-Jun-2018].
- [3] R. Stott, “Gallery of LCD’s VULCAN Awarded Guinness World Record for Largest 3D Printed Structure - 13,” 2015. [Online]. Available: <https://www.archdaily.com/776169/lcds-vulcan-awarded-guinness-world-record-for-largest-3d-printed-structure/5630d5abe58ece22ae00047c-lcds-vulcan-awarded-guinness-world-record-for-largest-3d-printed-structure-image>. [Accessed: 21-Jun-2018].
- [4] L. P. L. van der Linden, “Innovative Joints For Gridshells,” Delft University of Technology, 2015.
- [5] S. Galjaard, S. Hofman, N. Perry, and S. Ren, “Optimizing Structural Building Elements in Metal by using Additive Manufacturing,” *Int. Assoc. Shell Spat. Struct.*, no. August, 2015.
- [6] G. S. Van Bolderen, “Exploration of Stability of 3D-Printed Steel Members,” Delft University of Technology, 2017.
- [7] M. Attaran, “The rise of 3-D printing: The advantages of additive manufacturing over traditional manufacturing,” *Bus. Horiz.*, vol. 60, no. 5, pp. 677–688, 2017.
- [8] W. E. Frazier, “Metal additive manufacturing: A review,” *J. Mater. Eng. Perform.*, vol. 23, no. 6, pp. 1917–1928, 2014.
- [9] “3D printed ship’s propeller takes step closer to completion.” [Online]. Available: https://www.damen.com/en/news/2017/09/3d_printed_ships_propeller_takes_step_closer_to_completion. [Accessed: 24-May-2018].
- [10] “Home - RAMLAB.” [Online]. Available: <http://www.ramlab.com/>. [Accessed: 17-Jun-2018].
- [11] T. Trombetti, M. Palermo, and V. Laghi, “MX3D-DICAM COLLABORATION: UPDATES AND FURTHER DEVELOPMENTS,” 2018.
- [12] “MX3D Bridge.” [Online]. Available: <http://mx3d.com/projects/bridge/>. [Accessed: 15-Jun-2018].
- [13] F. Martina and S. Williams, “Wire+arc additive manufacturing vs. traditional machining from solid: a cost comparison,” p. 27, 2015.
- [14] “How Does Powder-Based 3D Printing Work? | Help Center | i.materialise.” [Online]. Available: <https://imaterialise.helpjuice.com/design-printing/powder->

- based-3d-printing. [Accessed: 25-May-2018].
- [15] “Optomoec LENS MR-7 multi-material metal 3D printer - High performance metals.” [Online]. Available: <https://research.csiro.au/metals/add-manufacturing/aus-innovation/optomoec-lens-mr-7-multi-material-3d-printer/>. [Accessed: 24-May-2018].
- [16] “Additive Manufacturing Enables Fast Modification of Molds.” [Online]. Available: <https://www.or-laser.com/en/news/additive-manufacturing-enables-fast-modification-of-molds/>. [Accessed: 17-Jun-2018].
- [17] V. Laghi, M. Palermo, M. Pragliola, V. A. Girelli, G. Van der Velden, and T. Trombetti, “Towards 3D-printed steel grid-shells : the idea and first studies,” in *International Association of Spatial Structures, Boston, USA*, 2018.
- [18] V. Laghi, M. Palermo, and T. Trombetti, “Buckling Tests on 3D-Printed Tubular Elements.” University of Bologna (Under development), 2018.
- [19] O. Querin, M. Victoria, C. Alonso, A. Rubén, and R. Marti, “Topology Design Methods for Structural Optimization,” 2017.
- [20] M. P. Bendsoe and O. Sigmund, *Topology optimization: theory, methods, and applications*, vol. 2nd Editio, no. 724. 2003.
- [21] W. R. Spillers and K. M. MacBain, *Structural Optimization*. 2009.
- [22] K. Proos, “Evolutionary Structural Optimisation as a Robust and Reliable Design Tool,” The University of Sydney, 2002.
- [23] A. Melazzini, “Vilfredo Pareto Tenacino : ‘ Signore Incaricato ’ nella società del ferro In Valdarno,” 1999.
- [24] “Optimal Design.” University of Trento, 2017.
- [25] Z. H. Huang, L. L. Zhang, S. Y. Cheng, J. Zhang, and X. H. Xia, “Back-Analysis and Parameter Identification for Deep Excavation Based on Pareto Multiobjective Optimization,” *J. Aerosp. Eng.*, vol. 28, no. 6, p. A4014007, Nov. 2015.
- [26] D. Anderson *et al.*, “Złote Tarasy, Warsaw , Poland,” *Arup J.*, vol. 1, 2008.
- [27] “Złote Tarasy z wysokości - NaszeMiasto.pl.” [Online]. Available: <http://warszawa.naszemiesto.pl/arttykul/zdjecia/zlote-tarasy-z-wysokosci,3701894,galop,19660056,t,id,tm,zid.html>. [Accessed: 24-May-2018].
- [28] “Galeria Złote Tarasy - zdjęcia - Kolumber.pl.” [Online]. Available: <http://kolumber.pl/photos/show/golist:26673/page:18>. [Accessed: 24-May-2018].
- [29] “złote tarasy - Google Maps.” [Online]. Available: <https://www.google.com/maps/search/zlote+tarasy/@52.2282867,21.0081401,244a,35y,288.24h,61.34t/data=!3m1!1e3>. [Accessed: 23-May-2018].
- [30] “GSA Suite | Oasys.” .
- [31] Robert McNeel & Associates, “Rhino.” .
- [32] S. Davidson, “Grasshopper - algorithmic modeling for Rhino.” .
- [33] C. Preisinger, “Linking Structure and Parametric Geometry,” *Archit. Des.*, vol. 83,

no. 2, pp. 110–113, Mar. 2013.

- [34] L. L. Beghini, A. Beghini, N. Katz, W. F. Baker, and G. H. Paulino, “Connecting architecture and engineering through structural topology optimization,” *Eng. Struct.*, vol. 59, pp. 716–726, 2014.
- [35] L. L. Stromberg, A. Beghini, W. F. Baker, and G. H. Paulino, “Application of layout and topology optimization using pattern gradation for the conceptual design of buildings,” *Struct. Multidiscip. Optim.*, vol. 43, no. 2, pp. 165–180, 2011.
- [36] H. Rubin and K.-J. Schneider, *Baustatik - Theorie I. und II. Ordnung*. Werner, 2002.
- [37] H. Rubin, “Uniform formulae of first- and second-order theory for skeletal structures,” *Eng. Struct.*, vol. 19, no. 11, pp. 903–909, Nov. 1997.
- [38] Oasys, “Oasys GSA8.7.” .
- [39] Technical University of Denmark, “Apps/ software - TopOpt.” .
- [40] A. Bejan, *Shape and Structure, from Engineering to Nature*. Entropy, 2001.
- [41] M. Beckh and J. Wiley, *Hyperbolic structures: Shukhov’s lattice towers - forerunners of modern lightweight construction*. John Wiley & Sons, Incorporated.
- [42] M. Dini, G. Estrada, M. Froli, and N. Baldassini, “Form-finding and buckling optimisation of gridshells using genetic algorithms,” *Wroclaw Univ. Technol. Pol. J.B. Obrebski R*, 2013.
- [43] C. Preisinger, “Parametric Structural Modelling (Karamba) User Manual for Version 1.2.2.” pp. 1–142, 2016.
- [44] T. Meyer Boake and V. Hui, “SSEF - Fun is in the Details - Hinge and Pin Connections,” *Canadian Institute of Steel Construction*. [Online]. Available: <http://www.tboake.com/SSEF1/pin.shtml>. [Accessed: 13-Jun-2018].
- [45] B. Jackson, “AML Technologies adapt WAAM 3D printing for supernova-made metal - 3D Printing Industry.” [Online]. Available: <https://3dprintingindustry.com/news/aml-technologies-adapt-waam-3d-printing-supernova-made-metal-127765/>. [Accessed: 18-Jun-2018].
- [46] Think Up, *Buckling failure of a pin ended column of low slenderness: Materials Lab on-line - YouTube*. 2015.
- [47] J. Mirtschin, “GeometryGym – OpenBIM tools for Architects, Engineers and the Construction Industry.” [Online]. Available: <https://geometrygym.wordpress.com/>. [Accessed: 03-Jul-2018].
- [48] S. K. Joosten, “Printing a stainless steel bridge: An exploration of structural properties of stainless steel additive manufactures for civil engineering purposes,” 2015.
- [49] Architecture Technology and Innovation Laboratory, “Tree like structures,” 2014.
- [50] I. M. Rian and S. Asayama, “Computational Design of a nature-inspired architectural structure using the concepts of self-similar and random fractals,” *Autom. Constr.*, vol. 66, pp. 43–58, 2016.

- [51] M. F. Barnsley, "Chapter IX Measures on Fractals," in *Fractals everywhere*, A. Press, Ed. 1988.
- [52] I. Md Rian and M. Sassone, "Tree-inspired dendriforms and fractal-like branching structures in architecture: A brief historical overview," *Front. Archit. Res.*, vol. 3, no. 3, pp. 298–323, 2014.
- [53] E. Allen, W. Zalewski, N. Michel, and Boston Structures Group., *Form and forces : designing efficient, expressive structures*. John Wiley & Sons, Inc, 2010.
- [54] M. Akbarzadeh, T. Van Mele, and P. Block, "On the equilibrium of funicular polyhedral frames and convex polyhedral force diagrams," *CAD Comput. Aided Des.*, vol. 63, pp. 118–128, 2015.
- [55] Peregoy Beau, "5 of the Best Art Nouveau Buildings in Paris Photos | Architectural Digest," 2016. [Online]. Available: <https://www.architecturaldigest.com/gallery/art-nouveau-paris>. [Accessed: 03-Mar-2018].
- [56] P. Metivier, "Grand Palais, Stairs, Paris." [Online]. Available: <https://www.flickr.com/photos/feuillu/46031551>. [Accessed: 03-Mar-2018].
- [57] P. A. Funes, "Barcelona Catechism." [Online]. Available: http://www.sacredarchitecture.org/articles/barcelona_catechism. [Accessed: 03-Mar-2018].
- [58] F. Ahmeti, "Efficiency of Lightweight Structural Forms : The Case of Tree- like Structures - A comparative Structural Analysis," 2007.
- [59] "Introduction to Fractal Geometry." [Online]. Available: <http://www.fractal.org/Bewustzijns-Besturings-Model/Fractals-Useful-Beauty.htm>. [Accessed: 03-Mar-2018].

APPENDICES

I. DENDRIFORM STRUCTURES

As highlighted by the name itself, dendriform structures, also called branching structures, are characterized by a tree-like structure. From a technical point of view there is not a unique definition what actually a dendriform structure is, however according to Architecture Technology and Innovation Laboratory (2014), it could be defined as:

“flat or spatial structural systems which consist of separate branches, each one of which forks out at a specific point (knot) into at least two other branches. Such structures can be subjected to tension, to compression, to flexion and to torsion.”

Despite this generic observation, dendriform structures are designed to avoid bending moments and work mainly in compression. It has to be underlined, that this behaviour is the result of a structural optimization based on a specific loading condition. Therefore, the designer has to be conscious that additional load cases would lead to undesired bending moments, and the structure has to be ready to withstand also these additional stresses.

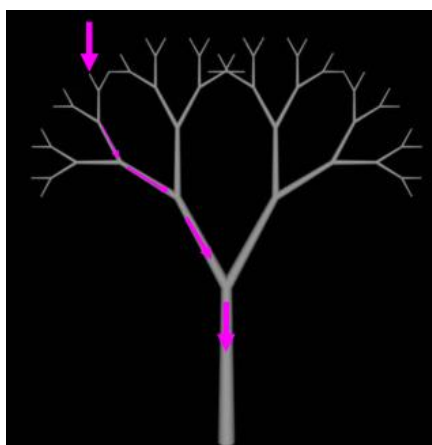


Figure 63. Tree principle [49]

The main idea behind the use of such structures is to reduce the lever arm of loads, collecting them at the application point, and transferring them through the branches to the main trunk. The main advantages of these structural systems are that the superstructure is continuously supported, and therefore the roof requests smaller supports, but at the same time the footprint at the basement level is limited and concentrated in a single location. In other words, lighter roofs, higher spans and smaller footprint. [50]

DEFINITION OF THE GEOMETRY

Morphology

As we already know in nature trees are not geometrically perfect but are affected to a certain level of randomness. However, from a structural point of view randomness is not acceptable as is associated to unpredictability. Therefore, some numerical parameters have to be defined in order to describe mathematically this sort of randomness. Self-similar fractal geometry is usually exploited in these cases.

Fractals are formed by the repetition of an original shape through a geometric transformation, and then repeating this process iteratively in the next steps for infinite times. [50]

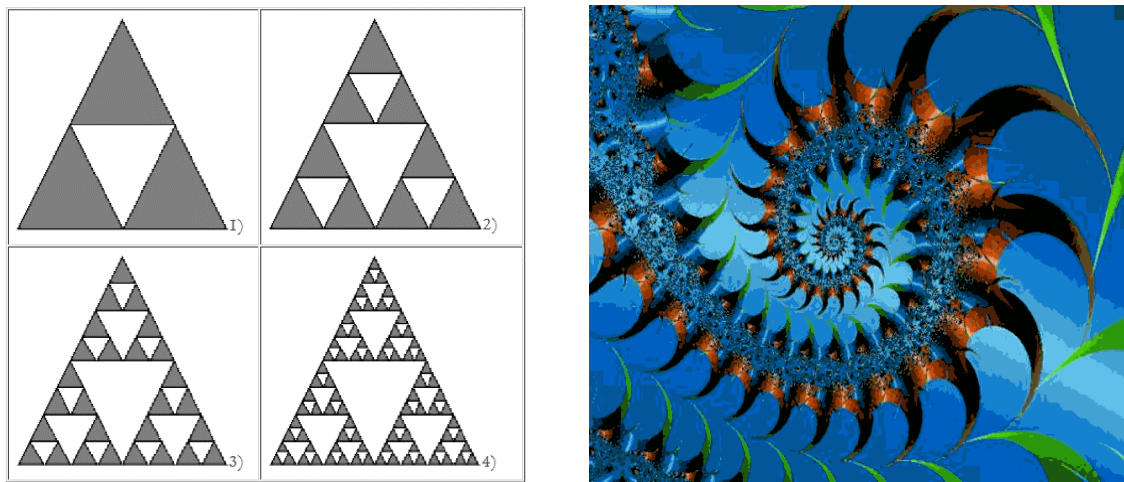


Figure 64. Examples of fractal geometries [59]

Fractals are made so that the same pattern or geometry can be iteratively repeated indefinitely at different scales, to form an infinitely complex structure. However, they are made so that their behaviour can be described by an algorithm. This last property is fundamental, as computers have been built for the purpose of solving complex algorithms. It is therefore understandable the decision to exploit the fractal geometry to design structures.

An interesting example on how to describe the fractal behaviour has been proposed by Barnsley [51]. The theory is based on a geometrical transformation of the initial geometry through a simple mathematical operator that scales, rotates and shifts the initial geometry. The 2-dimensional form is the following.

$$f = \lambda[\mu][r]\{x\} + \{\delta\} = \lambda \begin{bmatrix} \mu_1 & 0 \\ 0 & \mu_2 \end{bmatrix} \begin{bmatrix} \cos\theta & -\sin\theta \\ \sin\theta & \cos\theta \end{bmatrix} \begin{Bmatrix} x \\ y \end{Bmatrix} + \begin{Bmatrix} \delta_x \\ \delta_y \end{Bmatrix}$$

In order to maintain the initial proportions of the system the scale have to be created so that $\sum_{i=1}^k \lambda_i^D = 1$

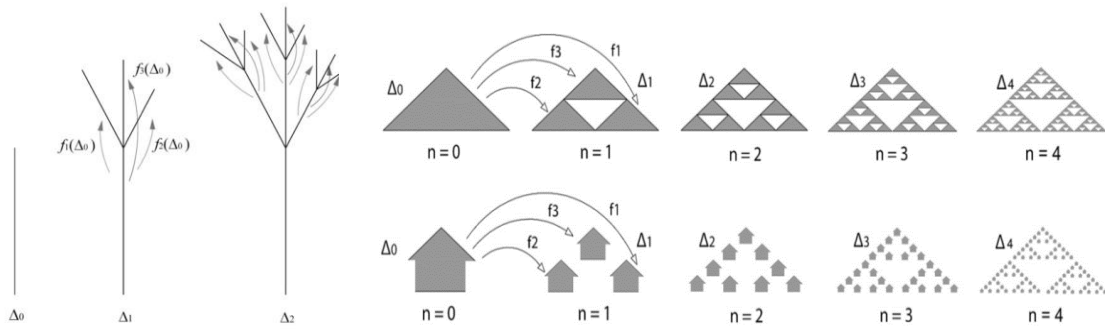


Figure 65. Examples of fractal transformations [50]

Patterns

It is evident that infinite geometries can be obtained through the geometrical transformation proposed here above. Hence it is useful to have an overview of some possible combinations of number of elements, dimensions and lengths that can be applied in the practice. These patterns are particularly useful as given the geometry the element needs to support, a possible geometry is already suggested.

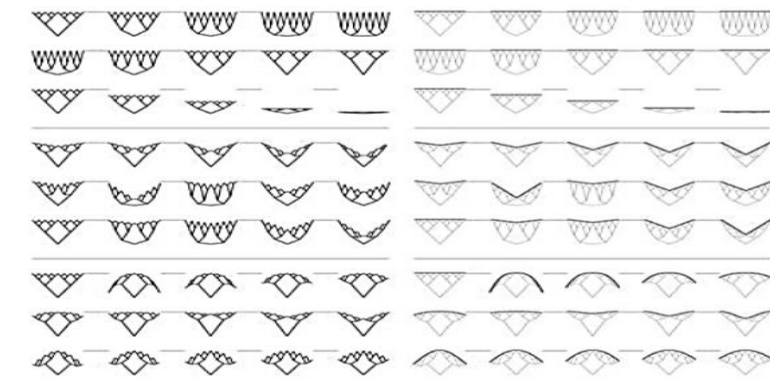


Figure 66. Examples of geometrical patterns and geometrical surface [49]

DESIGN TOOLS

When computers were still not available, there were few methods available for designing this type of structures. Otto Frei and Antonio Gaudi explored the combination of physical models and graphic statics.

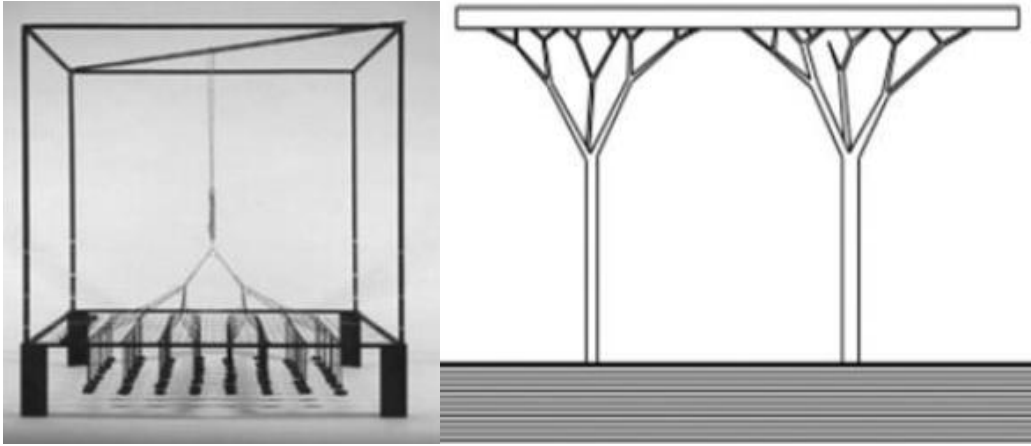


Figure 67. Otto Frei 's model for tree-like structures [49], [52]

Nowadays, the principle has remained the same. Graphic statics variations, usually in combination with more advanced computational techniques, are utilized for the analysis of dendriform structures. Advanced graphic statics [53] and 3D graphic statics [54] are good examples of this practice. The advantage of this techniques is that being graphical methods can be easily implemented into numerical algorithms for parametric design.

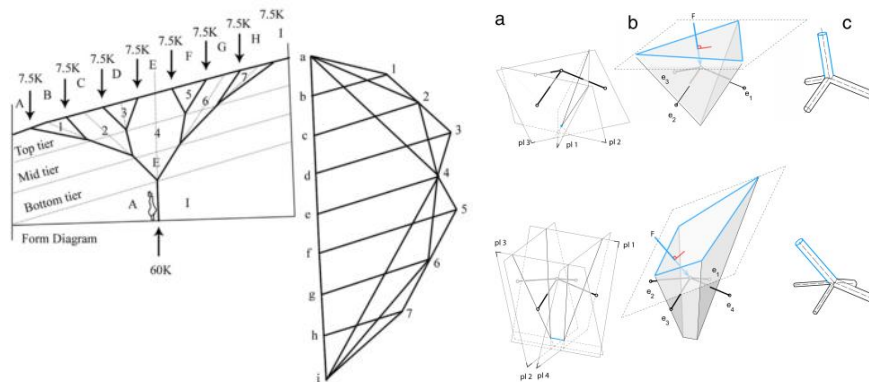


Figure 68. In the left: computer aided graphic static for the design of a market roof; in the right: convex polyhedral force diagrams for the determination of internal forces.

RECENT STRUCTURAL APPLICATIONS

Before the introduction of fractals, architects were already experimenting with tree-like structures. One of the very first examples of actual dendriform architecture is the Art Nouveau of the beginning of 20th century. One of the most relevant examples of such an architecture is the interior terrace of the Grand Palais in Paris built in 1900. [52]

Almost in the same years in Spain Gaudi was experimenting the tree-like pillars for the Sagrada Familia.



Figure 69. Terrace at Grand Palais in Paris [55], [56]

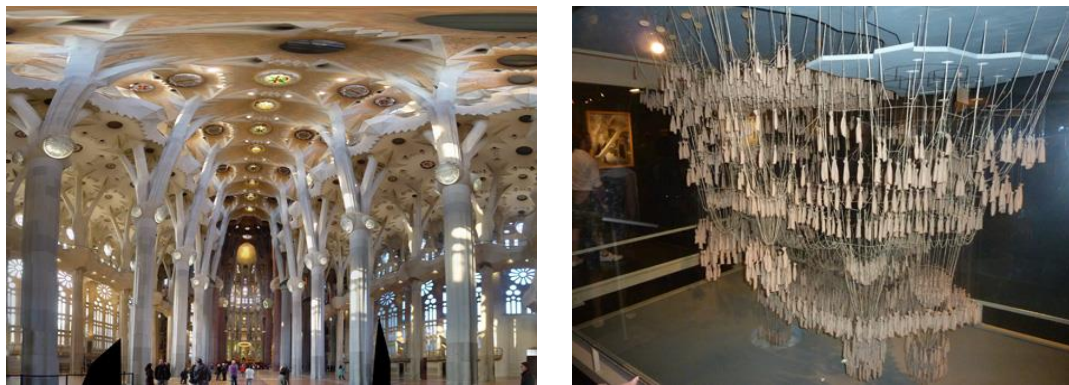


Figure 70. Detail of the dendriform pillars in the Sagrada Familia and physical model for the design of the church [57]

Thanks to the spread of computers, in the last few decades the use of these structures has grown more and more. [52], [58] Just to cite few examples of existing structures:

- 1991: Stuttgart Airport Terminal, Germany
- 1992: Palaice de Justice, Melun, France.
- 1994: Therme Bad Oeynhausen, Germany.
- 1996: Oriente Station, Lisbon, Spain.
- 2000: Beaverton Library, Oregon, USA
- 2013: Tote Restaurant, Mumbai, India.

Stuttgart Airport Terminal (1991)



Oriente Station (1996)

Palaice de Justice (1992)



Beaverton Library (2000)

Therme Bad Oeynhausen (1994)



Tote Restaurant (2013)



Looking at the pictures, it is clear how variable dendriform structures can be, both in terms of materials and geometries.

II. GENERATION OF THE MESH

i. Summary of Parameters and Conditions

Parameters:

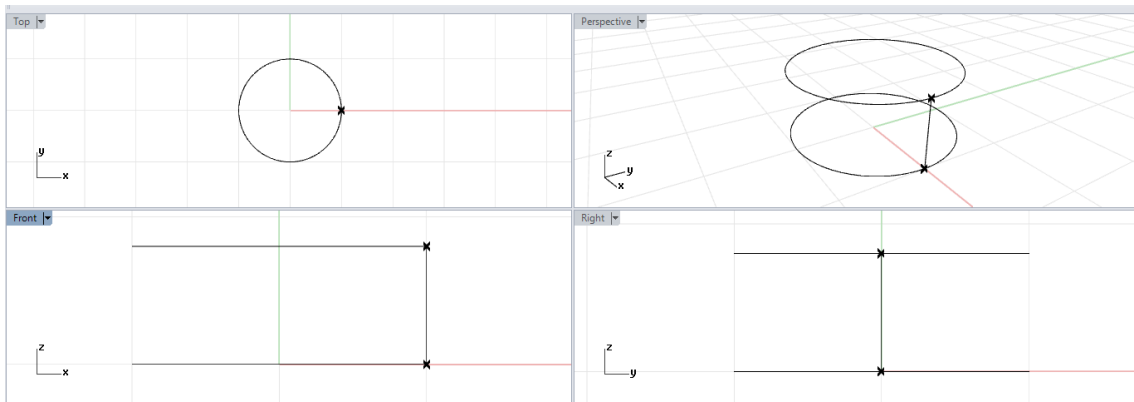
- r_r and a : reference radius and shape amplification factor (already introduced in Chapter 8.3)
- n_i : the number of inclined elements
- n_h : number of hoops
- θ : total angle of rotation of the hoops per meter in degrees

Conditions:

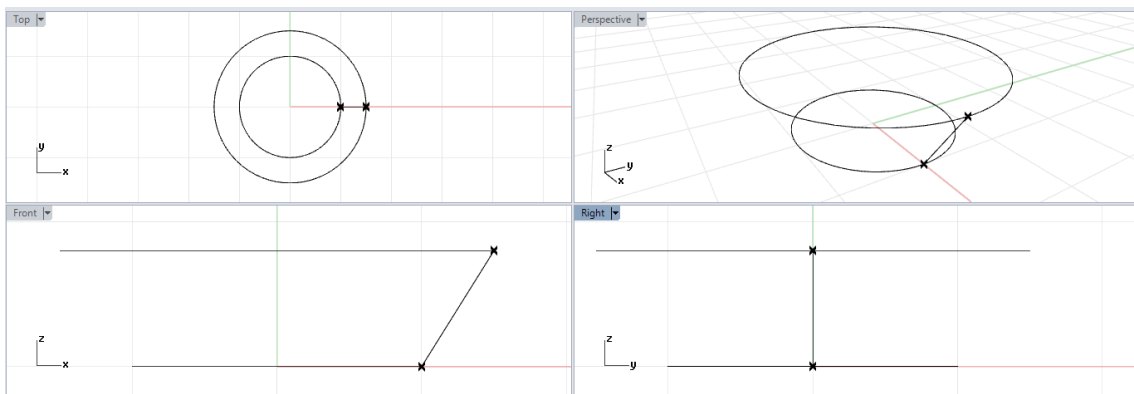
- The number of inclined elements is the same in all modules
- The inclined elements of two adjacent modules converge in the same point in the circles
- The radius of the circles is scaled according to the pattern $p(x)$ identified in Chapter 8.3.

ii. Generation Procedure

- 1) Draw two circles spaced according to n_h and connect two aligned points with a segment



- 2) Scale circles according to $R(x)$

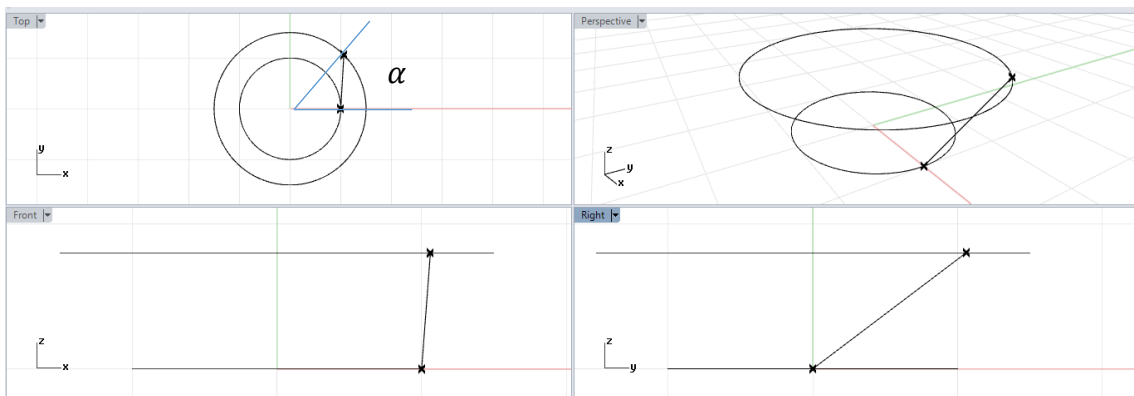


$$R(x) = r_r + a p(x)$$

x , coordinate along the axis

- 3) Rotate point along the circumference of an angle α

Example for $\alpha = 45^\circ$

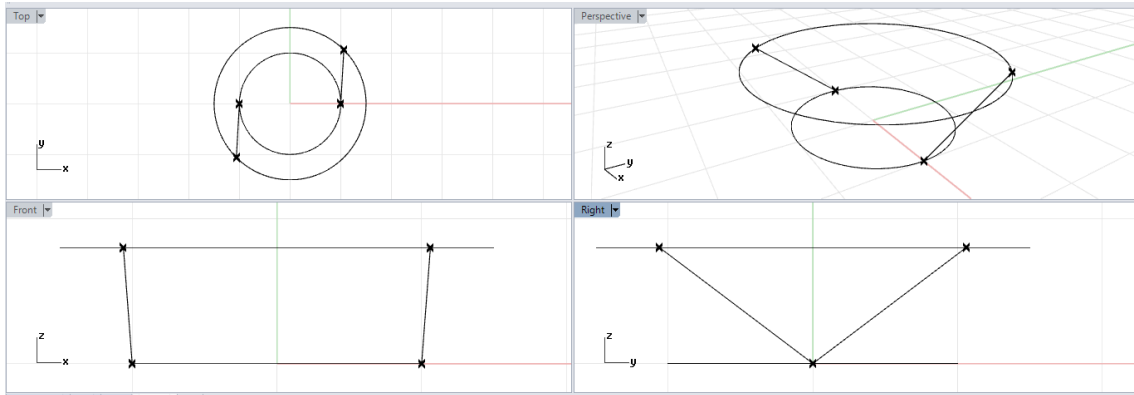


Note that: $\theta = \alpha/dx$

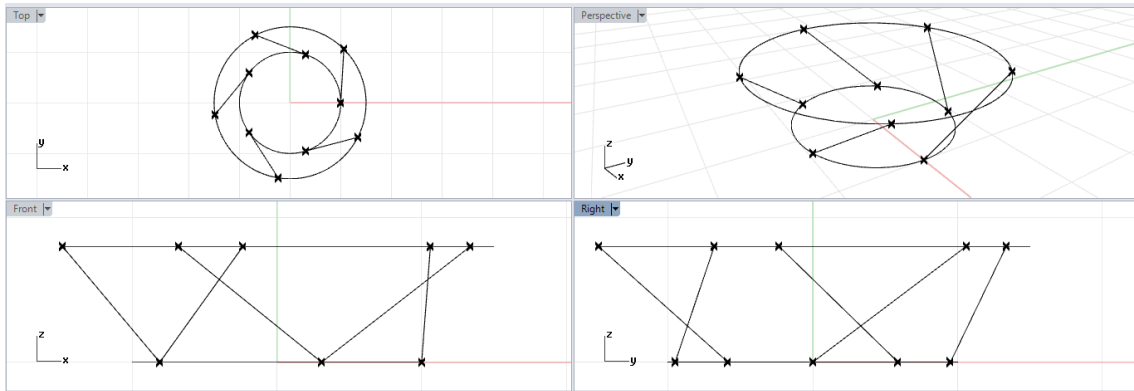
dx , distance between circles

4) Repeat the same procedure n_i times, with equispaced points

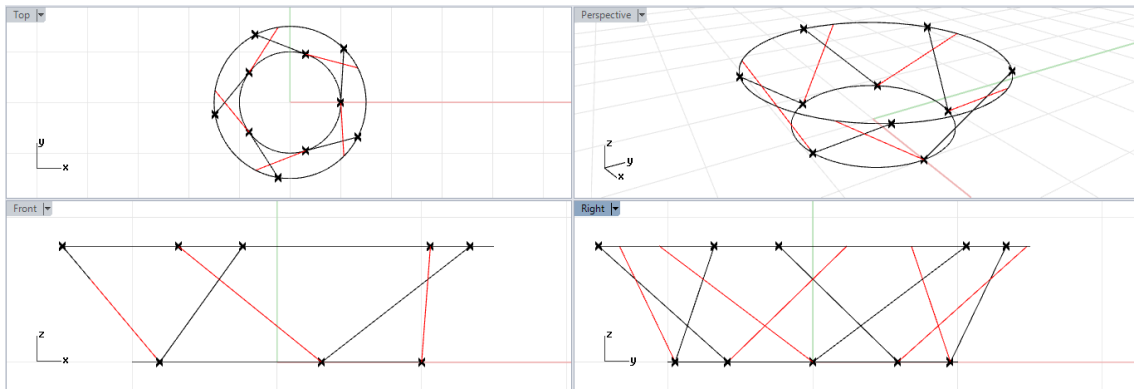
Example for $n_i = 2$



Example for $n_i = 5$

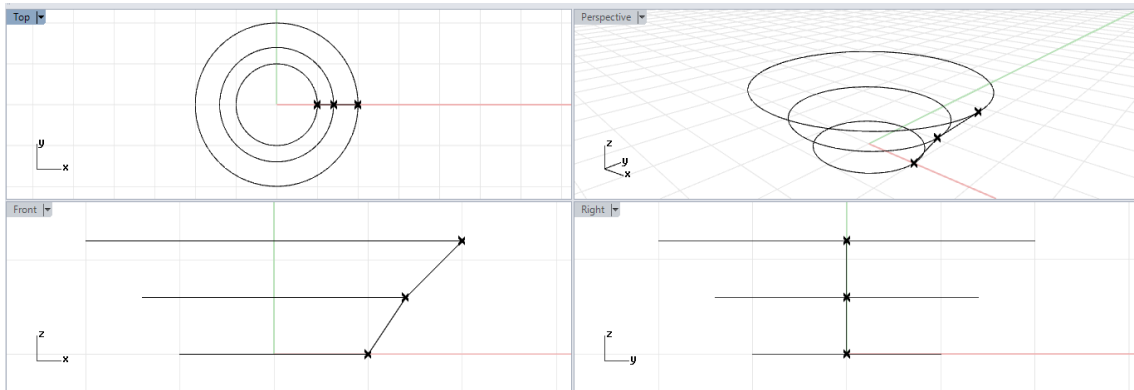


5) Apply the same procedure with $(-\alpha)$

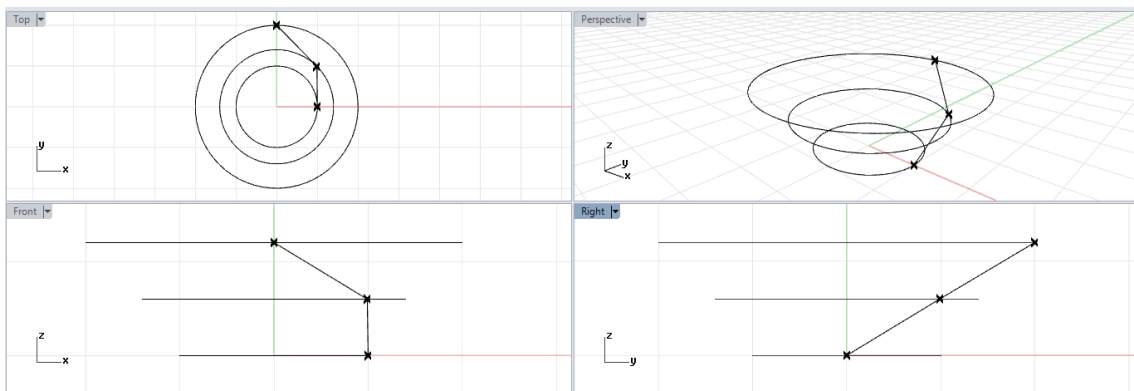


6) Apply same procedure for multiple elements

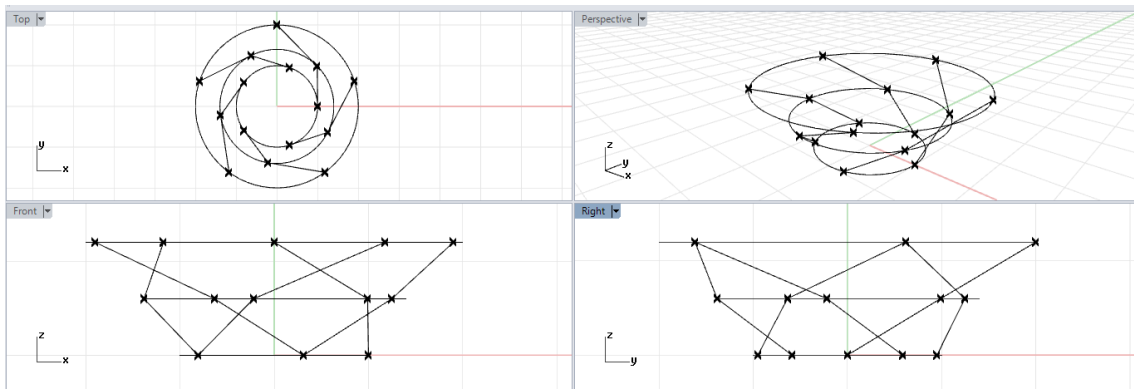
6.1



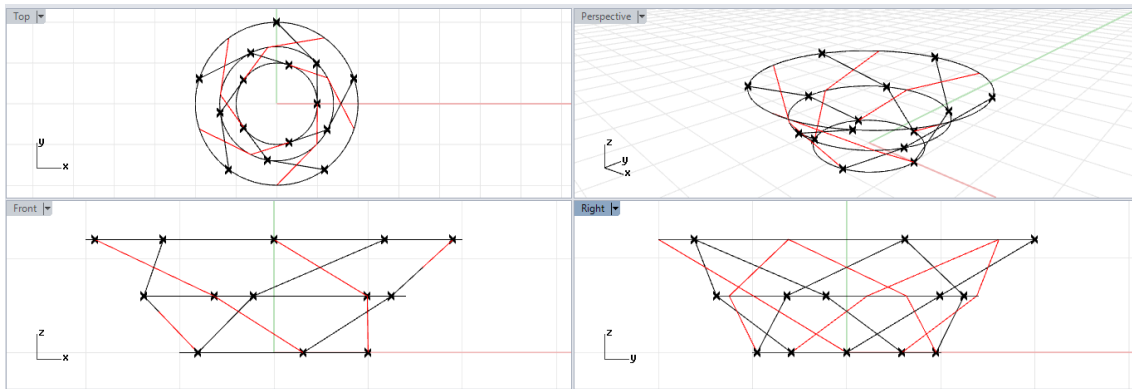
6.2



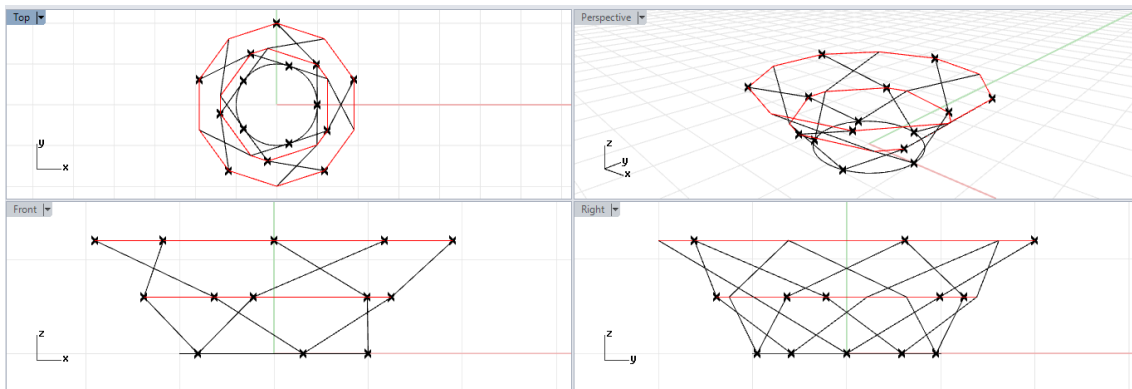
6.3



6.4



7) Transform the axes connecting the nodes into straight elements



III. FULL RESULTS TEST ON CONVERGENCE

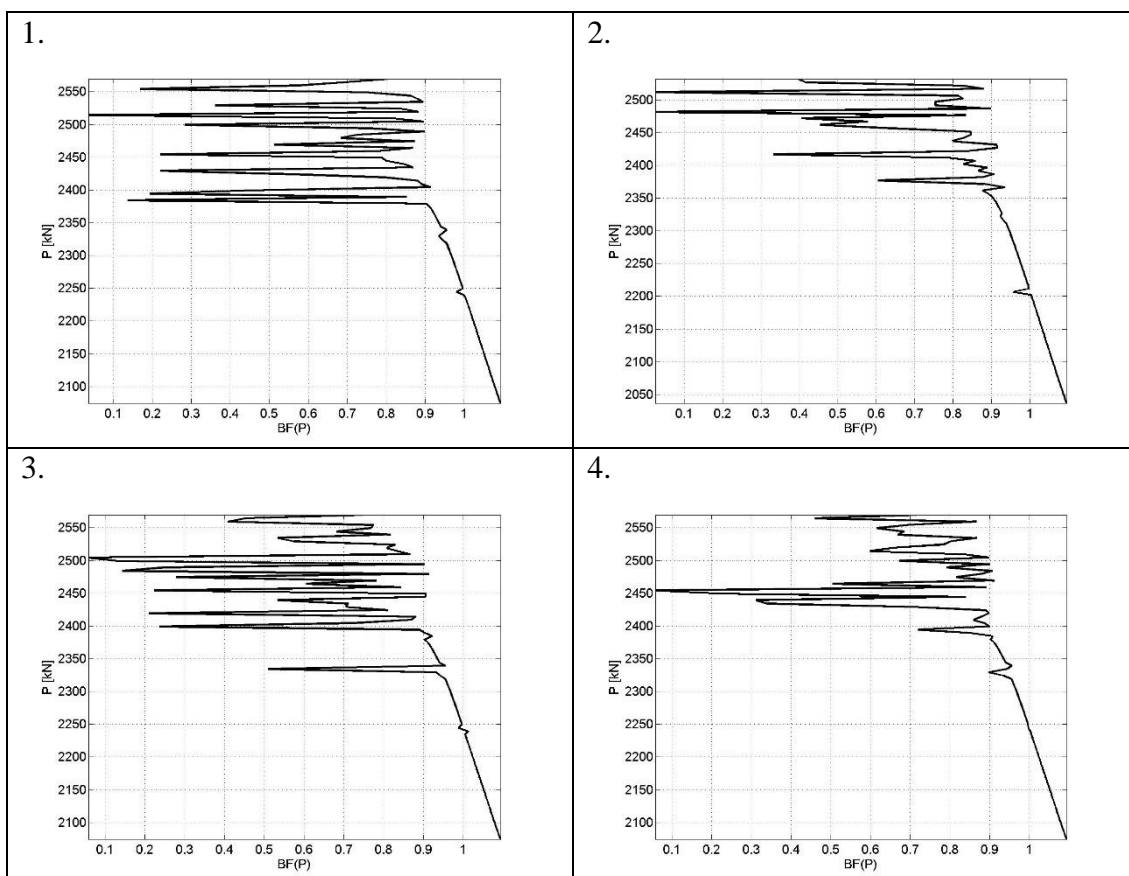
i. Geometries tested for Convergence Analysis

Here below the complete results of the convergence analysis.

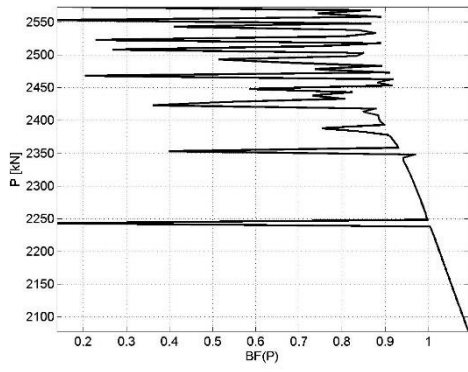
Table 16. Parametric description of the geometries that have been tested

r_r	a	n_i	n_h	θ
0	0.6	5	33	46
50	0.6	5	28	35
100	0.2	4	31	53
150	0.1	5	35	52
200	0.1	12	35	29
0	0.8	9	35	11
50	0.6	5	30	33
100	1.3	8	30	15
150	1.4	2	24	12
200	1.7	1	6	64

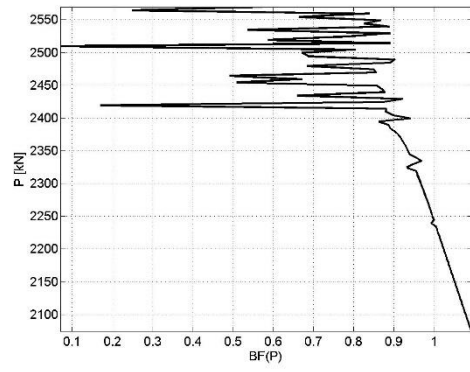
Full plot of BF as a function of applied load for the 10 geometries analysed.



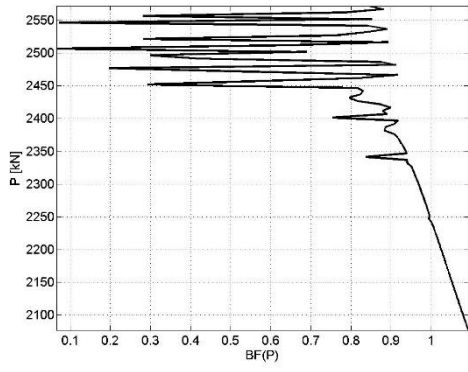
5.



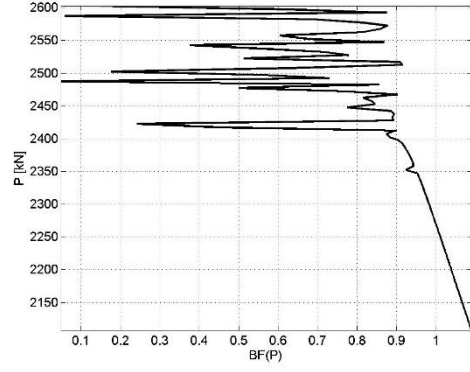
6.



7.

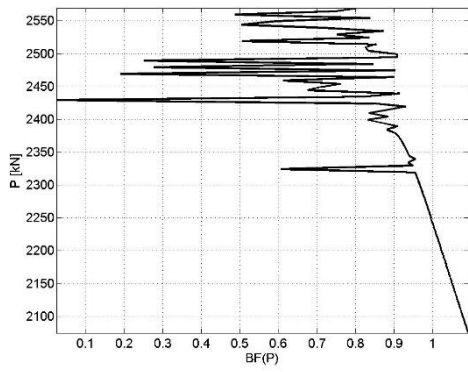


8.

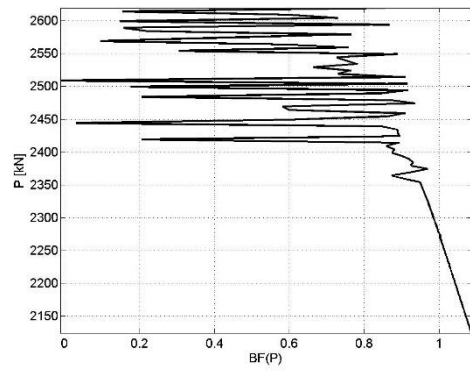


7

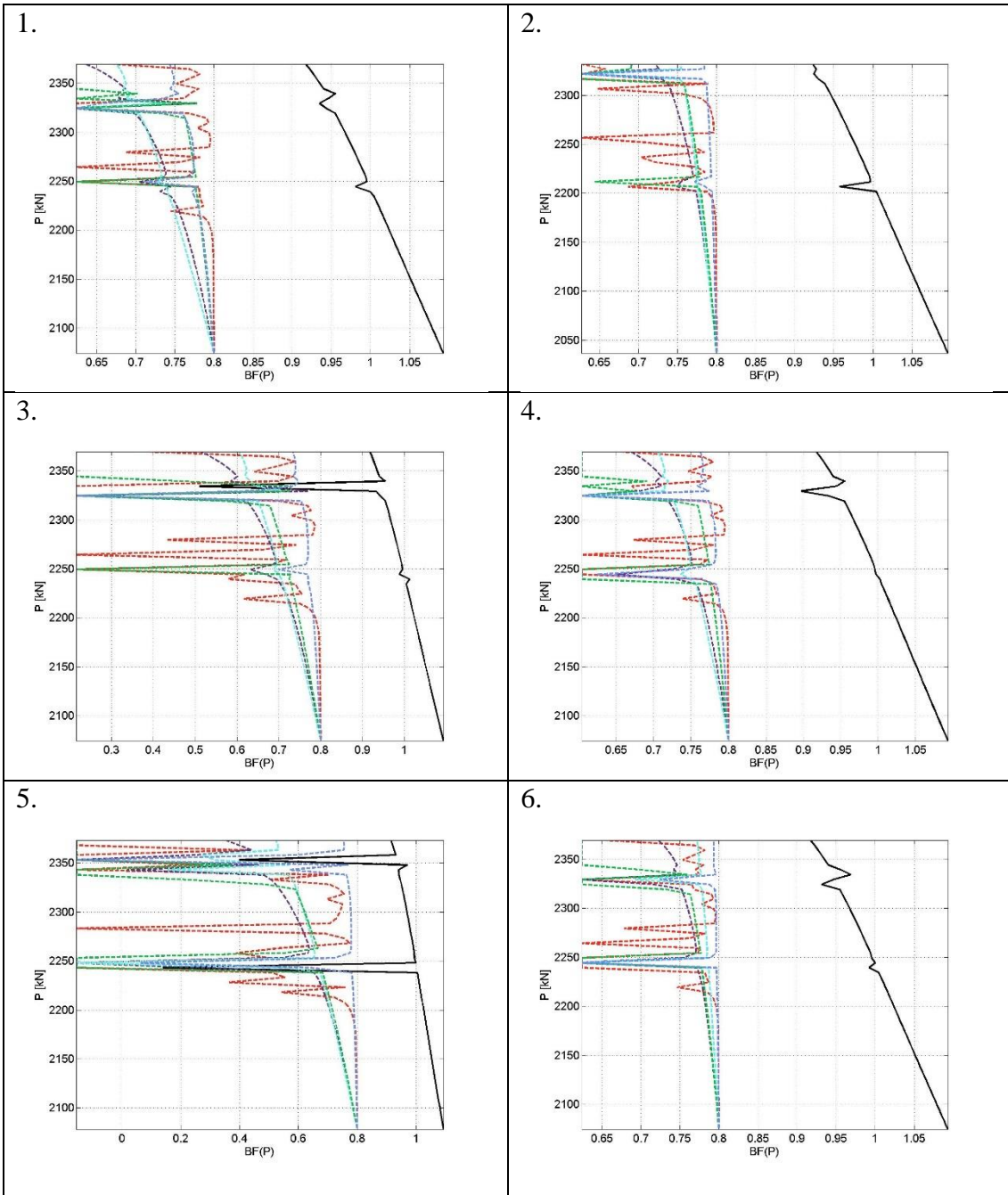
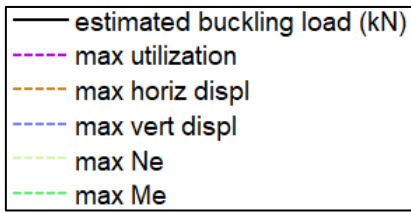
9.



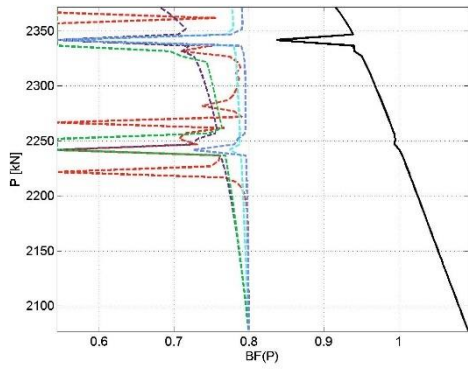
10.



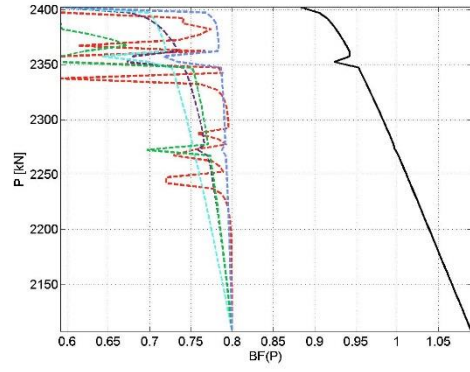
Graphs for the comparison of the peaks of the estimated buckling load and the other scaled results of the non-linear analysis.



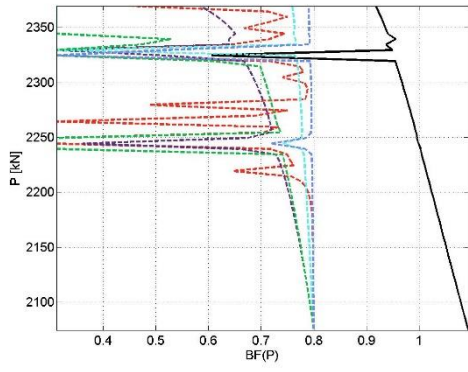
7.



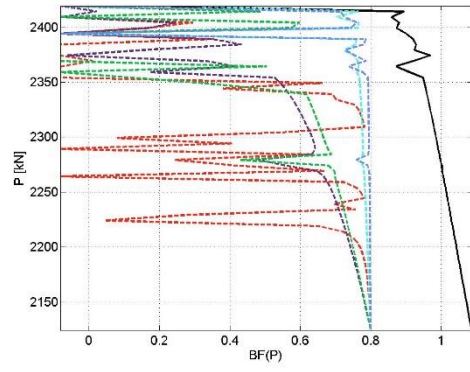
8.



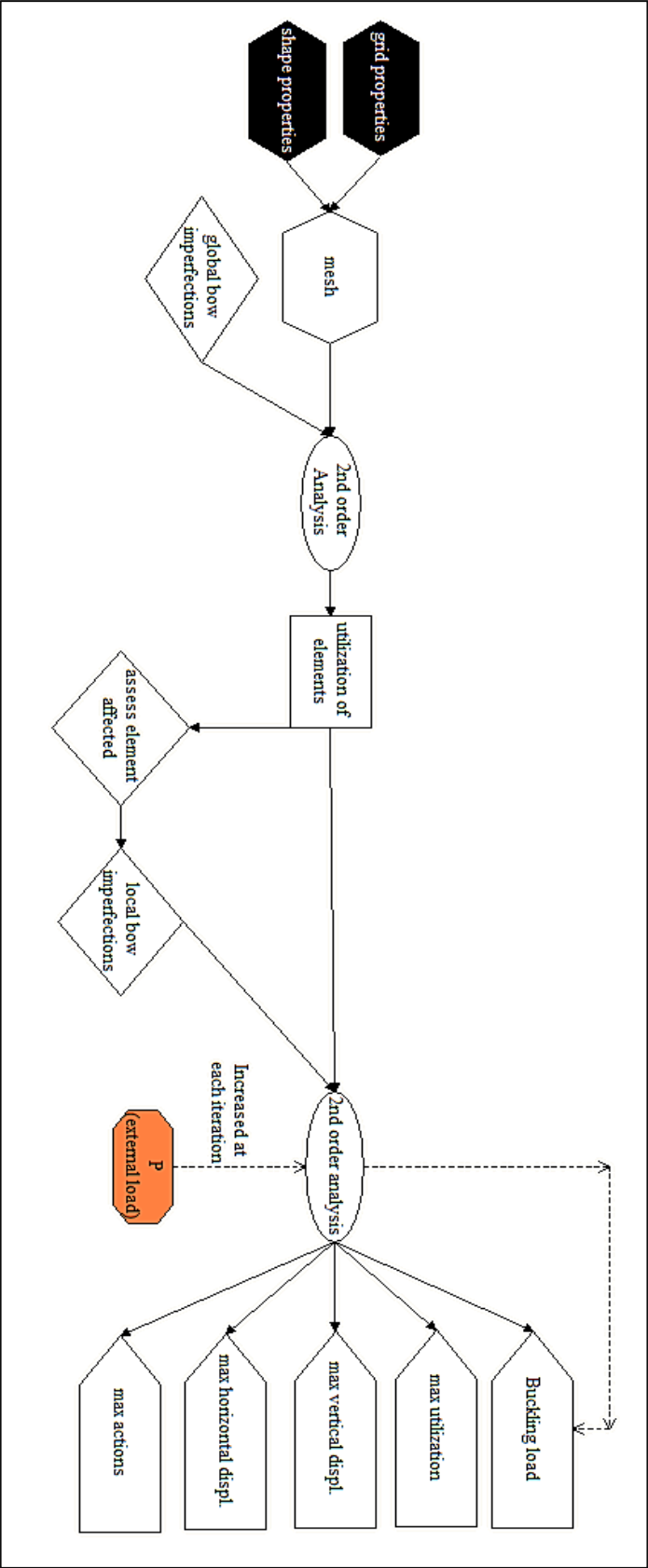
9.



10.

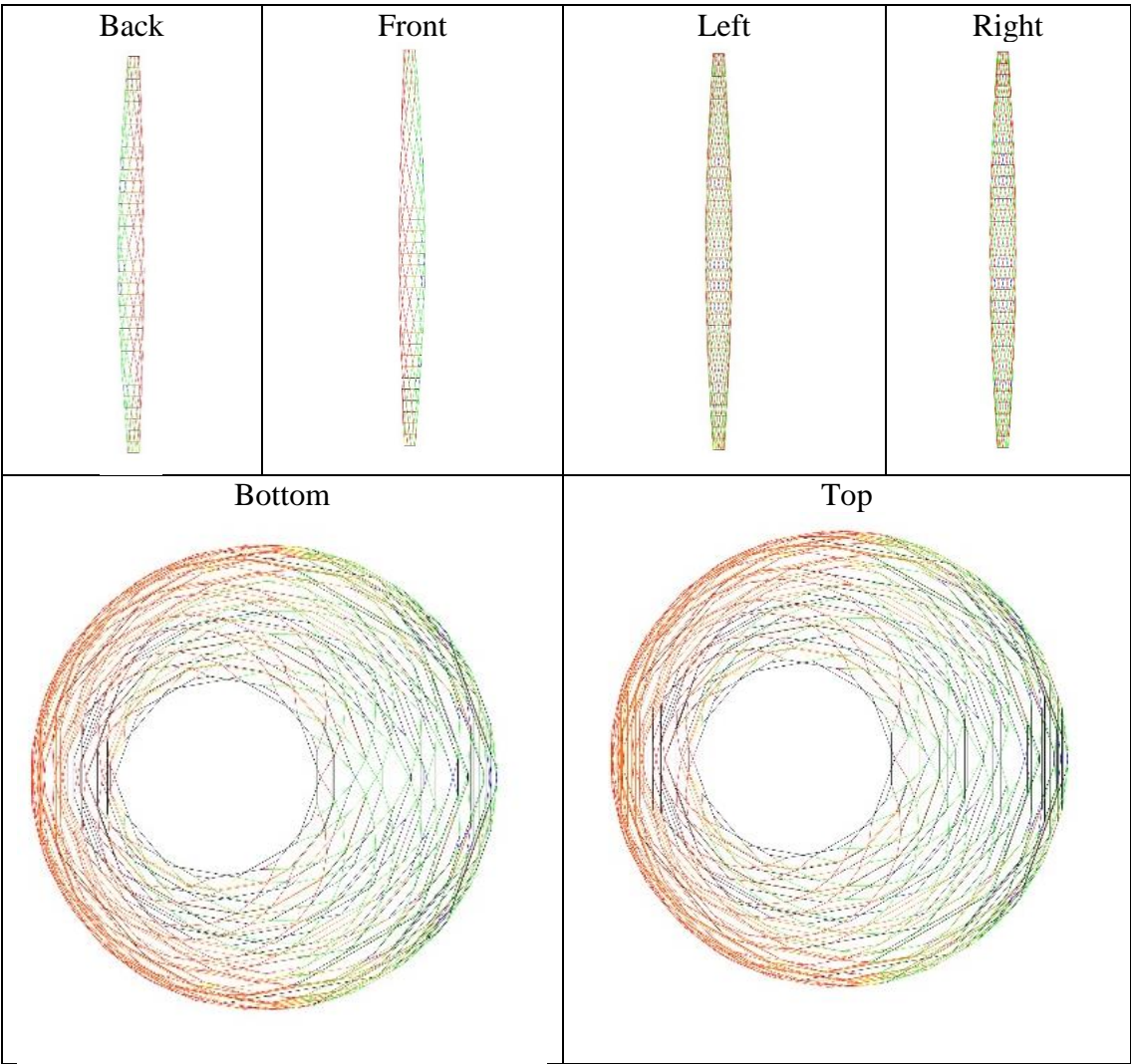


ii. Algorithm for Convergence Analysis



IV. DISTRIBUTION OF CROSS-SECTIONS FOR OPTIMIZED GEOMETRY P1_GI_I

	<i>d:40.0 t:10.0</i>
	<i>d:30.0 t: solid</i>
	<i>d:30.0 t:10.0</i>
	<i>d:30.0 t:5.0</i>
	<i>d:20.0 t: solid</i>
	<i>d:20.0 t:5.0</i>
	<i>d:10.0 t: solid</i>



V. FEEDSTOCK MATERIALS

Two different products have been used to produce the specimens used in the tests performed to assess material properties and imperfections.

i. Ugiweld Welding Wire

Here below the datasheet of the material used as feedstock to produce plate shaped specimens.

UGIWELD™ 308LM

Filler metal chemical composition	C	Si	Mn	Ni	Cr	Mo	Cu	N	S	P
	0.025	0.7 - 1.0	1.5 - 2.0	9.5 - 11.0	19.5 - 20.5	0.3	0.2	0.060	0.015	0.020

21-05-2013 – REV03

Category Stainless steel welding wires

Standards W Nr.: 1.4316
AWS - SFA 5.9: ER 308LSi
EN ISO 14343 – A: 19.9LSi

Approvals

	MIG	TIG	Subarc
TÜV (Germany)	X	X	X
DB	X	X	X
CE	X	X	X

Corrosion resistance

- Good general corrosion resistance. This grade is particularly recommended where there is a risk of intergranular corrosion.
- Very good atmospheric corrosion resistance in urban and rural medias.
- 308LM suits most food products and lot of chemical products such as cold alkaline solutions when diluted, cold organic acids when diluted, neutral and alkaline salt without holidays,....

Applications UGIWELD™ 308LM is a filler metal well suited for welding of austenitic stainless steels type 304 and 304L, and also stabilised austenitic stainless steel type 321.

- Equipment for chemical industry.
- Equipment for food processing industry.
- Pipes and tubes.
- Boiler engineering.

UGIWELD™ 308LM may be used for welding of some ferritic steels such as 409: automotive exhaust systems.

ii. Oerlikon Welding Wire

Here below the datasheet of the material used as feedstock to produce all specimens except the plate shaped ones.

INERTFIL 308LSi



Drahtelektroden für das Schutzgasschweißen korrosions- und hitzebeständige Stähle

Massivdrahtelektrode für das MAG-Schweißen artähnlicher austenitischer Cr-Ni-Stähle/-Stahlgussorten. Unter Beachtung der Anforderungen auch einsetzbar für ferritische nichtrostende Cr-Stähle. Unter nasskorrosiven Bedingungen für Betriebstemperaturen bis 350 °C, zunderbeständig bis 800 °C. Höherer Siliziumgehalt für besseres Anfließen und Nahtaussehen. Spritzerarmer Werkstoffübergang im Kurz-, Sprüh- und Impulslichtbogen.

Normbezeichnungen	Zulassungen	Grad
EN ISO 14343-A: G 19 9 L Si	DB	●
AWS A5.9 ER 308L Si	TÜV	●

Chemische Zusammensetzung (typische Werte in %)

C	Mn	Si	P	S	Cr	Ni	Ferrit
0.020	1.8	0.85	< 0.025	< 0.020	20	10	5-10

Mechanische Eigenschaften des reinen Schweißgutes

Wärmebehandlung	Streckgrenze (MPa)	Zugfestigkeit (MPa)	Dehnung A5 (%)	Kerbschlagarbeit ISO-V (J)	
				20 °C	-120 °C
Unbehandelt	≥ 350	≥ 520	≥ 35	≥ 80	≥ 32

Schutzgas 98% Ar+2% O₂

Schutzgase - EN ISO 14175 : M12, M13

Werkstoffe

AS1 304 - 304L - 302

1.4541 (X6CrNiTi18-10); 1.4301 (X4CrNi18-10); 1.4311 (X2CrNi18-10)

Lagerung/Rückbrocknung

Trocken lagern

Stromart/Polung/Schweißposition

DC+



